Doctoral Dissertation

Development of Highly Functional Biomedical Materials by Plasma-based Surface Modification

A thesis presented for the degree of

Doctor of Philosophy

ANJAR ANGGRAINI HARUMNINGTYAS

Division of Precision Engineering and Applied Physics

Graduate School of Engineering

OSAKA UNIVERSITY

Japan

October 2023

"I dedicate this research to my mother, who has had multiple bone implant surgeries, and to my husband, who is struggling with a spinal disease."

Acknowledgments

In the name of Allah, Most Gracious and Most Merciful. Alhamdulillah, all praise is always to Allah Subhanahu Wata'ala, the Almighty who created all universe, humans, and the day afterlife.

I would like to express my deepest gratitude to Prof. Satoshi Hamaguchi for his kindness giving me the opportunity to join his laboratory. I am grateful for his guidance throughout my master's and Ph.D. studies, and for allowing me to participate in collaborative research, experiments, and simulations related to plasma technology and its application. I also appreciate his support in enabling me to expand my knowledge by attending conferences, and plasma schools in Japan and abroad. These experiences have helped me gain knowledge, expand my research experience, and network with other experts. Thank you very much for your trust and support over all these years.

I would also like to express my gratitude to Assist. Prof. Tomoko Ito, who has patiently taught me a lot through experiment skills, valuable advice, discussions, and explanations of this research. I deeply appreciate your kindness and sincerity.

I extend my gratitude to my office, the National Research and Innovation Agency of Indonesia (BRIN) for providing the opportunity and permission to pursue my studies abroad in Japan. My acknowledgment to a Japanese government scholarship, the Ministry of Education, Culture, Sports, Science and Technology (MEXT), Japan for supporting my PhD program.

I would like to express my gratitude to Prof. Yoshitada Morikawa for providing me with the chance to enroll in the International Priority Graduate Program on Applied and Engineering Physics, Division of Precision Engineering and Applied Physics, Graduate School of Engineering, at Osaka University. I am grateful for his insightful comments and advice. I would also like to extend my gratitude to Prof. Yuji Kuwahara, Assoc. Prof. Ikutaro Hamada, and Assoc. Prof. Satoru Yoshimura for their willingness as reviewers for my doctoral thesis and for providing me with comments and advice to improve the quality of my research.

I would like to express my gratitude to Prof. Satoshi Sugimoto, who assisted me in becoming familiar with a plasma system for plasma polymerization from the start of my master's degree until the beginning of my doctoral studies. I also appreciate the insightful suggestions provided by Prof. Masato Kiuchi, Prof. Kazuhiro Karahasi and Dr. Ikuse during our laboratory meetings. I would like to extend my appreciation to Isobe-san and Dr. Nicolas for sharing knowledge about simulation. I also want to thank Dr. Pierre for sharing knowledge about his plasma system and its diagnostics.

I would like to acknowledge our collaborators in the orthopedic department at Osaka University, Prof. Takashi Kaito, Dr. Joe Kodama, and Masato Ikuta-sensei

for their fruitful discussions and valuable contributions to biological experiments, both (*in vitro* and *in vivo*).

I am really grateful to Yuko Umemura-san for her kindness and invaluable support not only in the laboratory and university but also for her care and assistance in various matters. I am also thankful to Yano-san and Nagao-san for their assistance in the laboratory. I would like to express my gratitude to Sakai-san and Kumagai-san for their assistance and for sharing valuable information from the university.

I am also thankful to Assoc. Prof. Lenka Zajickova for the opportunity to collaborate on research at the Central European Institute of Technology (CEITEC) in Brno, Czech Republic. I also thank Marek Elias for kindly teaching me to operate the thin-film deposition machines in the clean room at CEITEC. Thanks to Josep Polcak who teach me to operate high-resolution XPS at CEITEC. I am grateful to Katka, Jenifer, Pretty, David, Pretty, et. al for their support during my stay in the Czech Republic.

I would like to express my gratitude to Watsuji-san, Iwaki-san, and Konda-san, who helped and taught me in the nano clean room at the nanotechnology open facilities, ISIR, Osaka University. I also want to thank Omitsu-san, Katano-san, and Haneoka-san for teaching me how to operate various XPS. Additionally, I am grateful to Murakami-san for teaching me FE-SEM and EDS, and to Eguchi-san for teaching me ICP-AES.

I would also like to extend my gratitude to all members of the Hamaguchi

laboratory in the past and now, especially Erin, Charisse, Sarah, Nina, Enggar, Jomar, Kita-kun, Jarl, Kawabata-kun, Hojun, Abdul, Taira, Kotani, Ichikawa, Elif, Lucas, Fujita-kun, Mieda-kun, Yanagisawa-kun, Kometani-kun, and other members. I will miss the moments we shared various activities that we enjoyed together, such as talks and discussions in the laboratory, hiking, BBQs, hanami in spring, and badminton.

I am also deeply grateful to all my friends from Indonesia and Malaysia, and my neighbors in Dai Dai Dai (including Aoyamadai) who made me feel like I am among family when I am away from my home country. Thank you for making my journey so memorable.

Last but not least, I would like to express my sincere gratitude to my husband for enlightening discussions, for inspiring me and teaching me many valuable things throughout my life. I truly appreciate you for being consistently by my side and supporting me at all times. I am also grateful to my parents for their support and unwavering prayers. Thank you so much to my brother, sister, and entire family for their continuous support and prayers. I couldn't have achieved anything without all your love and support.

Abstract

This study discusses thin-film deposition using low-pressure plasma for orthopedic applications. Plasma polymerization and sputter deposition were chosen as methods to modify the surface of artificial bone. Plasma polymerization of amine groups was performed on surfaces of calcium phosphates e.g., hydroxyapatite (HA) and β-tricalcium phosphate (β-TCP) surfaces, which are widely used as artificial bone. The gas mixture of CH_4/N_2/He was used to deposit amine groups by plasma-enhanced chemical vapor deposition (PECVD) with bipolar pulsed plasmas. The plasma system used for our experiments generates high-voltage ($\pm 1.1\,\mathrm{kV}$) low-frequency ($5\,\mathrm{kHz}$) pulsed plasmas with a pulse duration of $1\,\mu\mathrm{s}$. Chemical properties of deposited polymer films were investigated with X-ray photoelectron spectroscopy (XPS). Derivatization with 4-trifluoromethyl benzaldehyde (TFBA) was used to estimate the concentration of primary amines in deposited polymers. For interconnected porous HA and β-TCP, it was found that plasma polymerization could take place not only on the outer surfaces of such materials but also on the surfaces of their inner pores.

The results of *in-vitro* experiments showed that plasma-treated calcium phos-

phate exhibited significantly enhanced hydrophilicity, facilitating the deep infiltration of cells into interconnected porous calcium phosphate. The cell adhesion and osteogenic differentiation on the plasma-treated artificial bone surfaces were also enhanced. The plasma polymerization afforded high bone regeneration capacity in *in-vivo* observation. These results suggest that amine modification of artificial bone by plasma technology can provide high osteogenic ability and represents a promising strategy for resolving current clinical limitations regarding the use of artificial bone.

With the PECVD experiments discussed above, it was found that only a small percentage (about 12 %) of the deposited nitrogen atoms formed primary amine groups (NH_2). To understand how to increase the percentage of primary amines in the deposited polymer, the interactions between the deposited film surface and incident precursors were performed using molecular dynamics (MD) simulation. To evaluate a possible upper limit of the primary amine concentrations in the deposited film, simulations of a rather unrealistic process were performed, where all nitrogen atoms from the plasma were supplied as amino radicals (NH_2) together with other hydrocarbon radicals and ions. If all incident amino radicals were to stay as NH_2 in the deposited polymer, the primary amine density would be extremely high. However, it has been found that, even under such "ideal" conditions for the maximum primary-amine content, hydrogen atoms of incident NH_2 radicals tend to be transferred to surrounding C atoms in the polymerization process, leaving a relatively small amount of primary amine (the concentration ratio of primary amino groups (NH_2) to nitrogen atoms N being approximately 10 %) in the deposited polymer films. The results indicate that an increase of NH_2 radicals

in the gas phase of PECVD hardly increases the primary-amine content in the deposited films and, therefore, the primary-amine content may not depend strongly on the plasma conditions as long as a sufficient amount of nitrogen and hydrogen is supplied during the plasma polymerization process. The primary amine content predicted by the simulations was found to be in good agreement with earlier experimental observations.

I also examined the possibility of improving the biocompatibility of different types of artificial bone made of Polyetheretherketone (PEEK). In this study, $SrTiO_3$ (STO) was deposited on PEEK surfaces using an RF magnetron sputtering plasma under varying conditions. It is known that Sr can significantly enhance the osseointegration of PEEK implants and surrounding native spinal bone. It was found that, with simple deposition of STO, Sr can be released to the surrounding tissues (or water contained in such tissues) quickly if the STO-coated artificial bone is implanted in a human or animal body. This study successfully demonstrated that multi-layer structures of Ti and STO can control the release rate of Sr into surrounding water when the coated film is immersed in water. Such multi-layer Ti and STO coating is an effective candidate to achieve sustained Sr release from PEEK implants over an extended period.

List of Abbreviations

ALP	Alkaline phosphatase
Ar	Argon
BE	Binding energy
BIC	Bone-implant contact
β-TCP	Beta-tricalcium phosphate(β-TCP)
C	Carbon
Ca	Calcium
CaP	Calcium phosphate
CH_4	Methane
DBD	dielectric barrier discharge
EOG	Ethylene oxide gas
FE-SEM	Field-emission scanning electron microscopy
FTIR	Fourier-transform infrared spectroscopy

G-L	Gaussian-Lorentzian
ICP-AES	Inductively coupled plasma-atomic emission spectroscopy
H	Hydrogen
HA	Hydroxyapatite
He	Helium
MD	Molecular dynamics
N	Nitrogen
N_2	Nitrogen (gas)
NH	Secondary amine
NH_2	Primary amine
O	Oxygen
OES	Optical Emission Spectroscopy
P	Phosphate
PECVD	Plasma enhanced chemical vapor deposition
PEEK	Polyetheretherketone
PP	Plasma polymerization
RF	Radio frequency
Si	Silicone

$SrTiO_3$	Strontium Titanate
STO	$SrTiO_3$
TFBA	4-trifluoromethyl benzaldehyde
Ti	Titanium
TMP	Turbo molecular pump
XPS	X-ray photoelectron spectroscopy

Contents

Chapter 1

Introduction

1.1 An overview of surface modification on artificial bone as biomaterial

The demand for bone replacements (such as hip and knee replacements) continues to increase globally with millions of surgeries performed annually to treat damaged or deteriorated bones [1]. Moreover, osteoporosis cases are also growing, leading to weakened bone structures and lead to bone degeneration. These conditions were affecting approximately 21.7 % of the population in Asia, Europe, and America [2]. Therefore, this prevalence significantly contributes to the growing demand for bone replacements such as artificial bone.

Artificial bone materials that are commonly used for bone regeneration or replacement i.e., titanium alloys [5], zirconia [6], steel [7], bioceramics (HA or hydroxyapatite ($Ca_{10}(PO_4)_6OH_2$), β-TCP ($Ca_3(PO_4)_2$)) [3, 8–11], biopolymer (e.g.

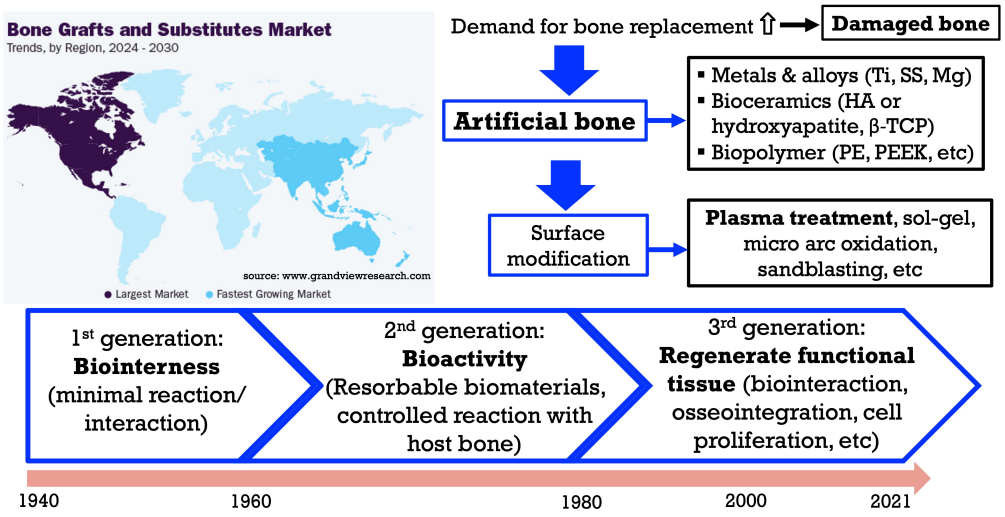

Figure 1.1: Schematic representation of the demand for artificial bone as bone replacement with the development of biomaterial surface modifications.[3, 4]

polyethylene (PE), polyetheretherketone (PEEK), polylactic acid (PLA), etc) and composite materials [12, 13]. However, current artificial bone products have limitations in promoting biocompatibility and osteogenic potential such, as bone growth. The study to improve the capabilities of artificial bone ability began around 1940 with the first generation, which focused on biointerness. This was followed by the second generation, which emphasized bioactivity. Currently, we are in the third generation, aiming to regenerate functional tissue through surface modification using various methods as explained in Fig. 1.1.

Plasma-surface modification was applied to biomaterials for biomedical fields to enhance the surface functionalities with various methods, such as plasma sputtering and etching, plasma implantation, plasma deposition, plasma polymerization by functional group attachment, laser plasma deposition, plasma spraying, magnetron sputtering [14–16]. The advantages of plasma-deposited films in bio-

materials are easy preparation, unique film chemistry, its ability to be coated on unique substrates with good adhesion, conformal and pin-hole free films, excellent permeation barriers with low levels of reachable, sterile upon preparation [15].

Plasma surface modification has become widely used to enhance the surface properties of artificial bone made from ceramics such as porous hydroxyapatite (HA).[9, 17] HA is commonly used in hard tissue replacement due to its composition, which is similar to human bones. A previous study has shown that untreated HA artificial bone exhibit low hydrophilicity and require extended healing periods when exposed to O_2 and He gases through dielectric barrier discharge (DBD) plasmas. However, HA treated with O_2/He plasma shows minimal effects in *in vivo*, likely due to the instability of the generated hydroxyl groups [9]. Therefore, further investigation is needed to improve the bone regeneration ability of artificial bones using low-pressure plasma.

1.2 Fundamental of low-pressure plasma

Although plasma is already well written in several textbooks [18, 19], it is necessary to introduce the basic knowledge of plasma before discussing its application. Historically, Sir William Crookes discovered DC discharge in a vacuum tube in the late 19th century. In 1929, this phenomenon was introduced as plasma by Irving Langmuir, it is known as the fourth state of matter. This state of matter is generated by the ionization of neutral atoms or molecules, positive ions, and free electrons with sufficient energy.[18, 19]

There are two types of non-thermal plasma or low-temperature plasma i.e., low-pressure plasma and atmospheric plasma. In low-pressure plasma, the electrons and other particles rarely collide, therefore the temperature remains low and close to room temperature. This condition occurs where $T_i \approx T_n \ll T_e$. Low-pressure plasma can be generated at working pressures below 1 mbar or 100 Pa. Meanwhile, atmospheric plasma is generated at pressures around 1 bar.[20]

In plasma processing, there are important parameters to obtain desirable plasma conditions. Low-pressure plasma depends on the flow rate of monomer gases and plasma pressure (controlled by a vacuum system) to regulate the number of molecules entering the chamber. The power source commonly used to generate plasma i.e., direct current (DC) or alternating current (AC), radio frequency (RF at 13.65 MHz), microwave, and so on.[19–21] The essential parameters of plasma are potential in plasma and at surfaces, electron temperature, plasma density, and ion flux. With plasma potential, the electron can adsorb and transfer the energy from the external circuit to the discharge gas, accelerating and causing collisions with molecules of gases, which leads to ionization and dissociation. These processes continue with increasing electron density, while the chemical reaction in the plasma are controlled by ions.[20] The general chemical reactions in the gas phase possibly occur in plasma materials processing such as electron-ion pair production (1.1), radical production (1.2), negative ion production (1.3), gas-phase chemical reaction (1.4), ion transport to surfaces (1.5), radical transport to surfaces (1.6), and surface-phase reactions (1.7).[19]

$$\mathrm{e} + \mathrm{AB} \longrightarrow \mathrm{AB}^{+} + 2\,\mathrm{e} \tag{1.1}$$

$$\mathrm{e} + \mathrm{AB} \longrightarrow \mathrm{e} + \mathrm{A} + \mathrm{B} \tag{1.2}$$

$$\mathrm{e} + \mathrm{AB} \longrightarrow \mathrm{A}^{-} + \mathrm{B} \tag{1.3}$$

$$\mathrm{A} + \mathrm{B} \longrightarrow \mathrm{C} + \mathrm{D} \tag{1.4}$$

$$\Gamma_i = -\mathrm{D}_a \nabla \mathrm{n}_i \tag{1.5}$$

$$\Gamma_{\mathrm{A}} = -\mathrm{D}_{\mathrm{A}} \nabla \mathrm{n}_{\mathrm{A}} \tag{1.6}$$

$$\mathrm{A(g)} + \mathrm{B(s)} \longrightarrow \mathrm{C(g)} \tag{1.7}$$

When the specific chemical reactions occur in the plasma and modify the surface of a substrate, hence, various surface phenomena may take place such as adsorption, desorption, ion implantation, surface diffusion, surface mixed layers, collision cascade, etc as shown in Fig. 1.2. The plasma may modify the surface continuously by fluxes of neutral (reactive atoms and radicals), ions, electrons, and photons.[22] The interaction between molecule and surface is causing adsorption such as physisorption (weakly bound due to low attractive van der Waals force) and chemisorption (covalent bonding between atoms or molecules with the surface).[19]

Low-pressure plasma has been attracted to modify various surfaces, including the biomaterials surfaces. The surface modification of biomaterials using low-pressure plasma will be discussed in the next section, specifically focusing on plasma polymerization and plasma sputtering.

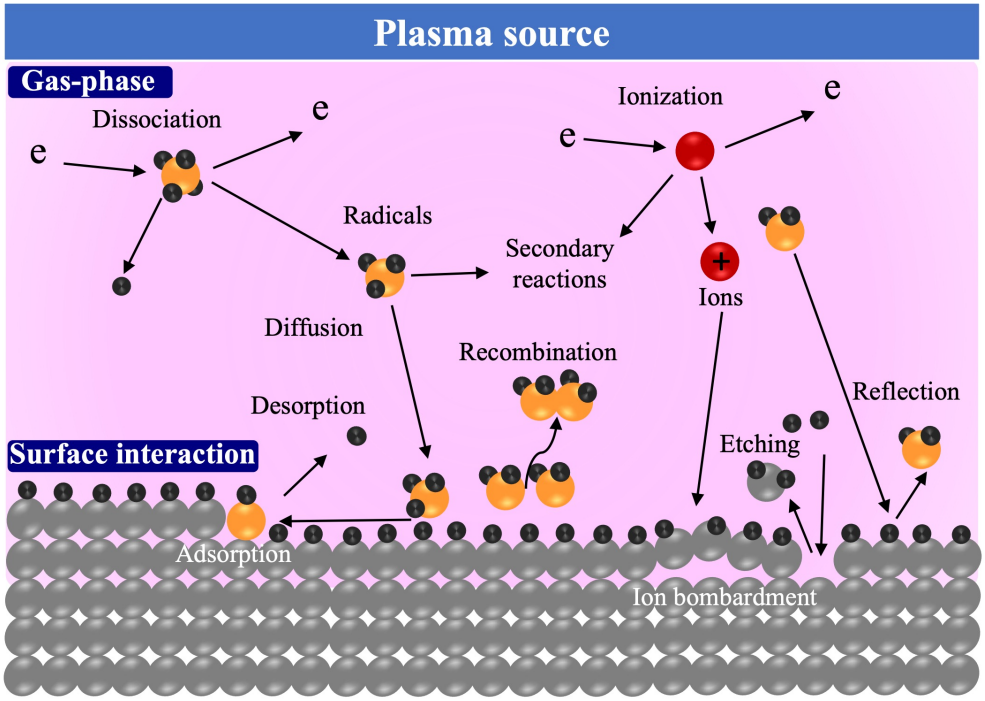

Figure 1.2: Schematic representation of the phenomena in plasma surface interaction at low pressure. [23]

1.3 Plasma polymerization on biomaterials, including artificial bone implants

Plasma polymerization or glow discharge polymerization has been studied since the 1960s and 1970s [24]. Plasma polymerization is defined as a process of thin film deposition that is performed through plasma to activate a monomer. In this process, an organic gas or vapor is introduced into electric discharge, where high-energy electrons efficiently break it down into radicals. Subsequently, these radicals adsorb onto the surface with high concentrations of trapped radicals and form a macromolecule of organic polymer [24]. The organic substances created

through this process are referred to as plasma polymers, which exhibit noteworthy irregular structures in both their chemical and physical properties when compared to conventional polymers [25].

The crucial of plasma polymer is ultrathin films with minimal flaws from vacuum deposition of covalently bonded materials [24]. The properties of plasma polymer are influenced by the used monomer and discharge parameters. The process is typically carried out using a gas mixture that includes a monomer and a noble or inert gas, such as argon (Ar) or helium (He). The inert gases are able to reduce the breakdown voltage and enhance the discharge through the metastables and Penning ionization mechanism [26]. The chemical composition of the top thin layer can be altered significantly through plasma polymerization, but the modification does not affect the bulk of the substrate.

The important aspects of plasma polymerization were discussed by Yasuda [27]. Hegemann also explained using the theory of macroscopic description how to optimize plasma polymerization [28, 29]. They suggested that the power input is considered by the parameter of $W/(F.M)$, where W is the electrical input power (Watt), F is volume flow rate, and M is the molecular weight of the gas [24, 27]. This equation parameter represents the energy in the plasma per unit of monomer flow and is equivalent to the energy density in the plasma. This following quasi-Arrhenius's behavior with activation energy E_a corresponds to plasma chemical reaction as given by

$$\frac{R_m}{F} = G \exp\left(-\frac{E_a}{W/F}\right) \tag{1.8}$$

where G is denoted as a reactor geometrical factor related to the conversion of monomer into film growth, R_m is the mass deposition rate.

The deposition rate in plasma polymerization, which is defined as the mass of film growth per area and time is dependent solely on the monomer supply. The deposition rate would be constant near room temperature and decreases with increasing temperature [28]. The deposition of plasma polymerization is primarily dominated by radicals.

Plasma polymerization offers the benefits of producing pinhole-free, conformal, and thin films that can be applied to a variety of substrates using a straightforward, one-step coating process [30]. Therefore, many researchers were interested in the application of plasma polymer on biomaterials using low-pressure gas-discharge plasmas [24, 31–33].

Plasma polymerization has been utilized to introduce various functional groups, such as amines, hydroxyl, and carboxyl, onto biomaterial surfaces. Among these, amine functionalization has demonstrated promise in improving bio interfaces on scaffolds for tissue engineering applications, particularly for fibroblast cells [34–36], polycaprolactone nanofiber [37–43], polyethylene [44], and HA on Ti substrate [45]. Amine functionalization of 3D porous scaffold with RF plasma and microwave-induced plasma has been reported to improve osseointegration and enhance osteoblast migration and cellularization, respectively [40, 46]. Plasma poly-

merization has been used to induce osteogenesis differentiation of adipose-derived stem cells in bone tissue engineering [47]. This suggests that plasma polymerization with amino functionalization is a promising technique for surface modification of ceramic calcium phosphate as an artificial bone for orthopedic applications [10].

1.4 Plasma sputter deposition on artificial bone

In plasma sputtering, films are grown through a deposition process whereby ionized atoms or molecules are accelerated from the target onto the substrate surface by high-energy ions in a vacuum chamber [48, 49] Typically, Ar^+ is chosen for bombardment due to its chemical inertness, low cost, and similar atomic mass to commonly used metal targets like Ti, Cr, Au, Al, and Cu.

Sputter deposition is a highly advantageous method for metal deposition when compared to other methods, as it produces high-energy flux with high surface mobility, resulting in smooth, dense, conformal, and continuous films. Sputtering is also able to preserve the stoichiometry of the target source, as the physical bombardment mechanism of particle ejection results in consistent stoichiometry on the sample surface [48, 49].

There are several sputtering systems used for sputter deposition of thin films e.g. DC diode plasma, RF plasma, magnetron sputtering plasma, and reactive sputter deposition [48, 49].

It reported that magnetron sputtering offers several distinct advantages owing to its specific characteristics when applied to the preparation of thin films on

biomaterials [50–52]. This technique includes a vacuum chamber, an RF generator, a matching network, a magnetron, and a cooling system. RF magnetron sputtering typically is operated at frequencies of 13.56 MHz. The integration of a matching network and a controller plays an important role in ensuring that the RF supply seamlessly aligns with the output impedance of the generator, harmonizing with the cathode and anode's impedance. Several key factors influence the quality and reliability of coatings, such as discharge power, gas flow rate, working pressure, substrate temperature, deposition duration, post-heat treatment, and the use of negative substrate bias [53].

Magnetron sputtering offers several unique advantages when it comes to biomaterials (e.g. hydroxyapatite and Ti alloys) [50–52]. This technique allows for uniform coating, dense and pore-free coatings, and the coating of substrates with minimal thermal impact. Additionally, magnetron sputtering enables the deposition of high-purity films, precise control over the coating structure (amorphous or crystalline), and the capability to tailor the Ca/P ratio. The resulting bonding strength of the coating can exceed 30 MPa, making it well-suited for various biomaterial applications, particularly in enhancing the biocompatibility and functionality of medical implants [53].

Various dopants including strontium (Sr), silicon (Si), and silver (Ag), have been found to exert significant effects on the in vitro biological performance of calcium phosphate coatings (CaPs) [54–56]. In particular, the addition of strontium (at levels ranging from 3% to 7% atomic concentration) in hydroxyapatite (HA) thin films has shown a pronounced positive impact on HA coatings con-

cerning osteointegration and bone regeneration. When MG63 osteoblast-like cells were exposed to these Sr-doped HA coatings, notable enhancements in several key indicators of bone health were observed. This included significantly increased values for alkaline phosphatase (ALP) activity, osteocalcin, type I collagen, and the osteoprotegerin related to activation of cytokine receptor ratio [53]. Moreover, the presence of strontium led to considerable reductions in osteoclast proliferation, effectively countering undesirable bone resorption processes. The review paper about the effect of titanium implants with and without Sr-containing also reported that Sr-modified titanium implants may shorten the healing period, enhance osseointegration, and significantly increase bone-implant contact rate (BIC) [57]. These findings highlight the potential of strontium coatings to promote better outcomes in terms of bone tissue interactions and regeneration.

1.5 Objective

The goal of this study is to develop surface modification on artificial bone under various low-pressure plasmas close to room temperature. Calcium phosphate and polyetheretherketone (PEEK) were used as artificial bone in this study. For this purpose, we perform both experimental and simulation to understand the mechanisms and surface reactions during plasma deposition.

This thesis is explained in four main sections. In Chapter 2, we describe the details of the chemical structure of amine PPs on hydroxyapatite (HA) prepared from CH_4/N_2/He in the bipolar pulsed discharge at 70 and 100 Pa. In Chapter

3, we examined the interaction between the amine-containing polymer surfaces with incident radicals and ions in a simplified plasma polymerization process for C-based polymers. In Chapter 4, we demonstrate the effects of amine modification on β-TCP for in vitro cell adhesion, osteogenic differentiation, and in vivo bone regeneration using a gas mixture of CH_4, N_2, and He by low-pressure plasma. In Chapter 5, we reported the surface modification on PEEK implant through $SrTiO_3$ deposition using RF magnetron sputtering plasmas. The findings of this study, which investigated the surface modification of artificial bone under various low-pressure plasma at room temperature, are presented in the general conclusion in Chapter 6.

Chapter 2

Amine Plasma Polymers Deposited on Porous Hydroxyapatite Artificial Bone with Bipolar Pulsed Discharges

2.1 Introduction

Calcium phosphates, such as hydroxyapatite (HA, $Ca_{10}(PO_4)_6(OH)_2$) and β-tricalcium phosphate (β-TCP, $Ca_3(PO_4)_2$), are widely used as materials for artificial bones because of their chemical similarity to the mineral components of human bones. [58–61] Ideal bone grafts require stable ceramic materials with high biocompatibility, appropriate mechanical properties, high osteoconductivity, and an interconnected porous structure. [3, 58–63] Because calcium phosphates gener-

ally lack high biocompatibility, there have been several attempts to modify their surfaces to improve their biocompatibility and osteoconductivity. For example, The treatment of artificial bone made of interconnected porous HA with O_2/He plasma of dielectric barrier discharges increased its hydrophilicity and shortened the bone growth period in *in vivo* experiments. [8, 9, 64] The sputter deposition of a strontium-containing metal[65] can also stimulate bone growth around artificial bones, as demonstrated for zirconium and titanium alloy implants.[66]

Polymer deposition by plasma-enhanced chemical vapour deposition (PECVD), i.e., plasma polymerization, has also been used to coat material surfaces with bioactive thin films containing desired functional groups such as amino and carboxyl groups. [28, 47, 67–70] Earlier studies have also shown some positive effects of amine PPs on biocompatibility and bone regeneration such as improved cell adhesion, spreading, proliferation, and osteogenic differentiation. [44, 47, 71] Kodama *et al.* [10] demonstrated in their *in vivo* study that amine PPs deposited on interconnected porous β-TCP artificial bone enhanced bone regeneration.

This study aims to discuss details of the chemical and physical properties of the amine PPs used in Ref. 10. Standard crystalline silicon (Si) and porous HA were used as substrate materials for plasma polymerization, rather than the β-TCP used in Ref. 10. As expected and discussed later, the same amine PPs are formed on these substrates, regardless of the substrate material, as long as the same plasma polymerization method is used. In the *in vivo* study of Ref. 10, the amine PP-coated artificial bone samples were sterilized by autoclaving (120 °C for 20 min). Autoclaving can change the chemical nature of the deposited amine PPs,

which is also discussed in this study. Numerical simulations are used to examine possible mechanisms of the incorporation of nitriles (– C≡N) into the deposited films observed in the experiments.

The remainder of this article is organized as follows: Section 2.2 discusses the materials and methods used in this study. In Sec. 2.3, some general properties of the depositing plasmas as well as the deposited amine PPs are presented, including the film stability for up to two months and the effects of sterilization. In Sec. 2.4, numerical simulations of amine plasma polymerization processes are presented. Finally, the conclusions are presented in Sec. 2.5.

2.2 Materials and methods

2.2.1 Substrate materials

The calcium-phosphate substrates used in this study were interconnected porous HA NEOBONE^{TM} samples supplied by Aimedic MMT, Tokyo. The sample was a 2 mm thick disk with a diameter of 5 mm, a porosity of 72–78%, and an average pore diameter of 150 µm. The pores were nearly spherical and interconnected through nearly circular holes with an average diameter of 40 µm. The calcium (Ca), phosphor (P), and oxygen (O) atomic concentration ratios of the samples were measured with X-ray photoelectron spectroscopy (XPS), as described below, and found to be Ca:P:O = 31:16:53, which were close to the ideal stoichiometry of HA of Ca:P:O = 23.8:14.3:61.9.

Silicon (Si) substrates were also used for film characterization. They were double-sided polished (111) single crystals, N-type phosphorus-doped, with a resistance of 0.5 Ω cm. Before use, samples were cleaned with 99 % ethanol in an ultrasonic bath for 1 min.

2.2.2 Plasma discharge conditions and optical emission spectroscopy (OES)

The plasma polymerization system used to deposit amine PPs in this study is the same as the low-pressure bipolar pulsed discharge system described in Ref. 10, as shown in Fig. 2.1. The design of the plasma chamber and voltage source was based on previous plasma studies. [72–74]

The cylindrical vacuum chamber was made of stainless steel with a diameter of 400 mm and a height of 784 mm. The top circular aluminum electrode, 80 mm in diameter, was grounded, and the bottom circular molybdenum electrode, 190 mm in diameter, was connected to a high-voltage bipolar pulse generator. The distance between the two electrodes was 38 mm. The substrates were placed on the bottom electrode. The positive or negative voltage pulse applied to the bottom electrode had a width of 1 µs and the voltage was 1.1 kV or −1.1 kV (peak-to-peak voltage 2.2 kV). The positive and negative pulses were applied alternately, with a time lapse of 100 µs between the start of two consecutive positive and negative pulses. The power, repetition frequency, and duty cycle were typically 15 W, 5 kHz, and 1 %, respectively.

Prior to discharge, the chamber was evacuated with a turbomolecular pump at a pressure below 5×10^{-3} Pa. The substrates were sputter-cleaned in an Ar discharge for 10 min at a pressure of 70 Pa sustained by a rotary pump. For the PP deposition, the discharge was ignited with a CH_4, N_2, and He gas mixture at 70 or 100 Pa. The flow rates of CH_4, N_2, and He were typically set at 10, 20, and 10 sccm, respectively, and the deposition time was typically 30 min unless stated otherwise.

Optical emission spectroscopy (OES) of the plasma was performed with an OP-FLAME-T/Ocean Optics spectrometer in the optical wavelength range of 300–700 nm. The resolution was approximately 1 nm for an internal slit width of 5 µm. The optical emission spectrometer was placed right outside the quartz window and directly collected part of the optical emission from the plasma passing through the quartz window. The distance between the quartz window and the center line of the electrodes was approximately 200 mm.

2.2.3 XPS and chemical derivatization of primary amine

XPS analysis was carried out with a Shimadzu ESCA-850 with a non monochromatized Mg-Kα 1253.6 eV X-ray source at Osaka University, Japan, unless otherwise indicated. The pass energy was 75 eV and the point diameter was 8 mm (90 % uniformity).

The concentration of primary amines ($-NH_2$) on a sample surface was determined with chemical derivatization, using 4-trifluoromethyl-benzaldehyde (TFBA). [70, 75, 76] The carbonyl group (C=O) of a TFBA molecule forms an imine bond

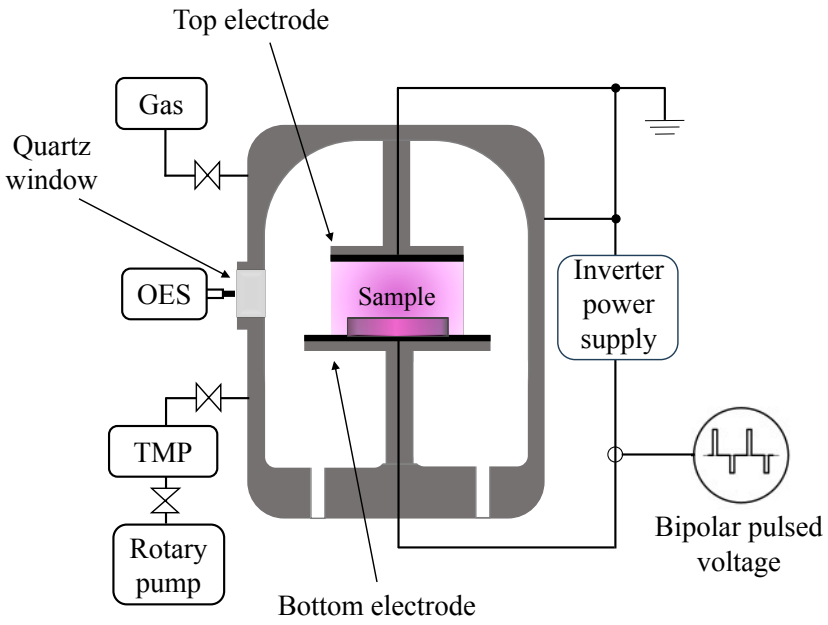

Figure 2.1: Schematic diagram of the bipolar pulsed discharge system used in this study. It is a parallel plate discharge system and high-voltage bipolar pulses are applied to the bottom electrode, on which substrates are placed. The top electrode and chamber walls are grounded. The applied peak-to- peak voltage was 2.2 kV (±1.1 kV) with a repetition frequency of 5 kHz (i.e., the time lapse between the positive and negative pulses being 100 µs), a pulse duration of 1 µs, and therefore a duty cycle of 1 %. The chamber was evacuated with a turbomolecular pump (TMP) and a rotary pump. In this study, plasmas were generated with a CH_4, N_2, and He gas mixture at a total pressure of 70 Pa or 100 Pa. The optical emission spectra were measured through a side glass window.

with an NH_2 group on a polymer surface. The derivatization process started with a glove box being evacuated with a vacuum pump. It was then filled with Ar gas at 60 sccm for about one hour. Subsequently, 1 ml of TFBA was added to 50 ml of glass beads in a glass vial. This process was carried out separately for both untreated samples and PP-coated samples inside the glove box. The reaction between TFBA vapour and the samples occurred in an Ar atmosphere at room temperature (25 °C) for four hours inside the glove box. Assuming all primary amino groups on the sample surface were bonded with TFBA molecules and non-

bonded TFBA did not remain on the sample surface, we determined the surface concentration of $-CF_3$ groups of TFBA, using ESCA-850 XPS, to estimate the concentration of primary amino groups on the sample surface as [77–79]

$$[NH_2] = \frac{[F][C]}{3[C] - 8[F]} \tag{2.1}$$

where [C] and [F] denote the concentrations (i.e., number densities) of C and fluorine (F) atoms determined by XPS.

2.2.4 Film thickness measurements

The thickness of a deposited PP film was measured on a Si substrate. Before the film deposition, a rectangular stainless-steel plate (10 mm × 3 mm) with a thickness of 1 mm was placed on each substrate as a mask. After the film deposition on the masked sample, the mask was removed, and the step profile of the deposited film was measured across both coated and uncoated areas of the substrate using a stylus profilometer (Dektak-XT Bruker). Typically, five measurements at different locations were conducted on each sample.

2.2.5 Sterilization of PP-coated materials

Sterilization of artificial bone is an essential step before bone graft surgery. For a better understanding of how a sterilization process affects the functionality of deposited PPs, surface analyses of deposited PPs were performed also after sterilization. This study used standard sterilization methods for ethylene oxide gas (EOG) and autoclave. For autoclave sterilization, the samples were placed in

an autoclave and heated at a high temperature (120 °C) for 20 min. whereas for EOG, the samples were exposed to ethylene oxide gas for 24 hours.

2.2.6 MD simulation of film growth

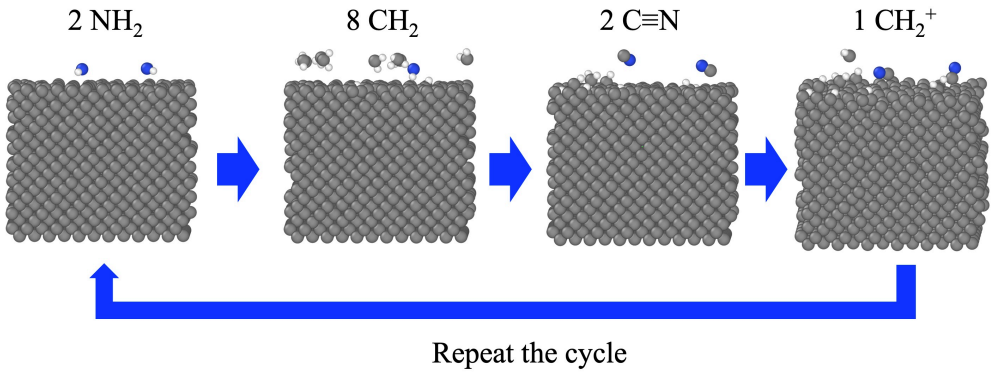

Figure 2.2: Schematic description of radical and ion irradiation steps in MD simulations of this study. Each image represents a single irradiation step with the number of incident radical or ion species indicated above the image, showing a side view of a C film model with grey, blue, and white spheres representing C, N, and hydrogen (H) atoms, respectively.

The film deposition processes were examined with MD simulations under simplified conditions, as in the study of Ref. 80. More specifically, in this study, the incident radical and ion fluxes were assumed to be NH_2, CH_2, CN, and CH_2^+ with flux ratios of NH_2:CH_2:CN:CH_2^+ = 2:8:2:1 at a surface temperature of 300 K.

We by no means intend to imply that these are typical incident radical and ion flux ratios in our experiments. Because we cannot measure the incident radical and ion fluxes of our experimental system, it is difficult to estimate how close or far off these flux ratios are to or from the actual radical and ion fluxes. We used the flux ratios above for the following reasons: Earlier studies indicate that CH_2 and CH_3 are dominant radical species containing C atoms in typical hydrocarbon plas-

mas [81–84] and NH and NH_2 are dominant radical species containing N atoms in typical nitrogen/hydrogen plasma [85]. Here we select NH_2 and CH_2 as representative species, as in the earlier MD simulation study of Ref. 80, because CH_2 has a higher sticking probability than CH_3 (due to their numbers of dangling bonds) and the maximum possible formation of primary amines ($-NH_2$) was sought for in the earlier study. As to ion species, because C-containing radicals are likely to be more dominant than N-containing radicals, we select $CH_2{}^+$, which has the same chemical composition as the CH_2 radical species we selected for this study, so as not to introduce additional complications. The flux ratios of radicals and ions were selected such that, in the absence of CN radicals, the atomic concentration ratio of N to C atoms of the deposited film in the simulation became similar to the experimentally obtained value. Because the radical-to-ion flux ratio is typically high, we selected the ratio NH_2:CH_2:$CH_2{}^+$ = 2:8:1. With these ratios, as shown in Fig. 6 of Ref. 80, the N-to-C ratio of deposited film in simulation is about 15 %, which is close to the experimentally observed value of 18 %, as will be discussed in Subsec. 2.3.2.

As we shall discuss in Sec. 2.4, the goal of the MD simulation study is to clarify the formation mechanisms of nitriles ($-C{\equiv}N$) in the amine PPs when CN radicals exist in the depositing plasma. Therefore, we use a (possibly unrealistically) large CN radical flux to augment the formation of nitriles for easier observation. In this way, we selected the flux ratios of NH_2:CH_2:CN: $CH_2{}^+$ = 2:8:2:1 essentially for consistency and simplicity.

A C film model with a surface area of 2.14×2.14 nm^2 was used as a substrate

material. A diamond structure of C atoms was used for simplicity, but a sufficiently dense amorphous C film model would result in essentially the same results for polymer deposition. The C atoms in the two atomic layers at the bottom were fixed in position to prevent the downward drift of the film model during simulation due to the momentum transfer from incident species. Periodic boundary conditions were applied in the horizontal directions such that the top surface represented an infinitely wide surface region.

The deposition process was approximated by cyclic deposition of incident species in the following manner: Each deposition cycle consisted of 4 irradiation steps, as shown in Fig. 2.2. In the first irradiation step, two NH_2 radicals were injected into the top surface of the material at randomly selected surface locations with predetermined incident kinetic energies. In the second, third, and fourth irradiation steps, 8 CH_2 radicals, 2 CN radicals, and a single CH_2^+ ion were injected, respectively, in a similar manner.

For simplicity, the angle of incidence for each incident species was set to be normal to the initial C substrate surface (even if the deposited polymer surface became rough). The incident species were released slightly above the top material surface in each irradiation step. The kinetic energy of each charge-neutral radical species was assumed to be 0.2 eV. The energy of 0.2 eV, which is higher than the thermal energy at room temperature but lower than typical bond energies, was selected because it reduces the simulation time by speeding up the motion of slow species without much affecting the properties of deposited films. The ion energy was varied from 0.2 to 100 eV.

In each irradiation step, the MD simulation was performed under the constant-total-energy (i.e., microcanonical or NVE ensemble) condition for an initial duration of 700 fs. It was then followed by a cooling process for 1,300 fs, with a 1,200 fs Langevin thermostat [86] and a 100 fs Berendsen thermostat. [87] The cooling process was designed to reduce the material temperature gradually to 300 K before the next irradiation step started. Thus the total duration of each irradiation step was 2.0 ps. The interatomic-potential and force field models for C, N, and H systems used in this study were essentially the same as those used in the earlier studies of Refs. 80, 88–91. For further information on the MD simulation method, the reader is referred to Ref. 80.

2.3 Results and discussions

2.3.1 Optimization of plasma polymerization conditions

The film growth was optimized with Si substrates under various deposition times, N_2 gas flow rates, and gas pressures. Figure 2.3 shows the deposition rate and N content in the deposited films as functions of the N_2 flow rate at a total gas pressure of 100 Pa. It is seen that the deposition rate decreases as the N_2 flow rate increases. This is because the relative amount of C in the gas phase, which is the main polymer-forming species, decreases as more N_2 gas is introduced to the discharge chamber with a fixed total pressure. The N content in the deposited film increases with the N_2 flow rate. Although not shown here, the films contained a small amount of O (4–6 % of the total atomic concentrations of C, N, and O),

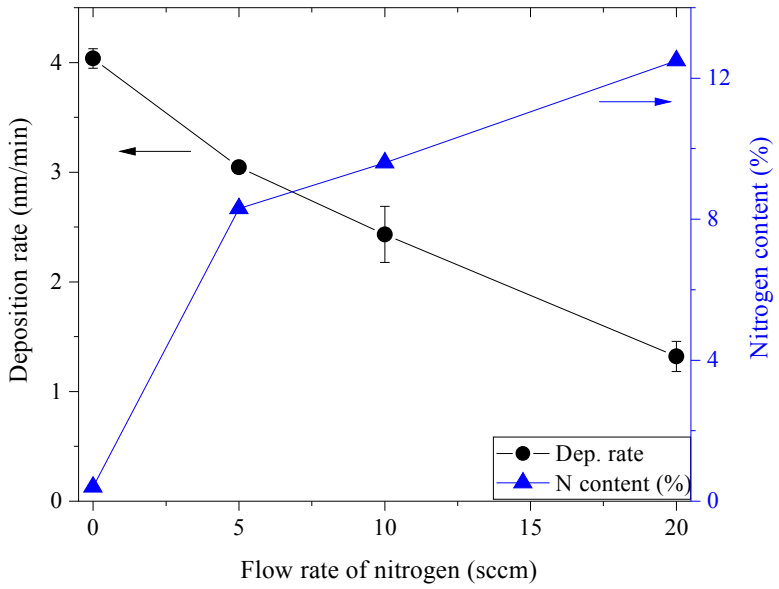

Figure 2.3: Deposition rate and N content of amine PP films deposited on Si as functions of the N_2 gas flow rate at 100 Pa. The gas flow rates of CH_4 and He were both 10 sccm. The deposition time was 30 min. The N content is defined by [N]/([C]+[N]+[O]) evaluated from XPS. The other process conditions were the same as those presented in Subsec. 2.2.2.

which did not correlate with the N_2 flow rate.

Taking into account other practical factors such as discharge stability, we performed the polymerization in this study mostly with CH_4, N_2, and He flow rates of 10, 20, and 10 sccm, respectively, and a deposition time of 30 min at a total pressure of 70 Pa (rather than 100 Pa of Fig. 2.3.) The other process conditions were the same as those presented in Subsec. 2.2.2. Under these conditions, the deposition rate and N content were 0.9 ± 0.1 nm/min, which made the thickness of the deposited film around 30 nm for 30 min deposition. In the rest of the paper, these polymerization conditions are used unless indicated otherwise.

2.3.2 Amine PP deposition on porous HA

With the polymerization conditions discussed above, PP films were deposited on both Si and porous HA substrates. Figure 2.4 shows the relative atomic compositions of Ca, P, C, O, and N on untreated porous HA surfaces and deposited PP films on HA and Si substrates. The number n in the figure indicates the number of substrate samples used for the measurements and the error bars represent their standard deviations. A single measurement was made near the centre of each sample disk surface (facing the plasma in the case of plasma-treated samples).

As expected, the same PPs were deposited on both Si and porous HA samples. No Ca or P was observed from the PPs on HA samples, indicating that the films were thick enough and completely covered the HA substrates. It also indicates that the observed O signals of amine PP-coated HA samples came from the deposited PP films, not HA, and therefore are of O impurities. As seen in Fig. 2.4, the N-to-C concentration ratio of amine PPs was about 18 %.

For porous HA substrates, amine PPs were also deposited on the inner pore surfaces. Such amine PPs facilitate bone formation inside the pores of artificial bones. [10] The cross-section of a PP-coated porous HA disk was analyzed with high-resolution XPS with an Axis Supra (Kratos Analytical) spectrometer at the Central European Institute of Technology (CEITEC), Brno, Czech Republic, in the following manner: An amine PP-coated HA disk was cut along the central axis in half to form two semicircular disks along the central axis of one of the semicircular disks. During the deposition process, one flat surface of the HA

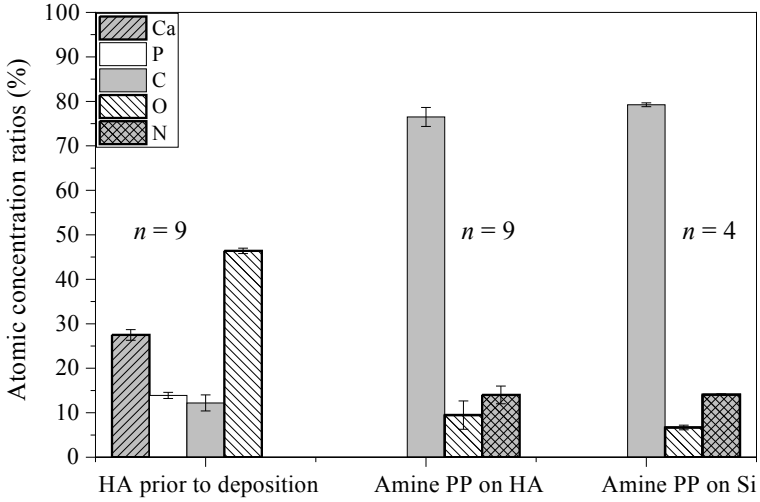

Figure 2.4: Atomic compositions of the porous HA substrate surfaces prior to film deposition and amine PP films deposited on the HA and Si substrate surfaces obtained by XPS (and, therefore, the H concentrations are not shown here). No N was observed on the HA substrate prior to the film deposition. No Ca, P, or Si was observed after the film deposition. The films were deposited at 70 Pa for 30 min. The flow rates of CH_4, N_2, and He were 10, 20, and 10 sccm, respectively. The number n represents the number of measured samples. The measurements of amine PPs were made one day after the film deposition.

disk faced the plasma while the other was in contact with the powered electrode surface. For reference, a XPS measurement was also made on a single spot of the plasma-facing surface of each semicircular disk.

The relative atomic concentrations along the central axis of an amine PP-coated porous HA disk are presented in Fig. 2.5. On the left-most side (in the shaded area), the atomic concentrations on the disk's top surface are presented. The horizontal axis represents the position along the central axis of the HA disk measured from the plasma-facing surface. It is seen that the chemical compositions gradually change towards nearly constant "bulk" values in the depth larger than approximately 400 µm. The variations of such bulk values (especially those of C

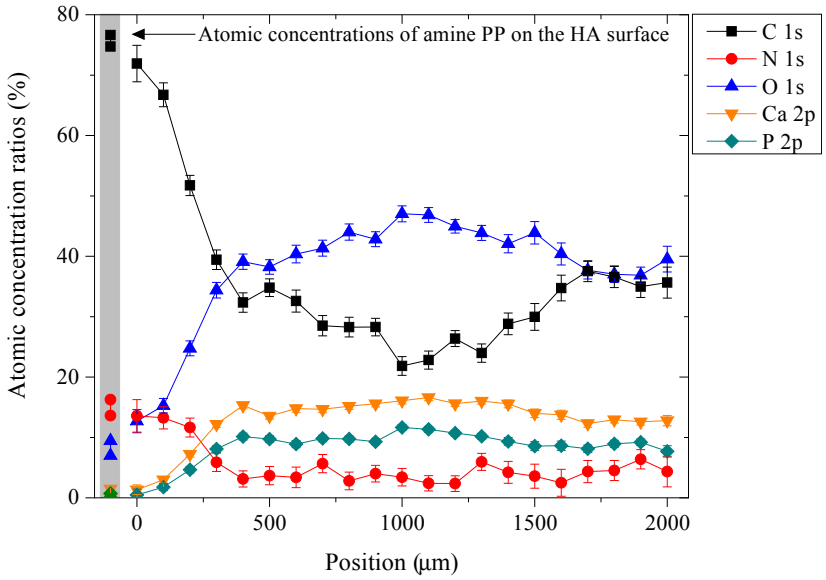

Figure 2.5: Atomic compositions from the cross-sectional analysis of the amine PP-coated porous HA disk (2 mm thick) obtained with high-resolution XPS. The X-ray spot diameter was 110 µm. The amine PP-coated HA disk was cut in half through its centre, and XPS measurements were taken along the centre axis. The first cross-sectional measurement point close to the coated HA top surface is marked 0 µm. The atomic concentrations measured on two different locations of the plasma-exposed HA top surface of the same HA disk (before the cross-section analysis) are plotted for reference in the shaded area below 0 µm. The error bars indicate the standard deviation obtained from Monte Carlo simulations for peak fit in CasaXPS software for a single-point narrow-scan XPS measurement for each data point. [92] The deposition pressure was 70 Pa and other deposition conditions are found in Subsec. 2.2.2.

and N) are most likely due to the randomness of the pore sizes and their positions. It should be noted that when the porous HA disk was cut in half, both HA materials and some inner pore surfaces were exposed on the cross-section. The relatively high concentrations of Ca and P in the bulk region of Fig. 2.5 originate from the newly exposed HA surfaces on the disk cross section. Nevertheless, non-negligible N signals are seen in a considerable material depth, indicating amine PP deposition on inner pore surfaces. The C concentration was also much higher than that of the untreated HA surface shown in Fig. 2.4. Deep penetration of the deposition

precursors was also observed for a porous β-TCP substrate coated with the same PP film [10].

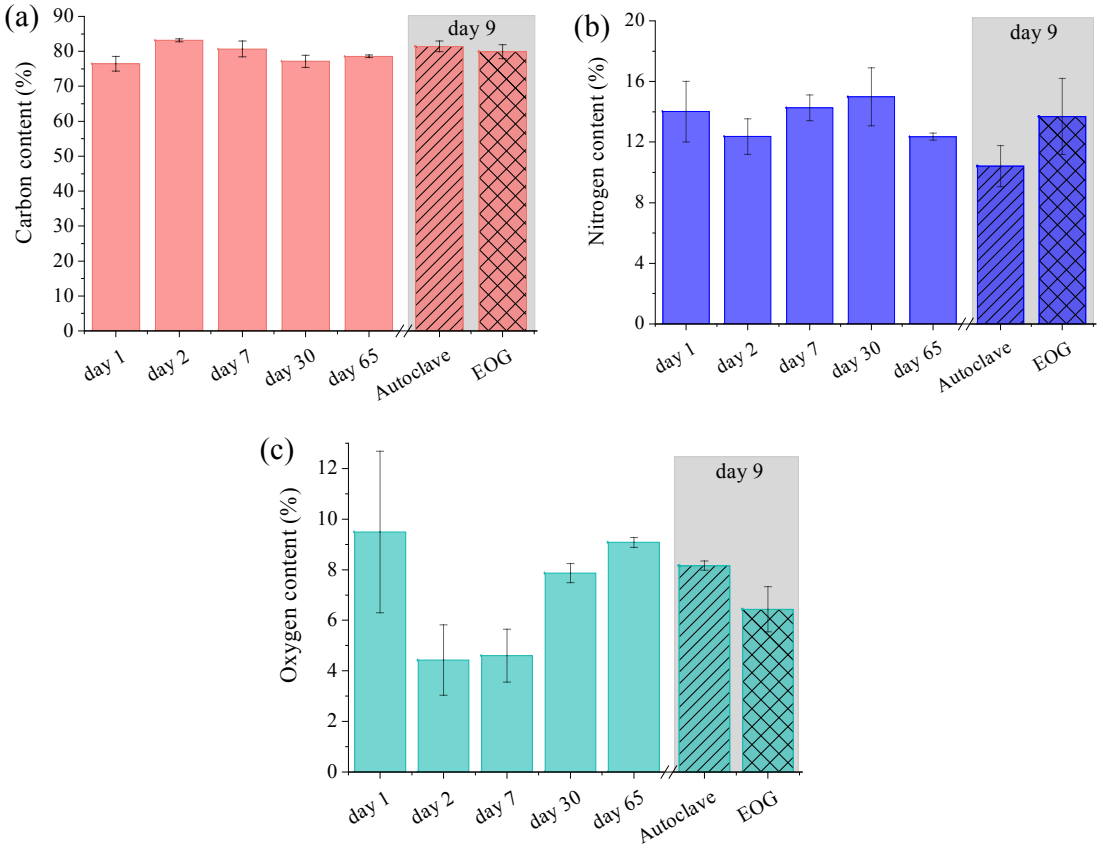

Figure 2.6: Relative concentrations of (a) C, (b) O, and (c) N atoms on amine PP film surfaces were measured 1, 2, 7, 30, and 65 days after the deposition with XPS. The samples denoted as "autoclave" and "EOG" were sterilized in an autoclave (120 °C for 20 min) and EOG (with a 24-hour exposure) one day after the film deposition, but their chemical composition measurements by XPS were performed 9 days after the film deposition. The films were deposited on interconnected porous HA disk samples with CH_4, N_2 and He, flow rates of 10, 20, and 10 sccm, respectively, a gas pressure of 70 Pa, and a deposition time of 30 min. The error bars were calculated based on data obtained from 9 different amine PP-coated samples for the measurement denoted as "day 1" and 3 different samples for the other measurements.

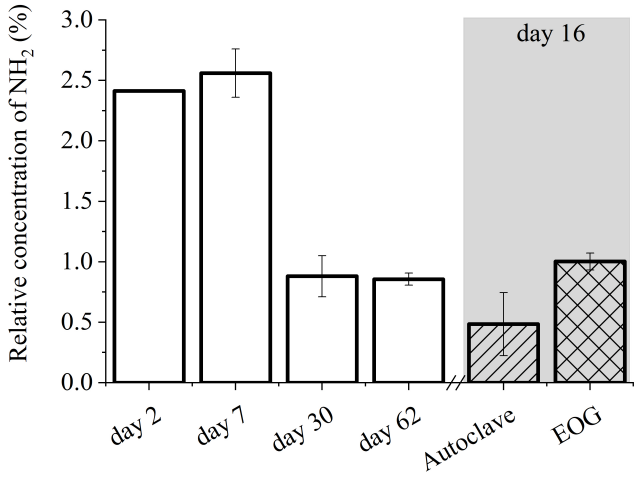

Figure 2.7: Relative concentrations of primary amine groups $-NH_2$, defined as $[NH_2]/([C]+[N]+[O])$, of the amine PP films deposited on porous HA samples, as a function of time after the film deposition. The chemical derivatization to determine the primary amine concentration was completed two days (day 2), 7 days (day 7), etc., after the film deposition, as indicated along the horizontal axis. The samples denoted as "autoclave" and "EOG" were sterilized in an autoclave (120 °C for 20 min) and EOG (with a 24-hour exposure) one day after the deposition and their derivatization was completed 16 days after the deposition. The error bars were calculated based on data obtained from 2 different samples for the measurement denoted as "day 7" and 3 different samples for the other measurements, except for "day 2" where data from a single sample is plotted.

2.3.3 Film stability

Figure 2.6 shows the changes in chemical compositions of amine PP films over about two months after the film deposition. After the film deposition, the samples were placed in sealed plastic bags to avoid dust and kept in a desiccator (with desiccants) without vacuum. The XPS measurements were performed one day (day 1), two days (day 2), etc., after the film deposition, as indicated along the horizontal axes of the figure. Some samples were sterilized in the autoclave or with EOG one day after the deposition, and their chemical compositions were measured by XPS 9 days after the film deposition, as indicated by "Autoclave" and "EOG"

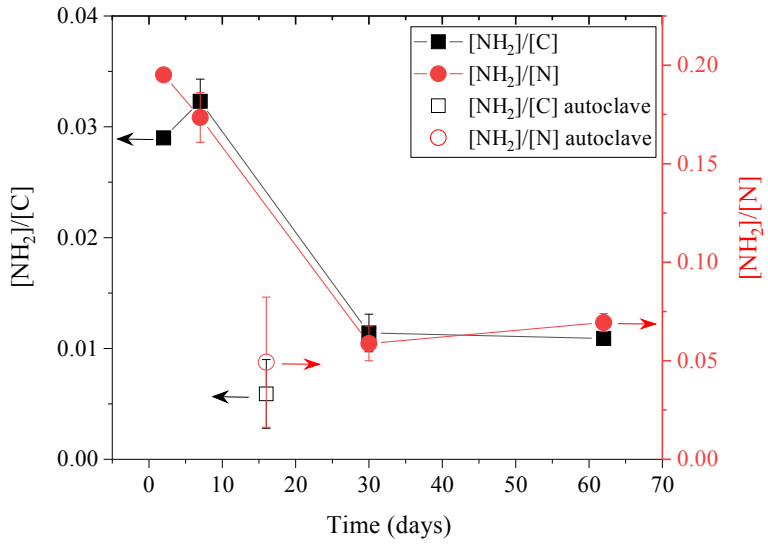

Figure 2.8: Ratio of the primary amine NH_2 concentrations to C and N atom concentrations on the amine PP films deposited on porous HA samples, obtained from the derivatization method as functions of time after the film deposition. The empty square and circle denote the values for the samples sterilized by autoclaving one day after the film deposition. The deposition conditions and the definition of error bars are the same as those of Fig. 2.7.

in Fig. 2.6. The chemical compositions hardly changed over two months after the film deposition. (The O content is relatively small and, therefore, subject to larger variations, compared to relatively small variations in the C content.) It is seen that the sterilization also hardly affected the chemical compositions of amine PP films.

Figure 2.7 shows the relative concentrations of primary amines ($-NH_2$) normalized by the sum of the C, O, and N atomic concentrations, i.e., $[NH_2]/([N]+[C]+[O])$, evaluated with the chemical derivatization described in Subsec. 2.2.3. The derivatization was completed two days (day 2), 7 days (day 7), etc. after the film deposition, as indicated along the horizontal axis. It is seen that the relative concentration of $-NH_2$ did not change much for the first week but went down

significantly over one month and reached a steady value. Other earlier studies also indicated that PPs containing amine groups are susceptible to oxidation in air, resulting in the formation of amides and other functional groups. [35, 93–95]

Some samples were sterilized in the autoclave or with EOG one day after the film deposition and their relative concentrations of primary amines were evaluated 16 days after the film deposition, as indicated by "Autoclave" and "EOG" in Fig.2.7. The figure suggests that the sterilization processes reduced the primary amine concentrations significantly because the loss of the primary amine by air exposure over 16 days seems much less than that caused by the sterilization. The relative concentrations of primary amines normalized by the C and N concentrations, i.e., $[NH_2]/[C]$ and $[NH_2]/[N]$ are also plotted as a function of time after the film deposition in Fig. 2.8. It is seen that approximately 20 % of N atoms of the deposited film formed primary amines immediately after the plasma polymerization process. However, this value dropped to approximately 5 % over one month if the sample was exposed to ambient air. Similarly, after the autoclave sterilization, approximately 5 % of the total N atoms form primary amines.

The earlier *in vivo* study by Kodama *et al.*, [10] reported enhanced bone growth on amine PP-coated porous β-TCP artificial bone after autoclave sterilization. Figure 2.7 suggests that the primary amine concentration of their artificial bone surfaces was also reduced by sterilization. However, it has not been clear how much primary amine is needed for bone growth enhancement as the secondary amine may also contribute to bone growth. Therefore, the primary amine concentration in itself may not be a major concern for bone regeneration applications.

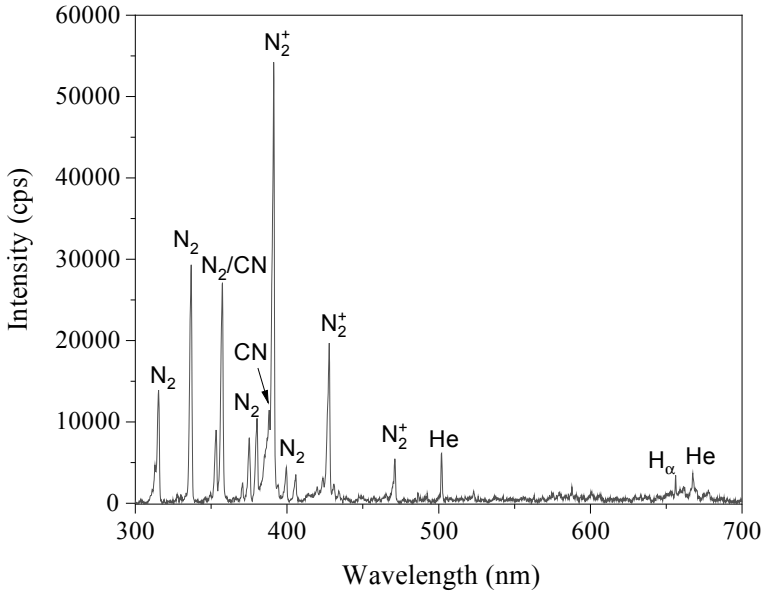

Figure 2.9: Optical emission spectra of a bipolar pulsed discharge of a CH_4, N_2, and He gas mixture with flow rates of 10, 20, and 10 sccm, respectively, at 70 Pa recorded during plasma polymerization. Other discharge conditions are found in Subsec. 2.2.2.

2.4 MD simulation on the possible formation of nitriles

Figure 2.9 shows the optical emission spectra observed during the plasma polymerization process. The observed strong peaks are those for $N_2{}^+$, N_2, CN, He and H_α. The OES peaks of N_2 were observed in the wavelength range from 300 to 400 nm. [96] The spectra of $N_2{}^+$ exhibit two strong peaks at 391.4 and 427.8 nm. [97, 98] The CN peaks were observed at 388.3 nm, sufficiently close to the peak of N_2 at around 359 nm. [96–98] Because the resolution of our OES measurement is not sufficiently high and detailed peak separation is not possible, some signals may originate from CN radicals.

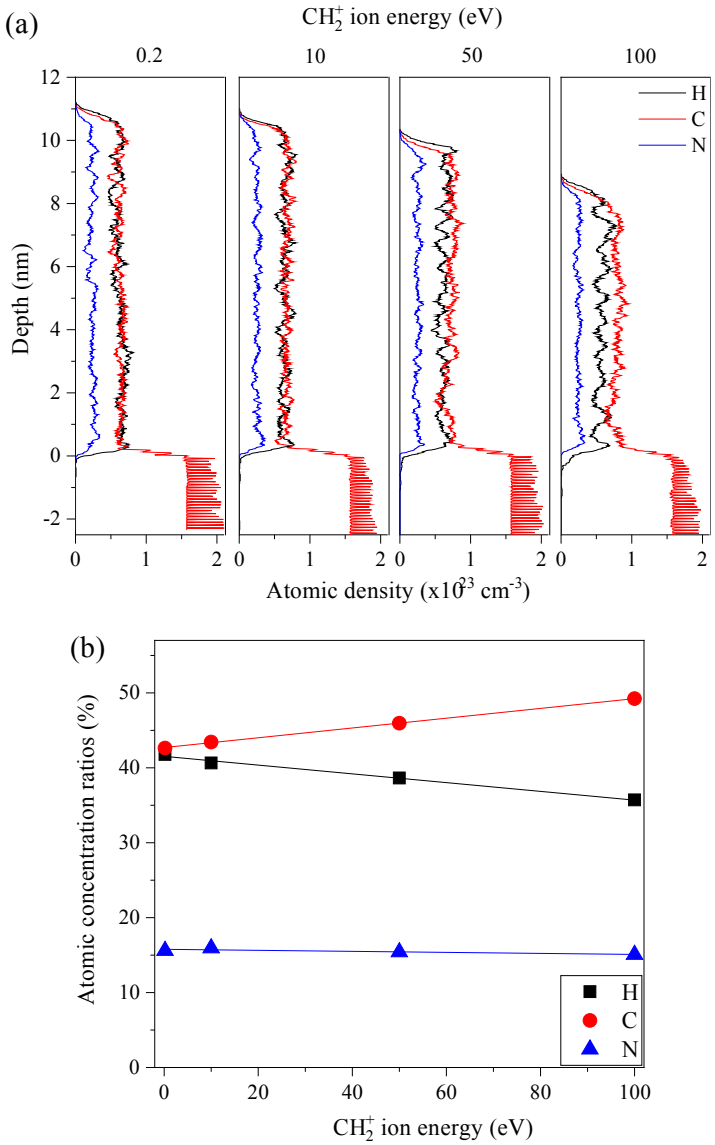

Figure 2.10: Atomic compositions of the deposited films obtained from the MD simulations with different kinetic energies (0.2, 10, 50, and 100 eV) of the incident CH_2^+ ions. (a) Depth profiles of atomic concentrations of H (black), C (red), and N (blue). The corresponding ion energy is given above each set of the profiles. (b) The relative atomic concentrations of H, C, and N atoms averaged over the deposited films as functions of the CH_2^+ ion energy.

Although we did not systematically monitor the OES data in this study, some CN radicals are likely to be present in the plasma, as discussed above. If there are some gas-phase CN radicals, they may be incorporated directly into the deposited PPs. When CN radicals interact with a polymer surface with abundant dangling bonds and H atoms, however, they are likely to lose some of their unsaturated bonds by forming new bonds with surface atoms. In general, it is difficult to evaluate the nitrile concentration in deposited polymers quantitatively. Fourier transform infrared (FT-IR) spectroscopy can detect the presence of nitriles in polymer films but typically cannot determine their concentration. In this study, we use MD simulations to examine how likely the incident gas-phase CN radicals can be converted to a nitrile (or retain its triple bond) when it is incorporated into the deposited film.

Following the earlier study of Ref. 80, we performed MD simulations of polymer deposition by amino and hydrocarbon radicals and ions together with CN radicals. More specifically, NH_2, CH_2, and CN radicals and $CH_2{}^+$ ions were deposited, as schematically described in Fig. 2.2. The properties of the virtually deposited polymer films obtained from MD simulations under the same simulation conditions without CN radicals are found in Ref. 80. As discussed in Subsec. 2.2.6, the intention is not to reproduce the experimental deposition conditions with this simulation study. Indeed the deposited films produced by MD simulations of this study have higher N concentrations than those of the experimentally obtained films because additional CN radicals are supplied to the surface in the simulations. Instead, the purpose of the simulation is to examine how many incident CN radicals keep their triple bonds under such simple deposition conditions.

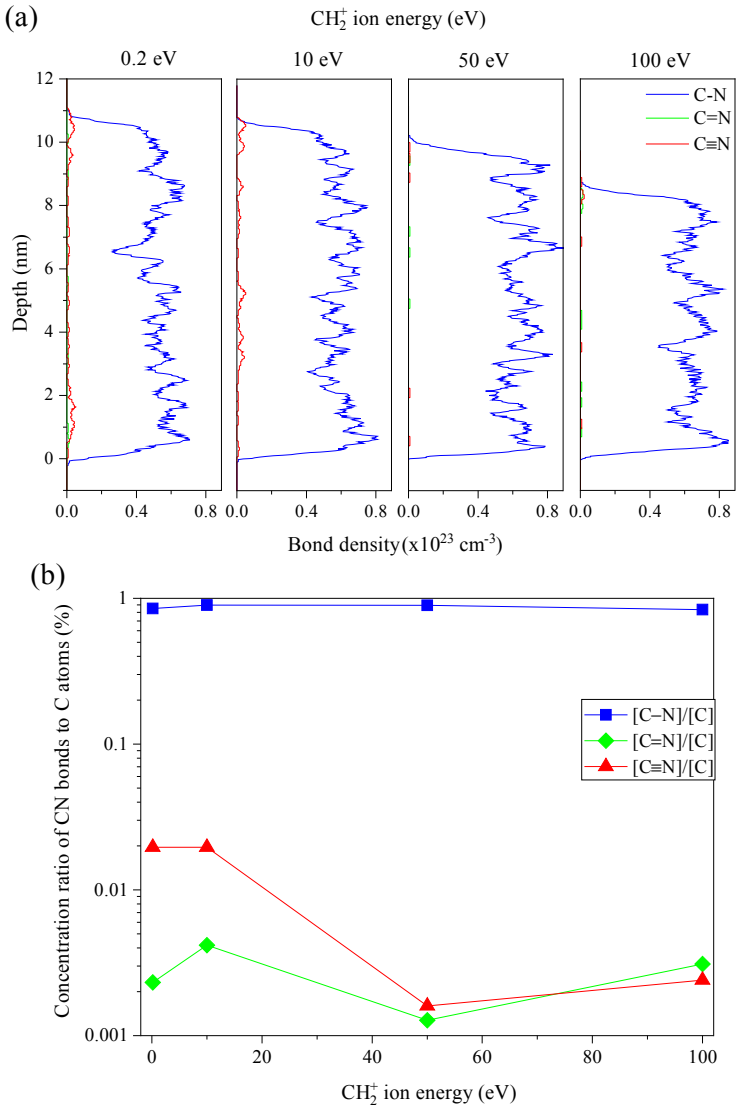

Figure 2.11: Concentrations of single, double, and triple bonds connecting C and N atoms in the deposited films obtained from the MD simulations with different kinetic energies (0.2, 10, 50, and 100 eV) of the incident CH_2^+ ions. The concentrations of other bonds are not shown here. (a) Depth profiles of C–N (blue), C=N (green), and C≡N (red) bond concentrations. The corresponding ion energy is given above each set of the profiles. (b) Relative concentrations of C–N, C=N, and C≡N bonds normalized by the C atomic concentration averaged over the deposited films as functions of the CH_2^+ ion energy.

Figure 2.10(a) shows the depth profiles of H, C, and N atomic concentrations in the deposited films, obtained from MD simulations. The vertical axis represents the depth (or height if the value is positive) of the film measured from the initial position of the substrate's top surface. The corresponding deposited film morphologies obtained from MD simulations are depicted in Fig. S1 of the Supplementary Information. Magnified images of one of the simulated amine PPs are also given in Fig. S2.

As the ion incident energy increases, the thickness of the film decreases. The concentrations of all atomic species averaged over the deposited films are given in Figure 2.10(b), which reveals that the amount of H decreases with increasing ion energy, as in the simulation results of Ref. 80. The cocentration ratio of N to C atoms in the deposited films is about 0.37 when the incident ion energy is close to 0, which reflects the fact that the incident flux ratio of N to C atoms is 4:11 (as shown in Fig. 2.2). The N-to-C ratio decreases with the increasing ion energy.

Figure 2.11(a) shows the depth profiles of the concentrations of C−N, C=N, and C≡N bonds in the deposited films. The concentration profiles of other bonds are not shown here for simplicity (but are given in Fig. S3 of the Supplementary Information). In Figure 2.11(b), the relative concentrations of C−N, C=N, and C≡N bonds normalized by the C atomic concentration averaged over the deposited films are presented as functions of the CH_2^+ ion incident energy. If all incident CN radicals retained their triple bonds in the deposited film, the ratio [C≡N]/[C] would be about 0.18, based on the flux ratios. However, the simulation shows that, even when the ion incident energy is low, this ratio is about 0.02, indicating that

only approximately 10 % of the incident CN radicals form nitriles in the deposited film.

In our polymerization experiments, the plasma-off time was much longer than the plasma-on time (with a duty cycle of 1 %). Therefore, CN radicals were likely to be formed in the recombining plasma. Furthermore, because of this low duty cycle, the effects of ion impact were overall minimal even if the applied voltage was high. This corresponds to the case of extremely low ion energy in our MD simulations.

As the ion energy increases, the surface atoms are mixed with other atoms in an increasingly wide and deep subsurface region by the ion impacts. This mixing of atoms increases the probability of incident CN radicals' reacting with other atoms and, therefore, breaking their triple bonds. The direct impact of energetic ions with nitriles on the surface can also break and eliminate their triple bonds.

2.5 Conclusions

Plasma polymerization with amine groups was performed on the surfaces of Si and porous HA, a model material for artificial bone. A gas mixture of CH_4, N_2, and He with flow rates of 10, 20, and 10 sccm, respectively, was used to deposit amine-containing polymers by PECVD with bipolar pulsed discharges. Under the typical experimental conditions used in this study, the plasma system generated high-voltage (± 1.1 kV) low- frequency (5 kHz) bipolar pulsed discharges with a pulse duration of 1 µs and a duty cycle of 1 % at a total pressure of 70 Pa. It was

found that N-containing polymers, referred to as amine PPs, were formed on the sample surfaces. The chemical derivatization method revealed that approximately 20 % of deposited N atoms formed the primary amine $-NH_2$ when they were deposited.

When the sample was exposed to ambient air in a sealed desiccator without vacuum for an extended period, the chemical compositions of the amine PPs hardly changed for up to two months. However, the atomic concentration ratio of primary amine groups to N atoms, i.e., $[NH_2]/[N]$, was reduced to approximately 5 % one month after the film deposition. Sterilization of amine PP-coated samples in an autoclave or by EOG was also found to reduce the $[NH_2]/[N]$ ratio to approximately 5 %. On the other hand, the earlier *in vivo* study by Kodama *et al.* [10] showed that porous β-TCP artificial bone coated with amine PPs by the same PECVD enhanced bone regeneration after sterilization by autoclaving. Although the presence of amines enhances bone regeneration, it is not clear whether the presence of the primary amine is especially effective in facilitating bone regeneration; the presence of the secondary amine may also contribute to bone growth.

Because deposition precursors with low sticking probabilities can penetrate the inner pores of the porous HA samples, amine PPs were also formed on the surfaces of the inner pores although the amount of deposited polymer was much less than that on the outer surfaces. These results are consistent with the earlier observations for porous β-TCP artificial bone samples with the same plasma polymerization. [10] The amine PPs deposited on the inner pore surfaces facilitate bone growth inside the pores of the porous artificial bone, as demonstrated in Ref. 10.

OES of the high-voltage bipolar pulsed discharges used for the plasma polymerization of this study suggested the possible presence of gas-phase CN radicals. Because the pulsed discharges had a low duty cycle (1 %) in this study, the recombining plasma was likely to allow the formation of CN radicals in the gas phase while ion impact had a minimal effect on the depositing film surface. The MD simulations of idealized deposition processes showed that, among all incident CN radicals from the gas phase, approximately 10 % of such CN radicals formed nitriles or retained their triple bonds C≡N in the deposited film if the ion impact effect is negligibly small. However, it was also found that energetic ion impacts significantly reduced the nitrile content in the deposited film.

Chapter 3

Molecular dynamics simulation of amine formation in PECVD with hydrocarbon and amino radicals

3.1 Introduction

Low-temperature plasmas have been widely used for material surface process applications [22, 99–107]. Among various processes using such plasmas, plasma-enhanced chemical vapor deposition (PECVD) is widely used for the deposition of carbon (C) based polymers. [24, 108, 109], which is also called plasma polymerization. PECVD processes often have an advantage over ordinary chemical vapor deposition (CVD) processes without plasmas because PECVD can be performed at a relatively low surface temperature. This is because, in PECVD, surface reactions are typically initiated by highly reactive free radical species gen-

erated in the plasma, rather than thermal reactions. Various plasmas generated by different techniques such as direct current (DC) [110], radio frequency (RF) [35–37, 70, 111, 112], microwave [32], and high-voltage pulse[10, 72, 74, 113, 114] plasmas have been used for plasma polymerization.

A recent study [10] used PECVD processes successfully deposited amine-containing polymers on the surfaces of artificial bones made of interconnected porous beta-tricalcium phosphate (β-TCP). The porosity of the artificial bone material was 72 $\sim$ 78% with an average pore diameter of 150 μm and an average diameter of interconnected passages of 40 μm. Amines (i.e., amino groups) are functional groups having a form of $-NH_2$ (primary amine) or $-(NH)-$ (secondary amine) with N being bonded with non-hydrogen atoms, typically C atoms in C-based polymers. Amines are known to have strong biological effects. For example, the presence of amines on a material surface increases its hydrophilicity and biocompatibility and promotes cell adhesion, immobilization of certain types of proteins, and accumulation of fibroblasts on its surface. [3, 24, 37, 44, 61, 70, 115–119]. The study of Ref. [10] has found that the presence of amines on artificial bone surfaces promotes bone regeneration.

It was also found in Ref. [10]that amine-containing polymers were formed even on the inner surfaces of interconnected pores of the artificial bone. Therefore plasma-treated interconnected porous β-TCP artificial bones enhanced the bone cell growth not only on their outer surfaces but also within their pores. The use of PECVD for polymerization allows precursor radicals to be transported deep into interconnected pores. Earlier studies of plasma-treated artificial bones with

oxygen (O) containing plasmas [120–122] also showed that the plasma treatment enhanced the bone cell growth but the surface stability and their effectiveness for bone growth *in vivo* were rather limited.

In Ref. [10], plasma-polymerization was performed with bipolar high-voltage pulsed discharges [72, 74, 113] with a maximum applied voltage of ±1.1 kV. The pulse duration was 1 μs at 5 kHz, with a duty cycle of 1 % and a gas pressure of 70 Pa. The discharge gases were CH_4, N_2, and He with flow rates of 10, 20, and 10 sccm, respectively. Because the applied high-voltage pulses were generated by an inverter power supply, the plasma generated in the plasma system was called inverter plasma. Although the applied voltage is high, the duty cycle was small and, therefore, the surface temperature of the deposited film was considered to remain close to room temperature. The plasma simulation results (based on an Ar discharge model) of Ref. [74] shows that the average ion kinetic energy is as low as 1 eV during a large part of the discharge except for the short pulse period, where the average ion kinetic energy can rise to about 100 eV.

The nature of CH_4/N_2/He-based plasmas of Ref. [10] may be different quantitatively from such Ar discharges generated under the same pulsed voltage conditions. However, we expect that ion energy distributions and their time dependence of CH_4/N_2/He-based plasmas used in the experiments of Ref. [10] are qualitatively similar to those in the simulations and the ions that dominantly affect the deposited film properties are those with kinetic energies up to 100 eV or so.

The amount of primary amine formed in the deposited polymer in the experiments of Ref. [10] was found to be relatively small; the ratio of the primary amine

concentration (i.e., number density), which we denote [NH_2], to the atomic nitrogen concentration [N], i.e., [NH_2]/[N], was about 8%. Other earlier polymerization studies with co-deposition of amino groups also show that the amine content in C-based polymers takes similar values.[76, 123–127] Then the question arises as to whether we can increase the amount of amine, especially primary amine, by adjusting plasma conditions, without compromising the film stability.

The goal of this study is to answer this question, at least partially, by examining the interaction between the amine-containing polymer surfaces with incident radicals and ions under simplified plasma polymerization process conditions. More specifically we ask the following question; if all incident nitrogen-containing species arrive at the surface in the form of amino radicals NH_2 in a polymer deposition process, will they remain mostly as NH_2 in the film, i.e., as primary amine, in the deposited film? If the answer is yes, the way to increase the primary amine content in the plasma polymerization process would be to find the discharge conditions that would maximize the concentrations of NH_2 radicals in the gas phase. If the answer is no, we must clarify the reason for it.

To perform this study, we use molecular dynamics (MD) simulations. [128, 129] MD simulations, where the equations of motion for individual atoms are integrated, have been used to study plasma-surface interactions at the atomic scale, [130] including deposition processes of various materials[91, 131–135] and plasma-polymer interactions. [88–90, 136, 137]. In this study, we irradiate C substrates with NH_2, hydrocarbon, and hydrogen (H) radicals as well as ions, and examine how amine-containing polymers are deposited. As in Ref. [10], the PECVD system that we

consider in this study is a bipolar high-voltage pulsed discharge (i.e., inverter plasma) system, as mentioned above, and therefore the deposition is assumed to take place at room temperature.

The rest of this article is organized in the following manner: In Sec. 3.2, we discuss the MD simulation method used in this study. The simulation results are presented and discussed in Sec. 3.3. The conclusions are given in the final section.

3.2 MD simulation

PECVD processes to deposit amine-containing polymers are modeled with MD simulation. In MD simulation, the motions of all atomic species are determined by the solutions of Newton's equations.[128, 129] The interatomic potential models for the system consisting of C, N, and H atoms (i.e., C/N/H system) used in this study are the same as those used in previous studies of Refs. [88–90, 135–138], which are based on Stillinger-Weber potentials[139–142] that represent multi-body interactions for covalent bonds among various atomic species. The bond energies used in our simulation are summarised in the Supplementary Material.

As in earlier MD studies for film deposition and etching of material surfaces, we use a small substrate irradiated by ions and charge-neutral species emitted from a plasma. Fig. 3.1 shows the C substrate model used in the study. Periodic boundary conditions are applied in the horizontal directions such that the top surface represents an infinitely large substrate surface. We used a diamond structure of C atoms for this substrate for simplicity, but a sufficiently dense amorphous carbon

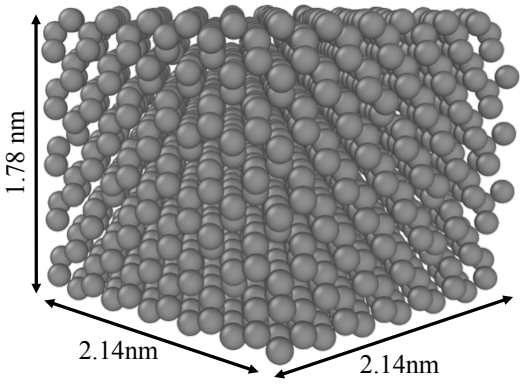

Figure 3.1: 3D rendering of the C substrate model used in our MD simulation. Each gray sphere represents a carbon atom. In each simulation, the substrate is initially in thermal equilibrium at 300 K.

Table 3.1: 5 different simulation conditions. Case I is the base case, which we examine in detail in this study. Cases II $\sim$ V represent different ways of providing additional H atoms to the system. The second row "Radical species" indicates the number of radical species supplied to the surface in a single ion injection cycle, as shown in Fig. 3.3. The third row indicates the total number of H atoms supplied to the surface in a single ion injection cycle. The kinetic energy of each ion was varied from 0.2 eV to 100 eV. The kinetic energy of each radical species was set at 0.2 eV. The substrate temperature was set at 300 K.

	Simulation conditions (Cases)				
	I	II	III	IV	V
Ion species	CH_2^+	CH_3^+	CH_3^+	CH_2^+	CH_3^+
Radical species	2 NH_2:8 CH_2	2 NH_2:8 CH_2	2 NH_2:8 CH_3	2 NH_2:8 CH_2:10 H	2 NH_2:8 CH_3:10 H
H atoms	22	23	31	32	41

substrate model would result in essentially the same results for film deposition. The C atoms in a thin bottom layer (more specifically, the 2 atomic layers at the bottom of the crystalline structures shown in Fig. 3.1) are fixed in position to prevent the downward drift of the substrate while it is subject to the momentum transfer from incident species.

As in earlier MD studies for film deposition and etching of material surfaces, we

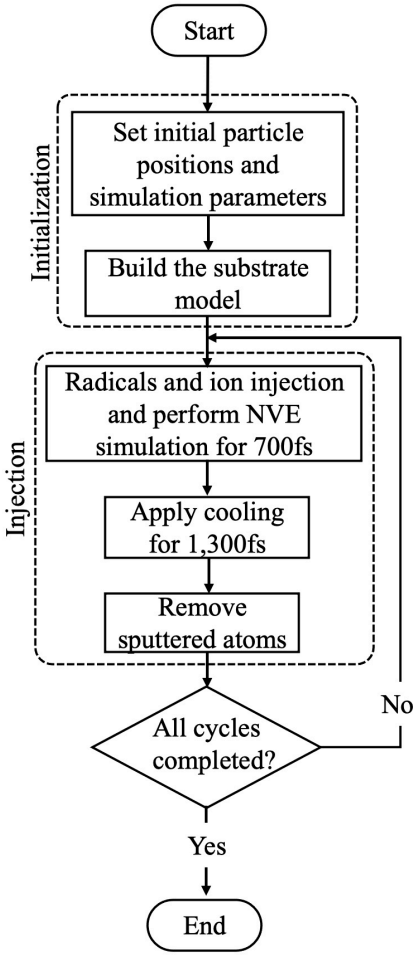

Figure 3.2: Flowchart of MD simulation of this study.

use a small substrate irradiated by ions and charge-neutral species emitted from a plasma. Fig. 3.1 shows the C substrate model used in the study. Periodic boundary conditions are applied in the horizontal directions such that the top surface represents an infinitely large substrate surface. We used a diamond structure of C atoms for this substrate for simplicity, but a sufficiently dense amorphous carbon substrate model would result in essentially the same results for film deposition. The C atoms in a thin bottom layer (more specifically, the 2 atomic layers at

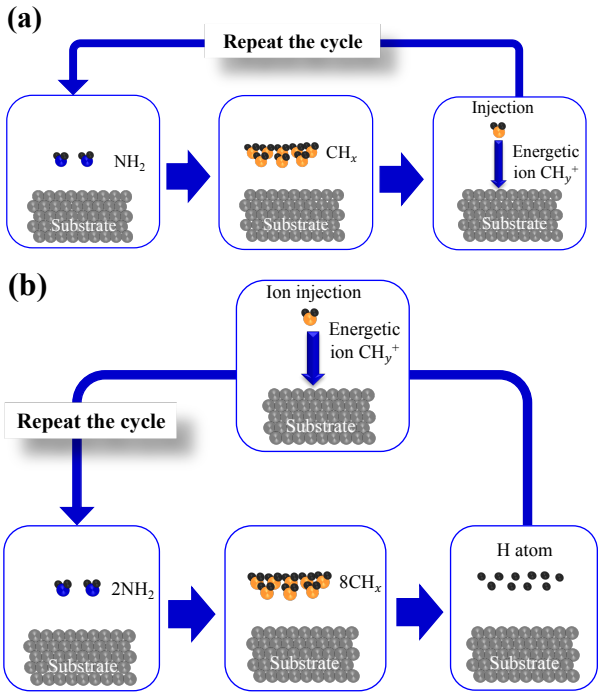

Figure 3.3: The way radicals and ions are injected in each ion injection cycle of MD simulation in this study. (a) First two NH_2 radicals are injected simultaneously, and then 8 CH_x radicals are injected simultaneously, and (b) in some cases, 10 H radicals are injected simultaneously, all at random horizontal positions. Then a single ion CH_y^+ is injected at a random horizontal position. The angle of incidence for all species is normal to the substrate surface. The injections of different species are performed sequentially within a relatively short period. (x, y = 2 or 3).

the bottom of the crystalline structures shown in Fig. 3.1) are fixed in position to prevent the downward drift of the substrate while it is subject to the momentum transfer from incident species.

The substrate was set in thermal equilibrium at 300 K prior to deposition simulation. This is because, as we discussed earlier, the PECVD system that we consider here is a bipolar high-voltage pulsed discharge (i.e., inverter plasma) system. In this system, the duty cycle is sufficiently small and the temperature of the deposited film is considered to remain near room temperature.

Under typical PECVD process conditions, a surface of a small area of 2.14×2.14 nm^2 shown in Fig. 3.1) hardly receive two ions or radicals nearly simultaneously because the ion or radical flux is sufficiently small. Therefore, as in earlier MD studies of plasma-surface interactions, we model the deposition process with a series of ion or radical injection cycles, in each of which an ion or a charge-neutral species may be injected into the surface. In this study, in each injection cycle, during the first 700 fs, the MD simulation was performed under the constant total-energy (i.e., microcanonical or NVE) conditions, followed by the cooling process for 1,300 fs, bringing down the material temperature to 300K. At the end of each injection cycle, we assume all floating atoms (which are considered to be sputtered or reflected) above the material surface, assuming they will eventually return to the gas-phase plasma. In this way, the total injection cycle time was 2 picoseconds. The cooling process consists of 1.2 picoseconds Langevin thermostat [86] and 0.1 picoseconds Berendsen thermostat [87]. The horizontal position of each ion impact is selected randomly and each ion is emitted from slightly above the top material surface.

Although two or more radicals are unlikely to arrive in the small area of the model substrate of Fig. 3.1), when we irradiate the surface with charge-neutral species, we typically inject multiple radicals or atoms simultaneously at random positions sufficiently far apart in a single injection cycle to make the simulation more efficient. This is because low-energy species separated sufficiently from one another hardly interact among themselves and their kinetic energies are too low to heat the surface significantly. When we irradiate the surface with ions, we typically inject a single ion in a single injection cycle. The general MD simulation flowchart

is illustrated in Fig. 3.2

The model substrate was set thick enough for our deposition process, but if any of the incident or recoiled species passes through the bottom layer in an injection cycle of incident species, the simulation automatically abandons the injection cycle, adds several new layers of the substrate from the bottom, and restarts the injection cycle. In this way, we ensure that the substrate is always sufficiently thick to keep all incident species on it or in its inside.

As discussed earlier, the goal of this study is to search PECVD conditions that maximize the primary amine content in the deposited polymer films when plasmas are generated with a gas mixture of CH_4, N_2, and He. Assuming He contributes only to generating plasmas and hardly affects surface reactions, we only consider gas-phase species generated from CH_4 and N_2 as deposition precursors. (He metastable species can provide sufficient energy to surface reactions, but we ignore such effects in this study for simplicity.)

Earlier studies [81–84] indicate that CH_2 and CH_3 are dominant radical species in typical hydrocarbon plasmas and they have different sticking probabilities on the depositing film surface.

In this study, therefore, as one of the simplest possible cases, we only consider CH_2, CH_3, NH_2, and possibly H radicals as incident radicals. As to ion impact, one of the most important effects of energetic ion incidence is the momentum transfer to the deposited film. Therefore, in this study, we only consider relatively heavy hydrocarbon ions such as CH_2^+ or CH_3^+. As to the supply of N atoms to the

deposited species, we only supply them in the form of NH_2 radicals, such that the process may produce films with the largest content of primary amines if the incident NH_2 radicals remain on the surface as they are just by bonding with surface C atoms without losing their H atoms. The experimental observation of Ref. [10] showed that the concentration ratio of N atoms to the sum of C and N atoms, i.e., [N]/[C+N], of the deposited films was about 12%. In the simulations, we use the number ratio of incident C and N atoms 9:2, with which we have confirmed that the values of [N]/[C+N] of the deposited films obtained from the simulation are close to 12 %. We may also supply additional H atoms in our simulation to ensure that deposited N atoms in the polymer have a large number of H atoms in their surroundings and can easily form primary amino groups NH_2 even if incident NH_2 radicals lose some of their H atoms during the deposition process.

Based on the above considerations, we set up 5 different simulation conditions summarized in Table 3.1. For example, in Case I, the simulation begins with an injection cycle of 2 NH_2 radicals to the material surface, followed by another injection cycle of 8 CH_2 radicals, and then an injection cycle of a single ion of $CH_2{}^+$. This set of 3 injection cycles is then repeated 1,000 times. Therefore the flux ratio of $CH_2{}^+$, NH_2, and CH_2 is 1:2:8. The sequence of ion and radical injections is summarized in Fig. 3.3(a)(b). From Cases II to V, we considered different ways to supply more H atoms to the surface.

In our study, we neglect the effects of electron irradiation and the effects of ions for the sake of simplicity. Despite the positive ion incidence upon the surface, electron irradiation can neutralize the surface charge. Indeed incident ions are

generally considered to be charge-neutralized right before or upon the impact due to the Auger effect or electron transfer from surrounding atoms.

The angle of incidence for all ions and radicals is assumed to be normal to the initial substrate top surface (i.e., in the vertical downward direction) for simplicity. The kinetic energy of each radical species is assumed to be 0.2 eV and the ion energy is varied from 0.2 eV to 100 eV. We chose 0.2 eV, rather than typical thermal energy at room temperature of 0.025 eV, to reduce the simulation time by speeding up the motion of slow species without affecting the properties of deposited films.

3.3 Results and discussion

3.3.1 General properties of deposited films

Fig. 3.10 presents the depth profiles of primary amines (NH_2) and secondary amine (NH) densities. Here a primary atom means an N atom that is bonded with two H atoms (and bonded with other atoms or no atom) and a secondary amine means an N atom that is bonded with a single H atom (and bonded with other atoms or no atom) at various incident ion energies. Compared with the atomic densities of C and H given in Fig. 3.4, the amine densities are shown to be much lower.

Overall structures of the deposited films are presented in Fig. 3.4 under the conditions of I (Case I) given in Table 3.1, at different ion incident energies varying from 0.2 eV to 100 eV. The dominant precursors for the film deposition are NH_2

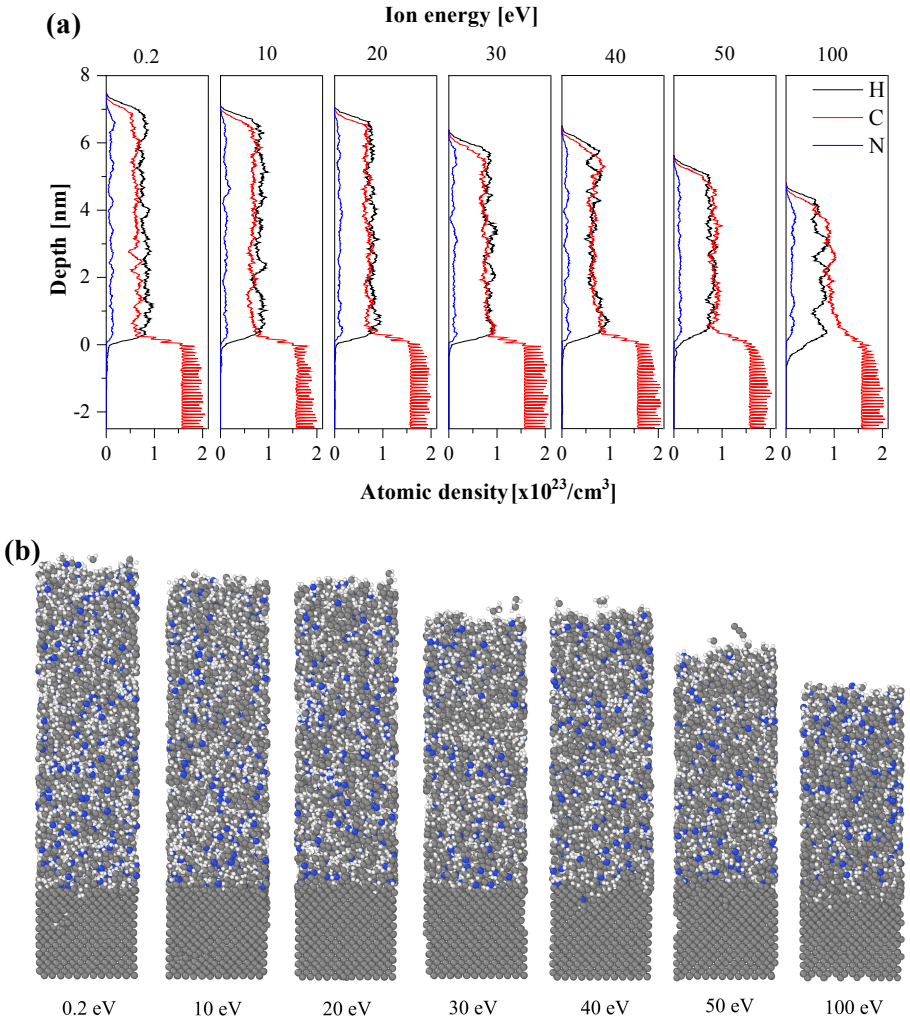

Figure 3.4: (a) Depth profiles of atomic concentrations (i.e., number densities) and (b) representation of MD simulation results with atomic models at different ion incident energies from 0.2 eV to 100 eV for Case I, i.e., the incident radicals are NH_2 and CH_2 and ions are CH_2^+. The ion dose is 2.18×10^{16} /cm^2. In (a), the black, red, and blue curves represent the atomic densities of H, C, and N atoms, respectively. In (b), the gray, blue, and white spheres represent C, N, and H atoms, respectively.

and CH_2 radicals.

The ion dose was 2.18×10^{16} /cm^2 in all cases. The doses of NH_2 and hydrocarbon (i.e., CH_2 or CH_3) radicals are 4.37×10^{16} /cm^2 and 1.75×10^{17} /cm^2 in

all cases.

The depth profiles of atomic concentrations (i.e., number densities) of H (denoted by a black curve), C (red), and N (blue) atoms of deposited films are given in (a). Here the "depth" is defined as the thickness of the deposited film measured from the original position of the C substrate surface. If the depth value is positive, the net deposition of a film takes place. The corresponding atomic-model representations of the deposited films are given in (b). Here the gray, blue, and white spheres represent C, N, and H atoms, respectively.

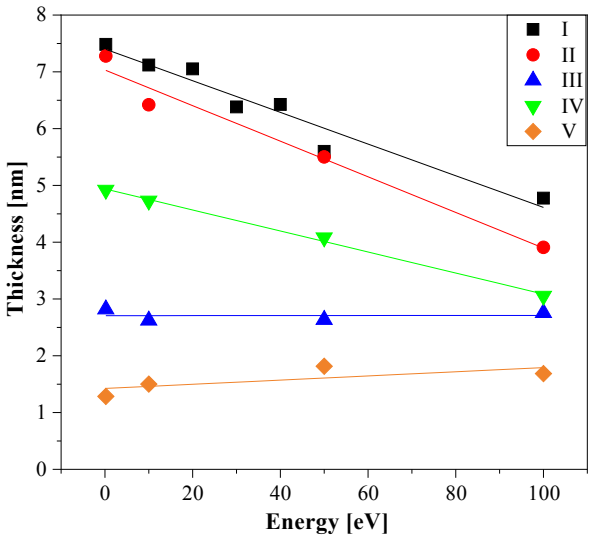

Figure 3.5: Deposited film thicknesses as functions of the ion incident energy for 5 cases given in Table 3.1. The lines are guides to the eye.

It is seen that the film thickness decreases with an increasing ion incident energy, indicating the sputtering of deposited film simultaneously takes place by energetic ion impact. It is also seen in (a) that the average C density slightly increases with the increasing ion energy, i.e., the densification of the deposited film due to the momentum transfer from the incident ions. [132, 133]. It is also seen

that the interface between the deposited film and the substrate becomes rougher as the ion energy increases.

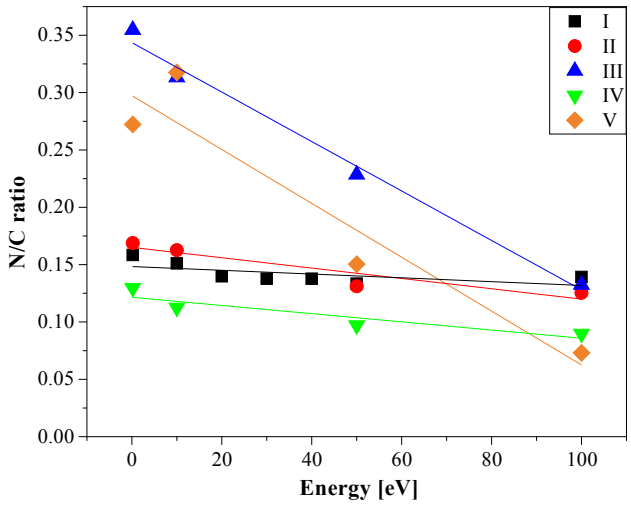

Figure 3.6: The ratio of the atomic concentration (i.e., number density) of N atoms to that of C atoms in the deposited film as a function of the ion incident energy for each case given in Table 3.1. The lines are guides to the eye.

Under the other conditions (i.e., Cases II - V) of Table 3.1, more H atoms are supplied to the surface. Fig. 3.5 compares the deposited film thicknesses among all 5 cases as functions of the ion incident energy. It is seen that the film thickness is largest for Case I, indicating that H atoms have detrimental effects on film deposition, possibly forming volatile hydrocarbon and amino radicals. Desorbed species will be discussed in Subsec. 3.3.3.

It is also seen that the deposited films are substantially thinner in Cases III and V. This is because the sticking probability of CH_3 is much lower than that of CH_2 (because CH_3 has only one dangling bond whereas CH_2 has two), a larger number of incident CH_3 radicals do not stick to the surface and are reflected, compared with the cases of incident CH_2 radicals. The sticking probabilities of CH_2 and CH_3

on a clean C surface of Fig. 3.1 evaluated from our simulation are summarized in the Supplementary Material. In Cases I, II, and IV, where the deposition of CH_2 contributes to the growth of the film, the film thickness decreases with an increasing ion incident energy due to the sputtering of deposited films by energetic ion impact, as discussed earlier.

In all five cases, the ratio of the numbers of incident N and C atoms is 2:9 $\simeq$ 0.22. Fig. 3.6 shows the number ratio of N to C atoms ("N/C ratio")in the deposited films as functions of the ion incident energy for all 5 cases of Table 3.1. It is seen in Cases I, II, and IV, the N/C ratio is lower than 0.22, suggesting that the sticking probability of NH_2 is lower than that of CH_2. In Cases III and V, where C is mostly deposited with CH_3, whose sticking probability is small, the N/C ratio can be higher than 0.22. In all cases, as the incident ion energy increases, the N/C ratio decreases, indicating that N atoms are more easily sputtered off from the surface than C atoms. This is most likely because a C atom can have maximum 4 bonds to form networks in the solid phase whereas a N atom can have maximum 3 bonds and therefore is more weakly bonded with the surface.

The ratio of the number of H atoms to that of all atoms in the deposited film is shown in Fig.3.7 as a function of the incident ion energy for each case of Table 3.1. Although the numbers of H atoms supplied to the surface are significantly higher in Cases IV and V than in other cases, the percentages of H atoms remaining in the deposited films are shown to be relatively similar. As we saw earlier, H atoms can form N or C containing volatile species, so an extra supply of H atoms might have contributed to the additional removal of N and C atoms without increasing their

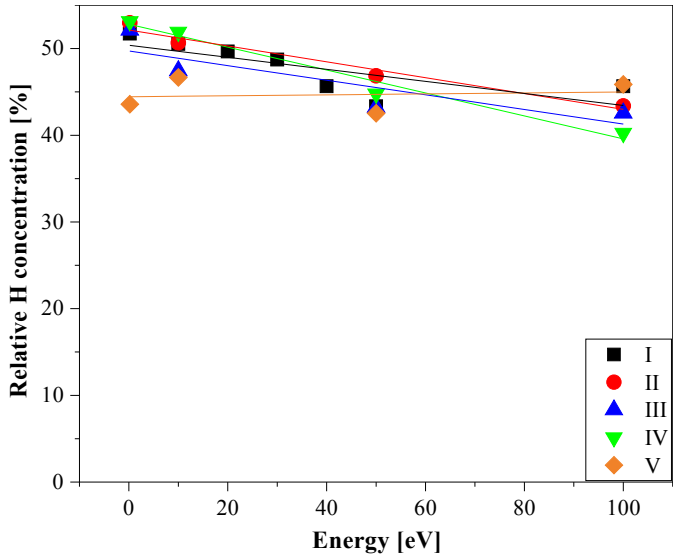

Figure 3.7: The ratio of the number of H atoms to that of all atoms in the deposited film as a function of the ion incident energy for each case is given in Table 3.1. The lines are guides to the eye.

presence in the deposited films. Fig. 3.7 also shows that, in general, the H hydrogen content slightly decreases with an increasing ion incident energy, indicating that H atoms are also prone to sputtering by ion impact.

3.3.2 Formation of amines in the base case

In this section, we focus on Case I and examine how much amine (i.e., NH_2 and NH) is formed in the deposited film. The goal of this study is to find out the optimal conditions for the formation of the primary amine NH_2 in the deposited film. Therefore, in our simulation, unlike experiments, we test the conditions where the number of primary amino groups formed in the film is most likely maximized. One such condition is that we supply N atoms to the surface only in the form of NH_2 radicals. The kinetic energy of radicals is too low to break their N-H

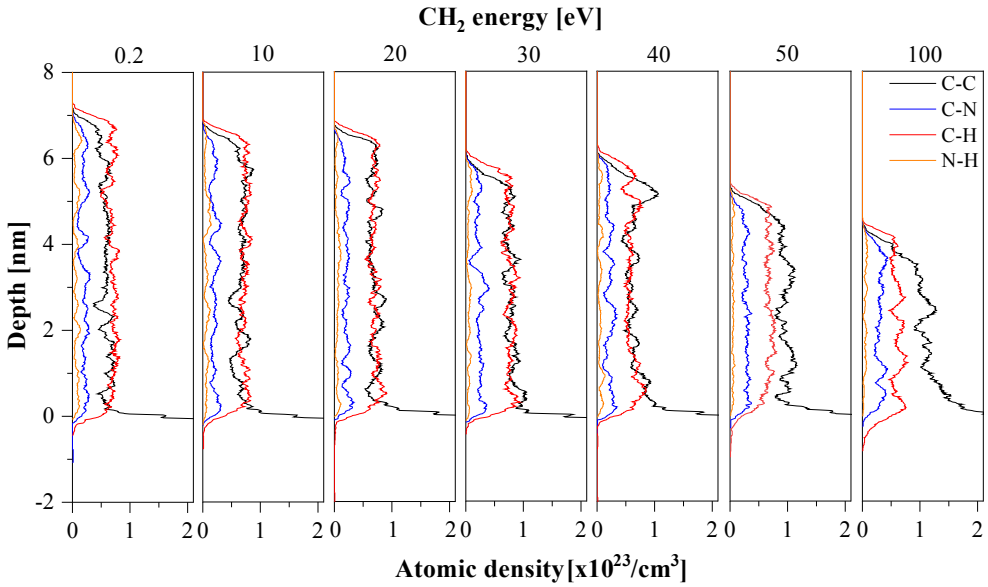

Figure 3.8: Depth profiles of bond concentrations (i.e., the number densities of chemical bonds) at different ion incident energies from 0.2 eV to 100 eV for Case I. Here the profiles of C−C, C−N, C−H, and N−H bonds (all single bonds) are shown. All other bonds, including double and triple bonds, are practically non-existent in the density scale of this figure.

bonds. Therefore, if N-H bonds of the incident NH_2 radicals are broken on the surface (without subsequent energetic ion impact), it must be caused by surface chemical reactions. In such simulation, if we observe the majority of the supplied NH_2 remain as they are and form primary amino groups, the optimal condition for the primary-amine containing polymerization would be to maximize the density of NH_2 radicals in the CVD plasma. If we observe otherwise, the simulation would indicate that the primary amine formation is intrinsically limited in such plasma polymerization due to surface chemical reactions.

Fig. 3.8 plots the depth profiles of the bond densities as functions of the ion incident energy, obtained from MD simulation. The bonds plotted here are C−C,

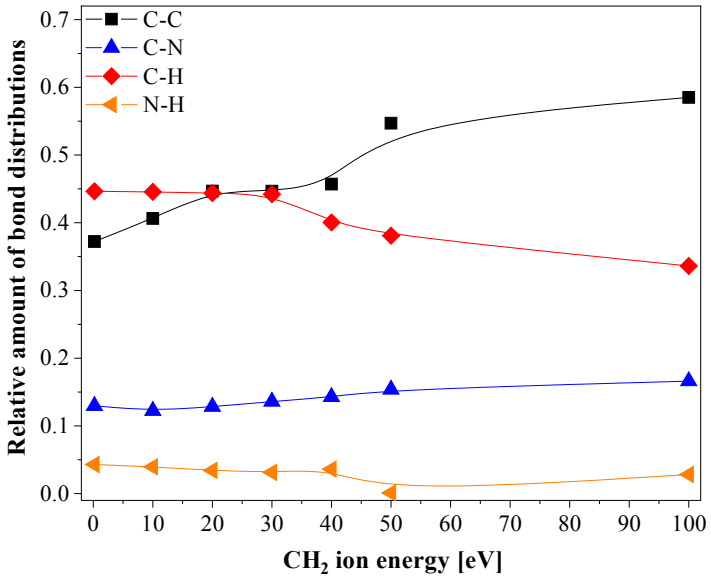

Figure 3.9: Relative bond concentrations averaged over the deposited films as functions of the ion incident energy. All other bonds are practically non-existent in the scale of this figure. The curves are guides to the eye.

C−N, C−H, and N−H, which are the dominant bonds observed in the simulations. These are all single bonds. Other bonds, including double and triple bonds (such as C=C and C≡C), are practically non-existent in the density scale of Fig. 3.8.

Fig. 3.9 shows the relative bond densities averaged over the deposited films among those shown in Fig. 3.8 as functions of the ion incident energy.

It is seen in both Figs. 3.8 and 3.9 that the dominant bonds are C−C and C−H whereas the bond densities of C−H is much smaller than those of C−N bonds, suggesting that the number of primary amines is relatively small. In other words, The majority of incident NH_2 radicals did not remain as they were in the material and changed their chemical structures. It is also seen in Fig. 3.8 that, for high ion incident energies, the density of the C−C bonds increases whereas that

of the C−H bond decreases, indicating the densification of the deposited polymer and preferential sputtering of H atoms.

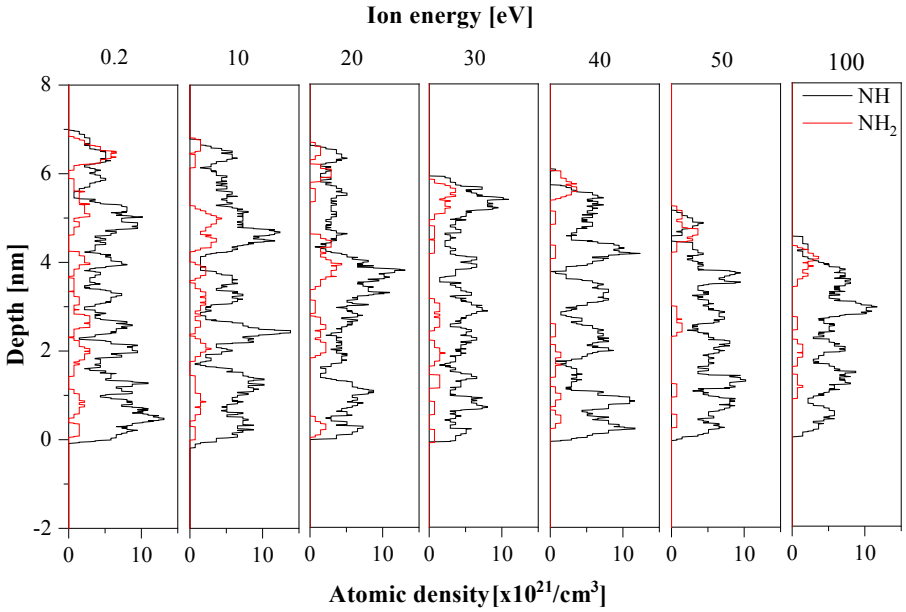

Figure 3.10: Depth profiles of the atomic concentrations of secondary amines NH and primary amines NH_2 at different ion incident energies from 0.2 eV to 100 eV for Case I.

Fig. 3.10 presents the depth profiles of primary amines (NH_2) and secondary amine (NH) densities. Here a primary atom means a N atom that is bonded with two H atoms (and bonded with other atoms or no atom) and a secondary amine means a N atom that is bonded with a single H atom (and bonded with other atoms or no atom) at various incident ion energies. Compared with the atomic densities of C and H given in Fig. 3.4, the amine densities are shown to be much lower.

The total number of primary amines NH_2 normalized by the total number of C or N atoms in the deposited film is plotted as a function of ion incident energy in

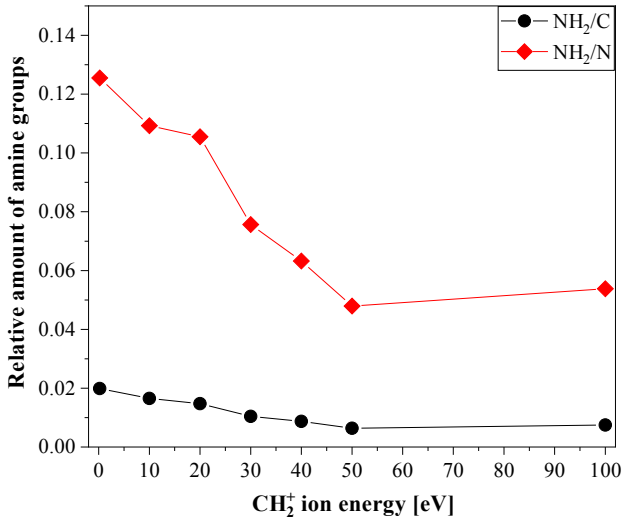

Figure 3.11: Relative concentrations of primary amines NH_2, normalized by the concentrations of C and N atoms separately, averaged over the deposited film as functions of the ion incident energy for Case I. The lines are guides to the eye.

Fig. 3.11. It is seen that, even at low ion incident energy, the density of primary amines is rather low although all N atoms are supplied as NH_2 radicals in the simulation. It indicates that the surface reactions during the deposition process cause the decomposition of incident NH_2 radicals, mostly likely H atoms of incident NH_2 radicals preferentially bonding with surrounding C and H atoms. Thus, the secondary amine -NH is more likely to form on the surface, rather than the primary amine $-NH_2$, when a NH_2 radical approaches a surface with many dangling bonds. For example, if the surface consists of carbon atoms only, the reaction

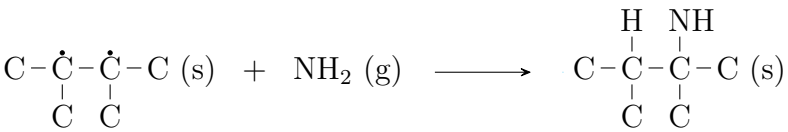

is more likely to take place than

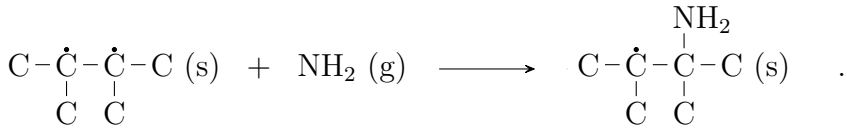

Here (s) or (g) indicates that the corresponding atoms are on the surface or in the gas phase.

The polymerization experiments discussed earlier [10] show that the observed density of primary amines normalized by the number densities of C and N are approximately 8% and 2%. These values are sufficiently close to the values obtained from the MD simulations although the simulation conditions are far more favorable for the primary amine formation.

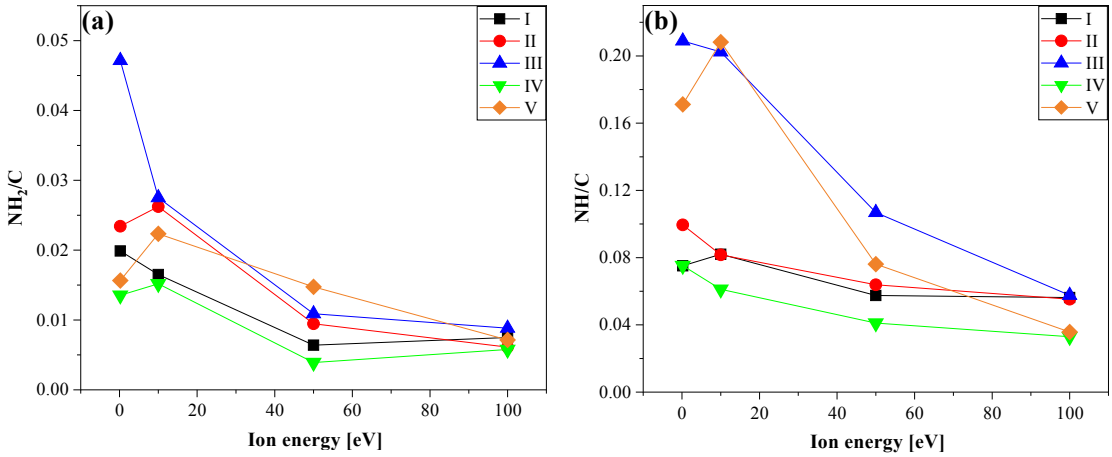

Figure 3.12: Relative concentrations of (a) primary amines NH_2 and (b) secondary amines NH, normalized by the concentrations of C atoms, averaged over the deposited film as functions of the ion incident energy for all cases listed in Table 3.1. The lines are guides to the eye.

Although the densities of secondary amines were not measured experimentally, the numbers of primary and secondary amines normalized by the numbers of C atoms in the deposited films for all cases of Table 3.1 are presented as functions of the ion incident energy in Fig. 3.12. The same quantities normalized with the

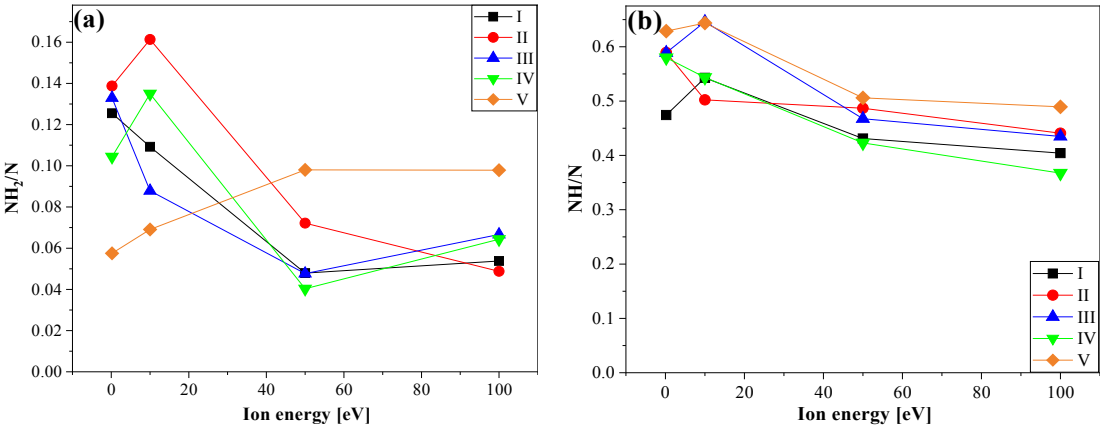

Figure 3.13: Relative concentrations of (a) primary amines NH_2 and (b) secondary amines NH, normalized by the concentrations of N atoms, averaged over the deposited film as functions of the ion incident energy for all cases listed in Table 3.1. The lines are guides to the eye.

number of N atoms in the deposited films are shown in Fig. 3.13, In all cases, it is seen that the number densities of secondary amines NH are much higher than those of primary amines NH_2. Except for some peculiar dependence of these quantities in Cases III and V, where the deposited films are very thin, the relative densities of primary and secondary amines are relatively similar among all cases, showing that incident NH_2 radicals hardly remain as they are as primary amines. The relative densities of primary and secondary amines are relatively low when the incident ion energy is higher than 50 eV. The higher supply of H atoms did not increase the amine density in general.

3.3.3 Desorbed species during deposition

In the previous subsections, we have seen that supplied amino radicals NH_2 hardly remain as they are, even when there is no ion impact (i.e., when the ion energy was set at 0.2 eV). This suggests that a significant rearrangement of bond

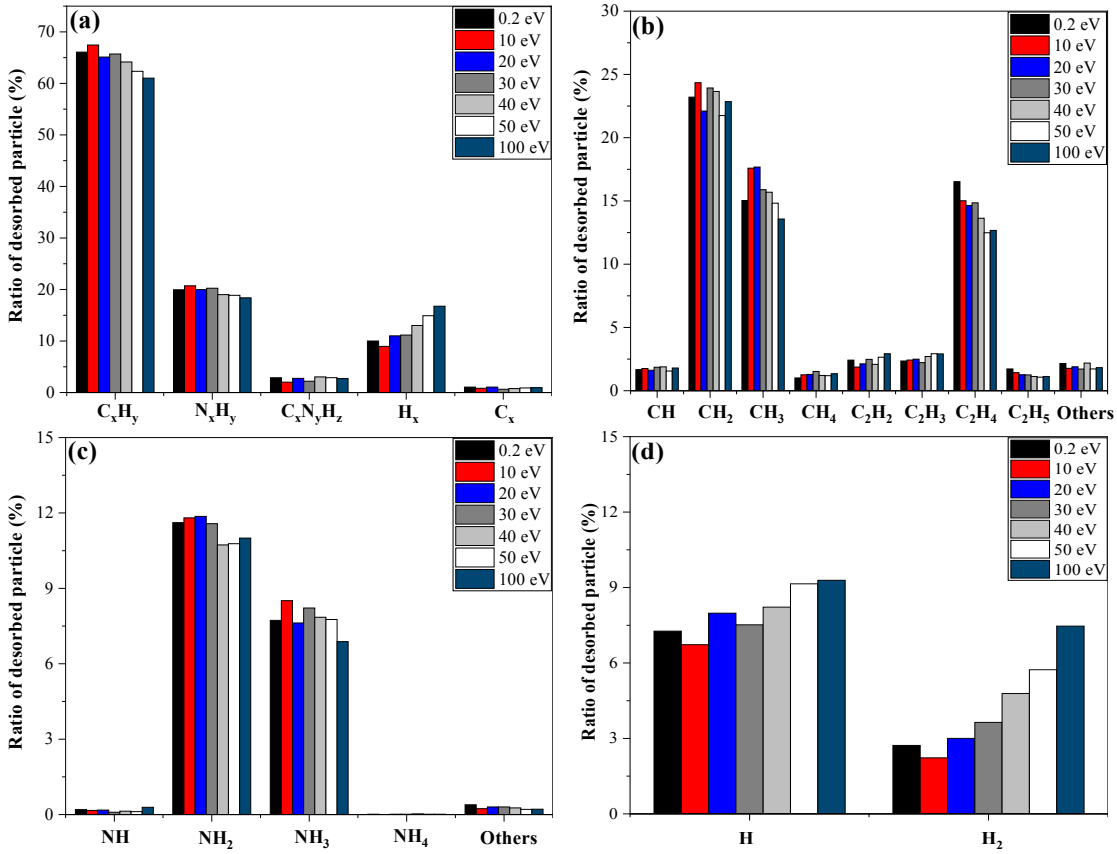

Figure 3.14: Relative numbers of desorbed species during the deposition process at different ion incident energies for Case I. The ratios are relative to the total number of desorbed species during the process. In (a), all desorbed species in forms of C_xH_y, N_xH_y, $C_xN_yH_z$, H_x, C_x (where x, y, $z \geq 1$) are listed. Relative numbers of N_x and C_xN_y species are essentially zero and therefore not listed here. In (b), the relative numbers of desorbed C_xH_y species, each of which is normalized by the total number of desorbed species, are listed. In (c), the relative numbers of desorbed N_xH_y species, each of which is normalized by the total number of desorbed species, are listed. In (d), the relative numbers of desorbed H atoms and H_2 molecules, each of which is normalized by the total number of desorbed species, are listed. It should be noted that reflected species from the incident radicals and ions are also included as "desorbed species" in this figure.

formation takes place among the incident NH_2 and hydrocarbon radicals on the surface. Such surface reactions are often reflected in the desorption species observed during the deposition processes. Fig. 3.14 shows the ratios of desorbed or reflected species among all observed desorbed species at different incident ion

energies in Case I of Table 3.1. It is seen that the dominant species leaving the surface during the deposition processes are CH_2 and NH_2, which are likely to be the reflection of incident radicals. It should be noted that the next dominant desorbed/reflected species are CH_3 and NH_3, which may also be reflected species of incident CH_2 and NH_2 radicals picking up additional H atoms from the surface when they leave the surface. The desorbed C_2H_4 may be formed on the surface when a weakly bonded CH_2 radical is bonded with an incident CH_2 radical or another weakly bonded CH_2 radical on the surface. The fact that, unlike C_2H_4 desorbed species, very few N_2H_4 species are observed as desorbed species indicates that incident NH_2 radicals hardly remain as NH_2 right after they are incorporated into the surface, possibly passing their H atoms to neighboring C or N atoms. Because ammonia NH_3 is volatile, so once NH_3 is formed, it desorbs from the surface.

For all of the desorbed species mentioned above, i.e., CH_2, CH_3, C_2H_4, NH_2, and NH_3, their ratio decreases with the increasing ion energy, indicating that they are reflected of incident radicals species or formed via surface reactions involving only radicals. On the other hand, other desorbed species such as C_2H_2, C_2H_3, H, and H_2 increase their percentages with increasing ion energy, indicating that the removal of H atoms from C_2H_4, preferential sputtering of H atoms, and the formation of H_2 molecules are driven by ion impact.

3.4 Conclusions

We have performed MD simulation to examine surface reactions during plasma polymerization by CH_4/N_2/He plasmas, as in earlier experiments of Ref. [10]. In the experimental study of Ref. [10], although a high amine content in plasma polymerized films was considered preferable, the observed content of primary amines in their deposited films was relatively low.

Therefore, the main question of this study is to find out how one can increase the primary amine content of a plasma polymerized film by adjusting the plasma conditions.

To answer this question, we performed MD simulations under simplistic conditions. Because the primary amine is a functional group of NH_2 bonded with a carbon atom of the polymer, it is natural to assume that, if all N atoms reach the surface as NH_2 radicals at low velocities during the plasma polymerization process, the content of primary amine should be the highest. Therefore, in our simulation, we irradiated a carbon substrate surface with NH_2 and hydrocarbon radicals with occasional ion bombardment at various kinetic energies under 100 eV. If the incident NH_2 radicals remain on the surface as they are, we would observe the highest primary amine content per deposited nitrogen atom. We also examined the cases with additional H atoms supplied to the surface. With additional H atoms, we expect that, if some primary amines NH_2 on the surface lose their H atoms, they could be replenished easily by surrounding abundant H atoms.

Based on these ideas, we set up 5 different conditions for MD simulation. The C to N ratio was selected to be about 4:1 because the concentration ratio of C to N in experimentally observed films in [10] was about 4:1. The flux ratio of ion to C or N containing radicals was set at 1/10 for the convenience of numerical simulation. In reality, the ion-to-radical flux ratio under typical plasmas is considered to be by orders of magnitude smaller. Therefore, the ion impact effects may be overestimated in our simulations if the ion incident energy is the same.

The main observation of our simulations is that, even if we supply all N atoms as NH_2 radicals to the surface at extremely low energy and minimize the ion incident energy, the maximum concentration of primary amines normalized by the concentration of all N atoms was about 12 % without ion impact. With an ion impact of 50 eV or higher, it goes down to about 5%. These values are consistent with the experimental observation of 8% of Ref. [10].

It is interesting to note that, even without ion impact (i.e., with an ion incident energy being close to 0), the primary amine content is low although all N atoms are supplied as NH_2. This indicates that, during the polymerization process where many dangling bonds of C atoms appear dynamically (i.e., many radicals are formed in the deposited films), dangling bonds of C tend to capture H atoms from NH_2.

On the other hand, although the experiments of [10] did not verify, the content of secondary amine NH can be high, as suggested in Fig. 3.13(b); the NH_2/N ratio can be higher 50 % in some cases. Our simulations also indicate that supplying additional hydrogen during the polymerization process does not promote the for-

mation of primary amines. It rather impedes the polymer deposition by breaking C bonds and forming more volatile species.

Based on these observations, we have concluded that the primary amine content of the experiments in Ref. [10], i.e., the NH_2/N ratio being 8%, is probably close to its maximum value that one could achieve under such experimental conditions. Even if we could increase the density of NH radicals in the plasma by some means, we could not expect a significant increase of the primary amines in the deposited film.

Chapter 4

Amine modification of calcium phosphate by low-pressure plasma for bone regeneration

4.1 Introduction

Autogenous iliac bone grafting remains the gold standard for repairing large bone defects caused by trauma or tumors or spinal fusion surgeries. However, the amount of autograft that can be harvested is limited and the harvesting procedure can cause donor site morbidity [143]. To overcome these limitations, the use of artificial bone, in combination with autografts is prevalent. However, the widespread use of artificial bone is hampered by its lack of satisfactory osteogenic ability, despite its superiority in terms of bone conduction and availability [62].

To enhance functionality, surface modification on biomaterials mediated by plasma technology has gained considerable attention. Functional groups created by plasma polymerization (i.e., polymer formation via plasma discharges) can provide selected surface properties such as hydrophilicity/hydrophobicity, cytocompatibility, and bacterial resistance to meet different clinical needs [144]. It was previously reported that plasma treatment of interconnected porous hydroxyapatite (HA) artificial bone with O_2/He gas could improve surface hydrophilicity and promote the osteogenic differentiation of rat bone marrow stromal cells (BMSCs) [8, 9, 64]. However, the O_2/He plasma-treated HA exerted only minimal effects in vivo, possibly owing to the instability of the generated hydroxyl (–OH) groups. In the present study, we focused on the addition of amino groups or amines ($–NH_x$ with $x = 0$–2), which has been suggested to promote cell attachment [40, 44]. Unlike in the earlier studies [9, 64], we used β-TCP, rather than HA. Both are calcium phosphates widely used for artificial bone, but β-TCP is known to have a comparative advantage over HA as being absorbed in vivo (biodegradable) [60]. Using a gas mixture of CH_4, N_2, and He for plasma treatment, we successfully generated amine-containing carbon polymer on the surfaces of β-TCP, including the surfaces of interconnected inner pores of porous β-TCP artificial bones. Here, we demonstrate the effects of amine modification on β-TCP by low-pressure plasma for in vitro cell adhesion, osteogenic differentiation, and in vivo bone regeneration with a rat calvarial defect model.

4.2 Materials and methods

4.2.1 Materials and reagents

Dense and porous disks of β-TCP [$Ca_3(PO_4)_2$] were provided by Coors Tek KK (Tokyo, Japan). All the dense and porous disks used in this study had the same dimensions of 5 mm in diameter and 2 mm in height (ϕ 5 mm $\times$ h 2 mm). The porous disks had well-organized interconnected structures with a porosity of 72–78%, an average pore diameter of 150 μm, and an average diameter of interconnected passages of 40μm [58].

The following culture media were used for in vitro experiments: (1) growth medium (GM) comprising α Eagle's minimal essential medium (α-MEM, Gibco, ThermoFisher Scientific, Waltham, MA, USA) supplemented with 10% fetal bovine serum (Sigma-Aldrich, St. Louis, MO, USA) and 1% antibiotic- antimycotic solution (Sigma-Aldrich); (2) osteogenic differentiation medium (ODM) consisting of GM supplemented with 50 μg/ml L-ascorbic acid 2-phosphate (Sigma-Aldrich), 10 mM β-glycerol phosphate (Merck KGaA, Frankfurt, Germany), and 10 nM dexamethasone (Sigma-Aldrich).

Cell Counting Kit-8 (CCK-8, Dojindo Molecular Technologies, Kumamoto, Japan) was used for the cell proliferation assay. LabAssay ALP (FUJIFILM Wako Pure Chemical Corp., Osaka, Japan) was used for the evaluation of alkaline phosphatase (ALP) activity and BCIP/NBT Color Development Substrate (Promega Corp., Madison, WI, USA) was used for ALP staining. M-PER and Pierce Rapid

Gold BCA Protein Assay Kits (Thermo Fisher Scientific) were used for total protein extraction and quantification, respectively. K-CX AT solution (Falma Co., Tokyo, Japan) was used for the decalcification of in vivo specimens.

4.2.2 Plasma polymerization of β-TCP disks

Plasma polymerization was performed with a bipolar pulsed-plasma deposition system, as shown in Fig. 4.1 (A). The details of the system are described elsewhere [72–74, 145]. The β-TCP disks were placed on the bottom metal (molybdenum) electrode, 190 mm in diameter, connected to the bipolar high-voltage power supply. The applied bipolar pulse voltages were 1.1 and - 1.1 kV (peak-to- peak voltage of 2.2 kV) and the pulse duration was 1 μs for each positive or negative pulse. The power, repetition frequency, and duty cycle were 15 Watt, 5 kHz, and 1%, respectively. The time lapse between a positive pulse and the subsequent negative pulse was 100 μs. The upper metal (aluminum) electrode, 80 mm in diameter, was grounded and the distance between the two electrodes was 38 mm. For plasma polymer deposition, the discharge was generated in a CH_4/N_2/He gas mixture with flow rates of 10, 20, and 10 sccm, respectively, and a gas pressure of 70 Pa. For biological (i.e., in vitro and in vivo) experiments, dense disks were treated only on one side for 30min whereas porous disks were treated on both sides for 60 min (i.e., 30 min each). This is because dense disks were used only for in vitro experiments in this study, where cells were placed only on one side of the disk, whereas porous disks were used only for in vivo experiments in this study, where all sides of the disk were exposed to the animal tissues. In either one-side or both-side plasma treatment, the sidewall of a disk was exposed to the plasma and therefore plasma treated. For

non-biological experiments (e.g., physical or chemical characterization of plasma-polymerized films), the disk was plasma treated only on one side for 30min and the film deposited on the plasma-facing surface or the inner pore surfaces was examined.

4.2.3 Plasma polymer film characterization

The chemical compositions of untreated or plasma-treated β-TCP surfaces were analyzed by X-ray photoelectron spectroscopy (XPS) using ESCA-850 (Shimadzu Co., Kyoto, Japan) with a non-monochromatized Mg-Kα (1253.6 eV) X-ray source at Osaka University, for which the pass energy was 75eV, the photoelectron take-off angle was 90°, and the spot diameter was 8 mm (90% uniformity), or by high-resolution XPS using PHI Quantera II (ULVAC-PHI, Inc., Chigasaki, Japan) with a monochromatic Al- Kα (1486.6 eV) X-ray source at the Foundation for Promotion of Material Science and Technology of Japan (MST), for which the pass energy was 112 eV, the photoelectron take-off angle was 45°, and the spot diameter was 100 μm.

The thickness of a deposited polymer film was evaluated by the standard ellipsometry [146, 147], using data acquired with the V-VASE Ellipsometer (J.A. Woolam, Lincoln, NE, USA) at Central European Institute of Technology (CEITEC), Brno University of Technology, in the spectral range from 0.75 to 6.5 eV at four angles of incidence 60°, 65°, 70° and 75°.

The detection of primary amine groups (–NH_2) on plasma-treated disk surfaces was performed using the standard derivatization with 4-trifluoromethyl-

benzaldehyde (TFBA), according to the published method [75, 148]. The derivatization reactions of TFBA vapors with plasma-treated disk surfaces were allowed to occur in an Ar atmosphere (Ar flow rate of 60 sccm at atmospheric pressure) at room temperature (approximately 25°C) for 4 h inside the glove box. The relative concentrations of primary amines on the sample surfaces were determined by the detection of fluorine (F) atoms of TFBA with ESCA-850 XPS analysis after the derivatization reactions. The surface morphologies of untreated and plasma-treated porous β-TCP disks were observed with a scanning electron microscope (SEM) (S-4800, Hitachi, Ltd., Tokyo, Japan) at Osaka University.

4.2.4 Cells

Rat BMSCs were obtained from the bone shafts of the femora of four 3-week-old green fluorescent protein (GFP)-transgenic male Sprague-Dawley rats (SD-Tg (CAG-EGFP) rats, Japan SLC, Hamamatsu, Japan). Following the sacrifice of the rats using CO_2 inhalation, both ends of the femur were removed from the epiphysis; the marrow was flushed out using 10 ml of GM expelled from a syringe through a 21-gauge needle according to the previously described method [148]. The released cells were collected in two 100 mm culture dishes containing 15 ml of GM. The medium was changed after 24 h to remove hematopoietic cells and renewed twice weekly. Cultures were maintained in a humidified atmosphere of 95% air with 5% CO_2 at 37°C. When the cells reached 80–90% confluency they were washed with phosphate-buffered saline (PBS) and trypsinized with 1% trypsin-ethylenediaminetetraacetic acid (EDTA). Following centrifugation for 5 min at 400 g, the cells were resuspended and plated at a density of $3.6 \times 10^4/\mathrm{cm}^2$. After

again reaching confluency, cells were collected and stored at - 80°C (Passage 1). Prior to in vitro experiments, stocked cells were thawed and resuspended in 15 ml of GM, then plated in a 100 mm dish and cultured for three days to reach 80-90% confluency (Passage 2).

4.2.5 Cell adhesion assay

A centrifugation cell adhesion assay was performed according to a published method [149]. Cell suspension (5×10^3 cells/35 μl GM) was gently dropped on each dense β-TCP disk surface to form a centroclinal water drop and incubated for 30 min in a 24 well culture plate to initiate adhesion. Then, 1 ml of PBS was gently added to each well containing a cell-adhered disk and macro fluorescence photos were taken with the Leica AF6000 Fluorescence Imaging System (Leica Microsystems, Wetzlar, Germany. Exposure: 1000 ms; Gain: 2.7; Binning 2×2; Magnification: 12.6×) to quantify the initial adherent cells. After this, the cell adhered disks were embedded into a 48-well culture plate containing 100 μl of Vaseline (KENEI Pharmaceutical Co., Ltd., Osaka, Japan) in each well. After filling each well with PBS, the plate was sealed with a sealing tape and set upside-down on a centrifuge (PlateSpinII, Kubota Corp., Tokyo, Japan) and centrifuged at 10 g for 5 min to detach weakly adherent cells. After the centrifugation, the detached cells were slowly aspirated and each well was carefully filled with 200 μl of PBS. Macro fluorescence photos of the plate were taken again under the same conditions as those prior to the centrifugation. Automatic cell counting was performed with the macro fluorescence photos and ImageJ software [150]. The adhesion rate is defined as the ratio of the number of cells attached to the surface

after centrifugation to that before centrifugation.

4.2.6 Morphology analysis of adhered cells

Cell suspension (5×10^3 cells/35 μl GM) was gently dropped on dense β-TCP disks and incubated for 3 h in a 24-well culture plate to initiate adhesion. Then, the wells were slowly filled with 1 ml of GM, and the incubation was continued for another 24 h. Macro fluorescence photos of random areas of the culture wells containing incubated cells were then obtained. The open-source software CellProfiler (www.cellprofiler.org) [151] was used for sorting cells and cell morphology analysis. In particular, the cell area was measured to quantify the spreading of attached BMSCs. Two cell-shape descriptors (circularity and solidity) were investigated; the circularity indicates the closeness of the cell shape to a perfect circle, and the solidity is an index to quantify the amount and size of concavities of the cell [152]:

$$Circularity = \frac{4\pi A}{P^2} \tag{4.1}$$

where A is the cell area and P is the perimeter.

$$Solidity = \frac{A}{ConvexA} \tag{4.2}$$

where *ConvexA* is the area of the smallest convex hull that contains the cell.

4.2.7 Cell proliferation assay

To balance the initial cell count of adherent cells on untreated and plasma-treated β-TCP disks, two different concentrations (5×10^3 cells/35 μl GM for the untreated group and 3×10^3 cells/35 μl GM for the plasma-treated group) of cell suspension were dropped on dense untreated and plasma-treated β-TCP disks in a 48-well plate. After incubating for 30 min, 500 μl of GM was slowly added to each well. At days 1, 3, 5, 7, 11, and 14, 50 μl of CCK-8 solution was added to each well and the plate was incubated for 2 h, then 100 μl of GM from each well was transferred into a 96-well plate. The optical density at 450 nm was measured using a spectrophotometer (Multiskan GO, Thermo Fisher Scientific).

4.2.8 Osteogenic differentiation assay

Cell suspension (2×10^4 cells/35 μl GM) was dropped on dense β-TCP disks and incubated for 30 min in a 48-well plate to initiate adhesion. Then, 500 μl of GM was slowly added into each well, incubated for 24 h, and the culture medium was replaced with ODM for osteogenic differentiation. The subculture was maintained for another four days. After washing the disks twice with PBS, the attached cells were fixed using 500 μl of 4% paraformaldehyde (PFA) for ALP staining, according to the manufacturer's instructions (Promega Corp.). For ALP activity, 60 μl of M-PER was added to each well and the cells were detached from the disks using a mini scraper. After lysing the cells for 5 min, the supernatant was collected for ALP and total protein assays. An ALP activity unit was defined as the release of 1 nmol p-nitrophenol per min of incubation at 37°C for each β- TCP disk. The

total protein content of each sample was measured to standardize the ALP activity values.

4.2.9 Rat calvarial defect model

A total of 20, 8-week-old male Sprague-Dawley rats (Charles River Laboratories Japan, Yokohama, Japan) were used to generate the calvarial defect model. Anesthesia was maintained by intraperitoneal injection of a mixture of 0.15 mg/kg medetomidine, 2.0 mg/kg midazolam, and 2.5 mg/kg butorphanol after introducing anesthesia by inhalation of 5% isoflurane. A 1.5 cm longitudinal incision was made at the center of the vertex and two full-thickness bone defects with a diameter of 5 mm were then carefully created using a high-speed trephine burr under constant irrigation with saline to avoid heat injury of the surrounding tissue. The plasma-treated and untreated β-TCP disks were implanted in the right and left defects, respectively. The rats were given free access to water and food after the surgery. The rats were sacrificed at postoperative 3 (n = 5) and 6 (n = 15) weeks by CO_2 inhalation. Microfocus computed tomography (micro-CT) and histological analyses were performed to evaluate new bone formation in the inner pores of porous β-TCP disks at 3 and 6 weeks postoperatively.

4.2.10 Microfocus computed tomography (micro-CT)

Harvested specimens were fixed in 10% buffered formalin, dehydrated and degreased using a graded ethanol series, and stored in 70% ethanol at 4°C for micro-CT scanning (Skyscan 1272 micro-CT, Bruker, Kontich, Belgium), which was

performed with the following parameters: camera binning = 2×2, source voltage = 80 kV, source current = 125 μA, image pixel size = 4 μm, rotation step = 0.6°, and filter = Al 1 mm. Image analysis was performed using CTAN software (Version 1.18.8.0+, Brucker). Micro-CT images of the specimens were compared with the results of histological evaluation of the specimens, discussed below, and the difference in image intensities between the newly formed bone and residual β-TCP was identified. Using this information, three-dimensional (3D) images of newly formed bones inside the porous β-TCP disks were reconstructed from the Micro-CT images of the specimens.

4.2.11 Histological evaluation

After micro-CT scanning, the specimens were demineralized using K-CX AT solution at 4°C, cleared in xylene, and embedded in paraffin. Then, several sections of 4 μm thickness were cut off from the center of each specimen and stained with hematoxylin and eosin (H and E).

4.2.12 Statistical analysis

Statistical analysis was performed using GraphPad Prism version 7.04 for Windows (GraphPad Software, San Diego, CA, USA) applying the Mann–Whitney U test for non-parametric data, Student's or Welch's t-test for parametric data, and Wilcoxon matched-pairs signed-rank test for in vivo results. The values are presented as mean ± standard deviation (SD). The differences were considered statistically significant for p-value < 0.05.

4.2.13 Ethic declarations

All animal work was approved by The Animal Experimental Committee of Osaka University Graduate School of Medicine (01-070-000) and restrictedly followed ARRIVE guidelines and the National Institutes of Health Guide for the Care and Use of Laboratory Animals [153].

4.3 Results

4.3.1 Plasma polymerization on β-TCP disks

A bipolar pulsed-plasma deposition system developed at Osaka University was used to perform plasma polymerization on dense and porous β-TCP disks. The schematic diagram of the system is given in Fig. 4.1A. The plasma was generated with a CH_4/N_2/He gas mixture with flow rates of 10, 20, and 10 sccm, respectively, and a gas pressure of 70 Pa. Methane (CH_4) was used to form an organic polymer, nitrogen (N_2) was to form amine groups, and helium (He) was to lower the plasma ignition voltage via Penning ionization. The plasma polymerization conditions used in this study, including the selection of the discharge gases and their mixing ratio, were selected to attain stable plasma discharge, a reasonable film deposition rate, and a relatively high amine concentration in the deposited film, using the gas species and discharge conditions that the authors are accustomed to operating the plasma system with for various other plasma polymerization applications [145, 154]. Although the conditions used in this study were locally optimized (i.e.,

by varying the discharge parameters around those presented in this article), its global optimization with different combinations of organic and nitrogen-compound gaseous species has not been performed yet and is beyond the scope of the present study.

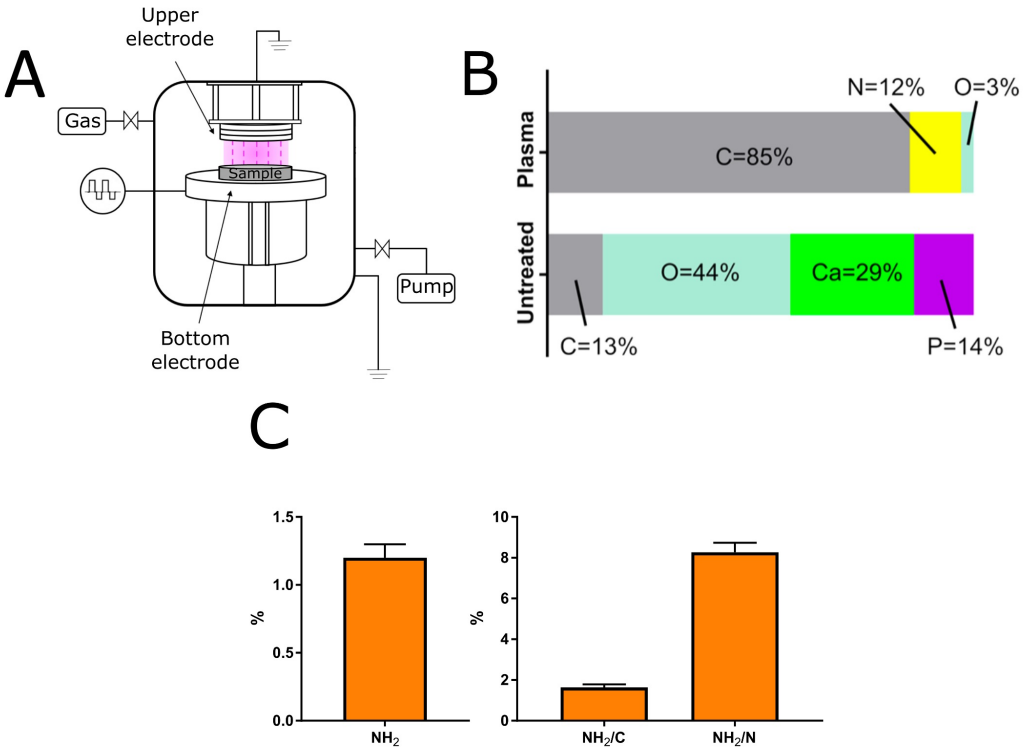

Figure 4.1: Plasma polymerization system and characterization of plasma-polymerized films. (A) Schematic diagram of the pulsed-plasma deposition system used in this study. Samples were placed on the bottom metal electrode, which was powered by high-voltage bipolar pulse voltages with a peak-to-peak voltage of 2.2 kV. The power, repetition frequency, and duty cycle were 15 W, 5 kHz, and 1%, respectively. The plasma was generated from a gas mixture of CH_4, N_2, and He with flow rates of 10, 20, and 10 sccm, respectively, and a gas pressure of 70 Pa. (B) The atomic concentration ratios on a plasma-treated dense β-TCP disk surface (top) and those on an untreated dense β-TCP disk surface (bottom). More precise values are given in the main text. (C) The relative number of primary amines ($-NH_2$) among all atoms excluding hydrogen (left) and the number ratios of primary amines to C or N atoms (right) on the surface of the plasma-polymerized film deposited on a dense β-TCP disk. In (B,C), all measurements were triplicate.

The chemical compositions of the untreated dense β-TCP disk obtained from XPS are Ca: P: O: C = 28.5 ± 0.2: 14.0 ± 1.5: 44.0 ± 0.6: 13.5 ± 2.2 (at.%), and those of the untreated porous β-TCP disk are Ca: P: O: C = 18.9 ± 1.1: 10.8 ± 0.6: 42.3 ± 3.9: 28.0 ± 1.6 (at.%). The measurements were performed in triplicate, i.e., n = 3. No nitrogen (N) was observed on the disk surfaces. It should be noted that hydrogen (H) cannot be detected by XPS and carbon (C) on the surface is essentially a contaminant from ambient air. Compared with the stoichiometric ideal β-TCP (Ca:P:O = 23.1:15.4:61.5), both dense β-TCP disk (Ca:P:O =33.0:16.1:50.9) and porous β-TCP disk (28.8:16.4:54.9) have Ca-rich compositions. The difference in chemical compositions between dense and porous β-TCP disks is considered to be caused by their different manufacturing processes.

The chemical compositions of the plasma-treated dense β-TCP disk obtained from XPS are Ca: P: O: C:N = 0.0 ± 0.0: 0.0 ± 0.0: 2.9 ± 0.2: 85.2 ± 0.1:11.9 ± 0.1 (at.%, n=3). The N to C ratio of the deposited film is, therefore, N/C = 14.0 %. The fact that neither Ca nor P was observed indicates that the deposited film was sufficiently thick (thicker than several nm at least). The observed small amount of O may indicate oxygen incorporated in the deposited film due to oxygen or water impurities off from the chamber walls of the plasma system during the plasma discharge or water (H_2O) molecules attached to the polymer surfaces when the sample was exposed to ambient air. The results are summarized in Fig. 4.1B.

It is not easy to measure the thicknesses of deposited polymer films on β-TCP precisely as the roughness of β-TCP surfaces is far greater than the deposited film thickness. However, we surmise that the deposited polymer thickness on the β-

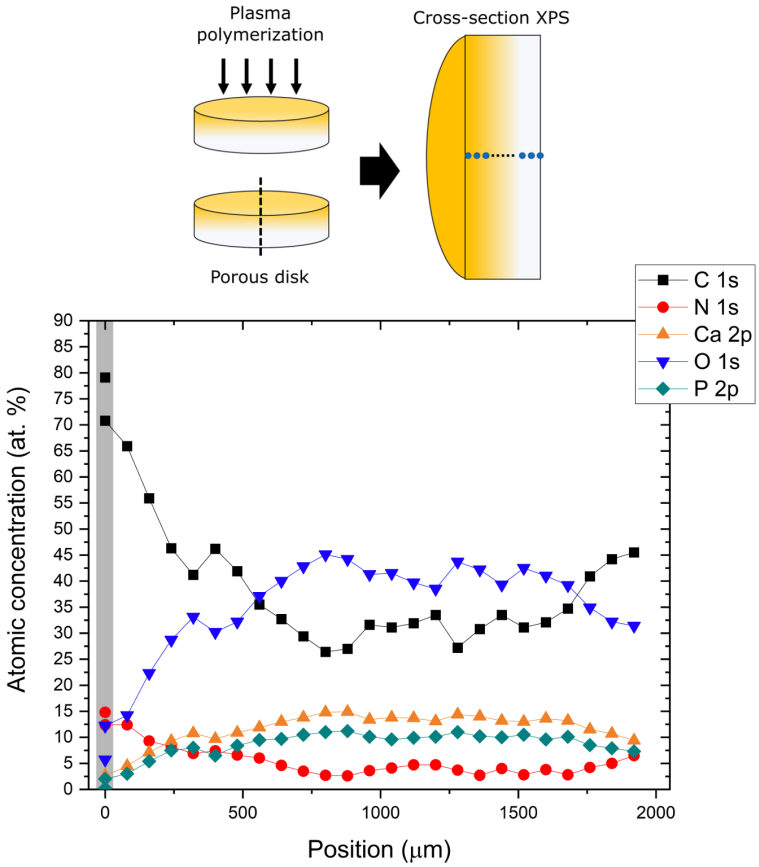

Figure 4.2: The profiles of relative atomic concentrations along the center axis of a plasma-treated porous β- TCP disk, indicating plasma polymerization of the inner pore surfaces due to the penetration of plasma-generated deposition precursors through the interconnected pores from the plasma-treated disk surface. After a single side of a porous β-TCP disk was plasma-treated, it was cut in half through its center, and the relative atomic concentrations were measured at 25 points along the center axis. The horizontal axis of the figure represents the position along the center axis measured from the plasma-exposed top surface of the disk. In each case above, the plasma treatment time was 30 min.

TCP disk under the conditions described above (i.e., 30 min polymerization) was about 40 nm, based on the thickness of the plasma-polymerized film formed on a crystalline (100) Si surface under the same polymerization conditions, which was determined to be 44.2 $\pm$ 0.1 nm (n=3) by ellipsometry.

The relative amount of primary amine (–NH_2) on a plasma-polymerized film surface was evaluated by the derivatization method [75, 155]. Fig. 4.1C shows the relative number of N atoms that form primary amine groups on the surfaces of plasma-polymerized films deposited on dense β-TCP disks 2 days after the film deposition. The left graph shows the atomic percentage of such N atoms among all surface atoms excluding hydrogen (i.e., the relative number of primary amines among all surface atoms excluding hydrogen), which is 1.2 ± 0.1 (at.%, n=3). The right graph shows the number ratios of primary amines to the surface C or N atoms, i.e., NH_2/C=1.6 ± 0.1 and NH_2/N = 8.3 ± 0.5 (at.%, n =3). It is seen here that about 8% of all deposited N atoms formed primary amines in the plasma-polymerized film. The remaining N atoms were most likely to form either secondary amines (-NH) or tertiary amines, i.e., nitrogen atoms bonded only with carbon atoms.

To observe whether the polymer depositing plasma penetrated the interconnected pores of artificial bone and coated their inner surfaces, we performed a cross-section analysis of a plasma-treated porous β-TCP disk. In this analysis, a single-side treated porous β-TCP disk was cut in half at the center and the cross sections were scanned with high-resolution XPS. The measurements were performed on 25 spots with a diameter of 100 m along the center axis of the cross-section, as presented in Fig. 4.2. The vertical and horizontal axes represent the percentages of atomic concentrations and the position along the center axis measured from the plasma-exposed top surface of the disk. We treated only a single side of the disk such that the penetration direction became clear. The untreated side of the disk was in direct contact with the electrode surface of the

plasma system and not directly exposed to the plasma.

As seen in Fig. 4.2, the C and N concentrations are the highest on the plasma-treated surface (i.e., at position 0) and decrease gradually toward the center. The fact that their concentrations are slightly higher near the untreated side (i.e., near position 2 mm) suggests that some polymerizing gas entered from this side through a gap between the bottom surface of the disk and the electrode. Because the porosity of the disk is about 75 % (i.e., 75 % of the disk volume is void), we expect that the area ratio of the inner pore surface to the β-TCP bulk on the cross-section is approximately 752/3: 252/3 = 68: 32. We also note that the variation of atomic concentration ratios on the cross-section is higher than the SD of the atomic concentration ratios on the untreated β-TCP surface given above. This is because of the random spatial distribution of inner pores, whose average diameter is 150 μm, inside the disk whereas the diameter of each measurement spot is 100 μm.

As discussed earlier, the atomic concentration ratios of untreated β-TCP were about Ca: P: O: C: N = 19: 11: 42: 28: 0 (at. %). Even in a deeper region of the cross-section (e.g., the region from 800 to 1700 μm) of Fig. 4.2, the atomic concentrations of C and N are higher than those of untreated β- TCP, and those of Ca and P are lower, which indicates that plasma-polymerized films were also deposited on the inner pore surfaces of the deep region of the disk. Plasma-treated porous β-TCP disks used for in vivo experiments of this study were treated on both sides (for 30 min each), as discussed before, so we expect the inner pores of those disks are well coated with plasma-polymerized films.

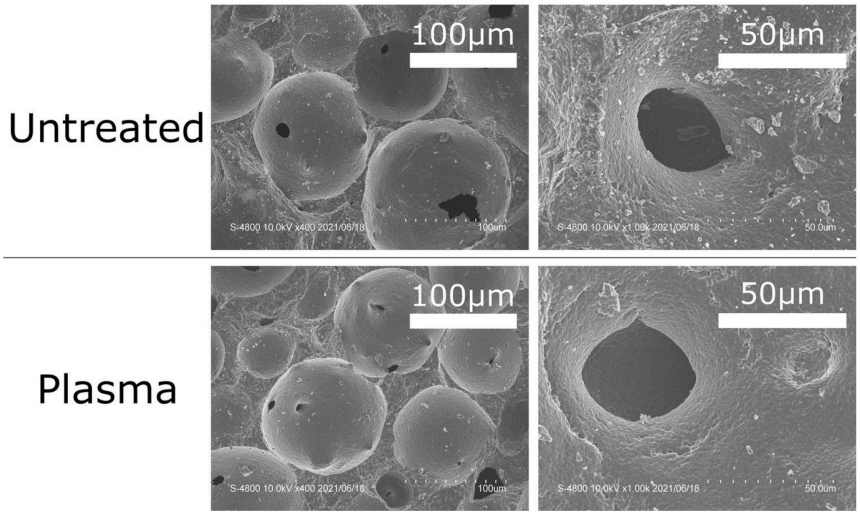

Figure 4.3: SEM images of the outer surfaces of untreated (top) and plasma-treated (bottom) porous β-TCP disks. Low magnification = $\times$ 400 (left). High magnification = $\times$ 1000 (right).

SEM photos of outer surfaces of untreated and plasma-treated porous β-TCP disks are shown in Fig. 4.3. Plasma polymerization did not cause structural changes in the porous disks. Typical interconnecting channels are shown in photos at $\times$ 1000 magnification. The deposited polymer is not visible here because its thickness (about 40 nm, as discussed above) is far smaller than the scales of these images.

4.4 Effects of plasma treatment on cell behaviors

First, we confirmed that the plasma treatment enhanced the hydrophilicity of β-TCP, which was originally hydrophobic. As a result, cell suspension dropped on

plasma-treated porous disks infiltrated quickly, and the cells therein adhered to the walls of their deep inner pores. Second, we investigated the effects of the plasma treatment on cell adhesion. Green fluorescent protein (GFP)- transgenic bone marrow stromal cells (GFP-BMSCs) were harvested from male GFP-transgenic rats. We seeded 5×10^3 GFP-BMSCs on the surface of each dense β-TCP disk, incubated them for 30 min to initiate adhesion, and then detached weakly attached cells by centrifugation, as shown in Fig. 4.4A. Figure 4.4B shows fluorescence photos of rat BMSCs attached to dense β-TCP disks before and after centrifugation. As shown in Fig. 4.4C, both cell counts and adhesion rates were significantly higher for the plasma- treated disks than those of the untreated disks.

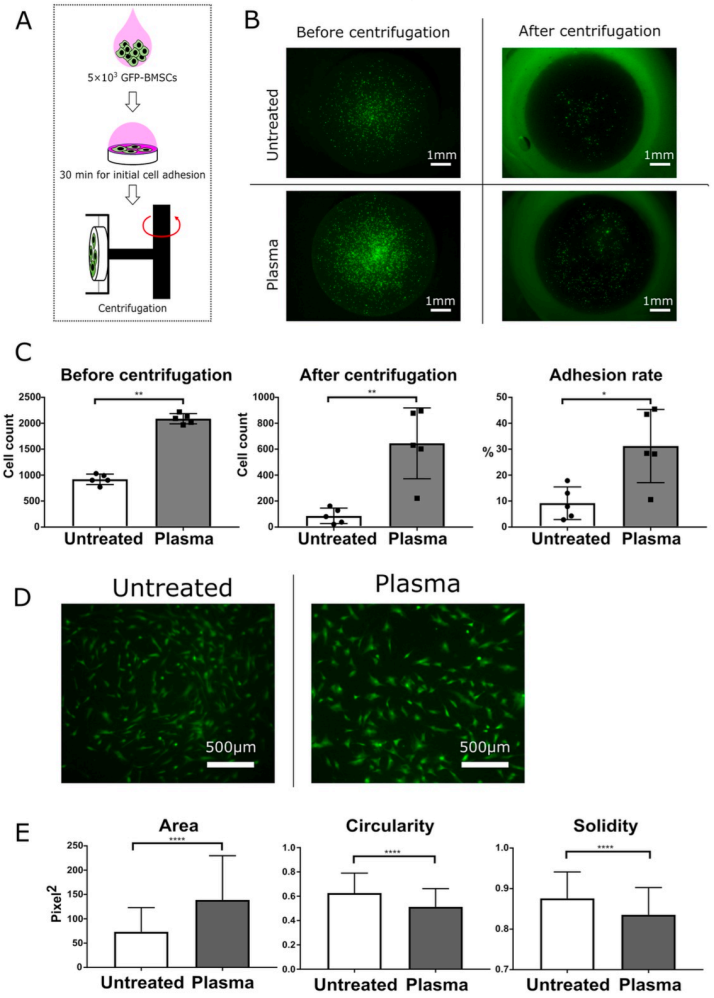

Figure 4.4: Cell adhesion and morphology assays. (A) Schematic diagram of the experimental setup for cell adhesion assay. (B) Fluorescence photos of rat BMSCs attached to untreated (top) and plasma-treated (bottom) dense β-TCP disks before (left) and after (right) centrifugation. (C) The average numbers of cells attached to each dense β disk after initial adhesion but before centrifugation (left), those after centrifugation (center), and the adhesion rates (right) for untreated and plasma-treated dense β-TCP disks. The data for C are expressed as mean ± SD (n = 5). *p < 0.05, ** p < 0.01. Mann– Whitney U test. Cell morphologies of rat BMSCs attached to dense β-TCP disks were also analyzed after 3 h incubation for the initial adhesion and subsequent 24-h incubation with additional GM. (D) Fluorescence photos of the rat BMSCs after the incubation on untreated (left) and plasma-treated (right) dense β-TCP disks. (E) Comparison of cell areas (left), cell circularities, defined by 4.1 (center), and cell solidities, defined by 4.2 (right), between the untreated and plasma-treated disks. The cell area represents its size and the cell circularity and solidity characterize its shape. The data of E are expressed as mean ± SD with n = 1860 for "untreated" and n = 1440 for "plasma". ****p < 0.0001. T-test.

Additionally, we also analyzed morphologies of rat BMSCs attached to dense β-TCP disks. We seeded 5×10^3 GFP-BMSCs on the surface of each dense β-TCP disk and incubated them for 3 h for initial adhesion. The cells were then further incubated with additional GM for 24 h. Fig. 3D shows fluorescence images of the cells after the 24 h incubation. It is seen there that the morphology of attached cells on the plasma-treated β-TCP disk exhibits a significant increase in the area of cytoplasm (shown in green in the images). These images are used to evaluate the cell areas, cell circularities, defined in 4.1, and cell solidities, defined in 4.2, for the untreated and plasma-treated disks, which are shown in Fig. 4.4E. It should be noted that the sample numbers for the untreated and plasma-treated cases are n = 1884 and n = 1440, respectively, for the analysis of Fig. 4.4E, and the differences in the mean values are confirmed to be statistically significant with unpaired t-test analysis. As we visually observed in Fig. 4.4C, Fig. 4.4E shows that the average area of rat BMSCs is larger on the plasma-treated dense β-TCP disk than on the untreated disk (left), suggesting the enhancement of cell spreading on the plasma-treated surfaces. It also shows that the average circularity (center) and solidity (right) are lower on the plasma-treated dense β-TCP disk than on the untreated disk, indicating the presence of membrane protrusions of rat BMSCs on the plasma-treated dense β- TCP disk.

Third, we performed cell proliferation assays. Considering the difference in the initial cell adhesion, we made the initial number of cells the same by seeding different numbers of GFP-BMSCs on plasma-treated and untreated dense β-TCP disks and plotted the cell proliferation curves by serial Cell Counting Kit-8 (CCK-8) assays (Fig. 4.5A). It was found that the plasma treatment did not influence

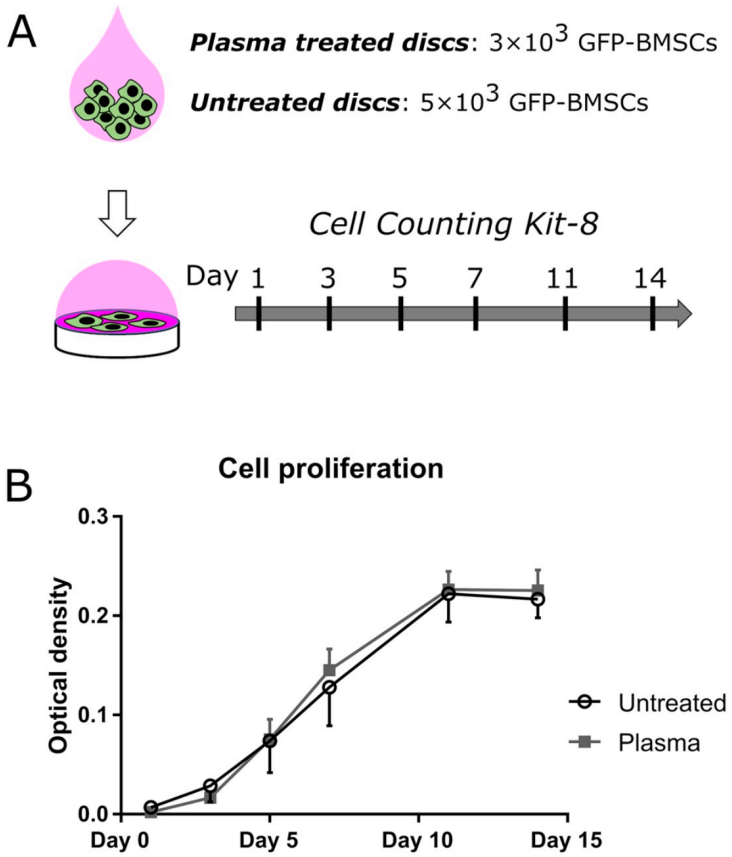

Figure 4.5: Proliferation assay for rat BMSCs on untreated and plasma-treated β-TCP disks. (A) Schematic diagram of the proliferation assay. (B) Cell proliferation curves for rat BMSCs on untreated (open circles) and plasma-treated (filled squares) β-TCP disks. All measurements were triplicate.

cell proliferation (Fig. 4.5B).

Last, to evaluate the overall osteogenesis including cell adhesion, proliferation, and osteogenic differentiation on plasma-treated and untreated dense disks, we seeded 2 × 104 GFP-BMSCs on the surface of each dense disk and performed ALP assays after 5 days of osteogenic induction (Fig. 5A). The plasma treatment significantly improved osteogenesis as demonstrated by ALP staining (Fig. 5B) and ALP activity assay (Fig. 5C).

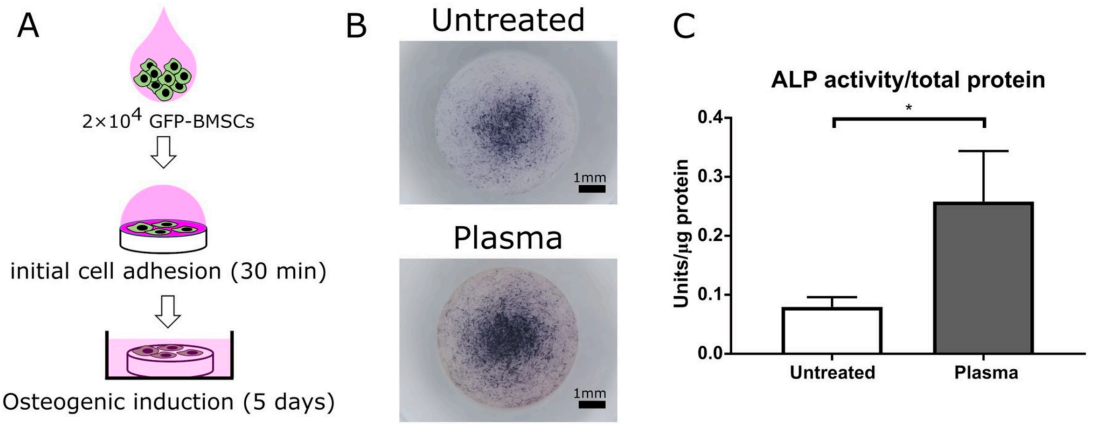

Figure 4.6: Osteogenic differentiation assay for rat BMSCs on untreated and plasma-treated β-TCP disks. (A) Schematic diagram of the osteogenic differentiation assay. (B) Macro photos of ALP-stained rat BMSCs sub- cultured on untreated (top) and plasma-treated (bottom) dense β-TCP disks. The black in the image represents the ALP stain. (C) The ALP activity values, as defined in the section Materials and methods, for untreated and plasma-treated β-TCP disks. The data here are expressed as mean $\pm$ SD (n = 3). *p $<$ 0.05. T- test.

4.5 Enhancement of in vivo new bone formation by the plasma treatment

Plasma-treated and untreated porous β-TCP disks were symmetrically transplanted into circular bone defects of rat calvarial bones. Histological evaluation and micro-CT analysis were performed at 3 and 6 weeks postoperatively (Fig. 4.7A). As seen in Fig. 4.7B, at postoperative 3 weeks, the volume of new bone formed inside the plasma- treated porous β-TCP disk was evaluated and found not to differ essentially from that inside the untreated porous β-TCP disk. However, at postoperative 6 weeks, the volume of new bone formed inside the plasma- treated porous β-TCP disk was significantly higher than that inside the untreated porous β-TCP disk. The 3D-reconstructed image of new bone along with the host calvarial bone

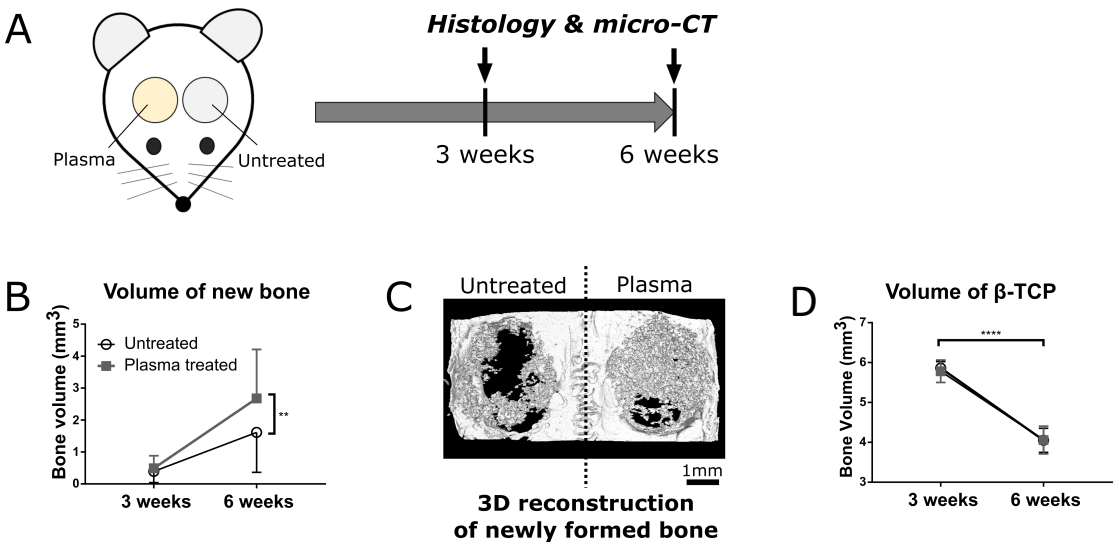

Figure 4.7: In vivo experiments on the new bone formation inside porous β-TCP disks. (A) Schematic diagram of the in vivo implantation of porous β-TCP disks and post-operative evaluations. (B) Micro-CT analysis of new bone volumes formed inside the untreated (open circles) and plasma-treated (filled squares) porous β- TCP disks at postoperative 3 and 6 weeks. (C) The 3D reconstruction of the calvarial bone implanted with untreated (left) and plasma-treated (right) porous β-TCP disks at postoperative 6 weeks. The gray grain- like structures indicate newly formed bone, and the white plate or slab-like structure with two circular holes represents the rat calvarial bone. The β-TCP disks are not depicted and therefore the volume occupied by β-TCP is represented by void space (black) in this image. (D) Micro-CT analysis of residual β-TCP volumes of the untreated (open circles) and plasma-treated (filled squares) porous β-TCP disks at postoperative 3 and 6 weeks. The data in B and D are expressed as mean $\pm$ SD (n = 5 for 3 weeks, n = 15 for 6 weeks). **p < 0.01, ****p < 0.0001. Wilcoxon matched-pairs signed-rank test.

revealed abundant new bone formation in and around the plasma-treated porous β-TCP disk (Fig. 4.7C). In both untreated and plasma-treated groups, nearly one-third of the β-TCP was absorbed for the 3 weeks between the postoperative 3 and 6 weeks (Fig. 4.7D) with similar rates. Because the initial volumes of the β-TCP disks were essentially the same (about 9.8 mm^3), the β-TCP absorption rate was unaffected by the plasma treatment.

Fig. 4.8 shows micro-CT slices and the corresponding histological sections of

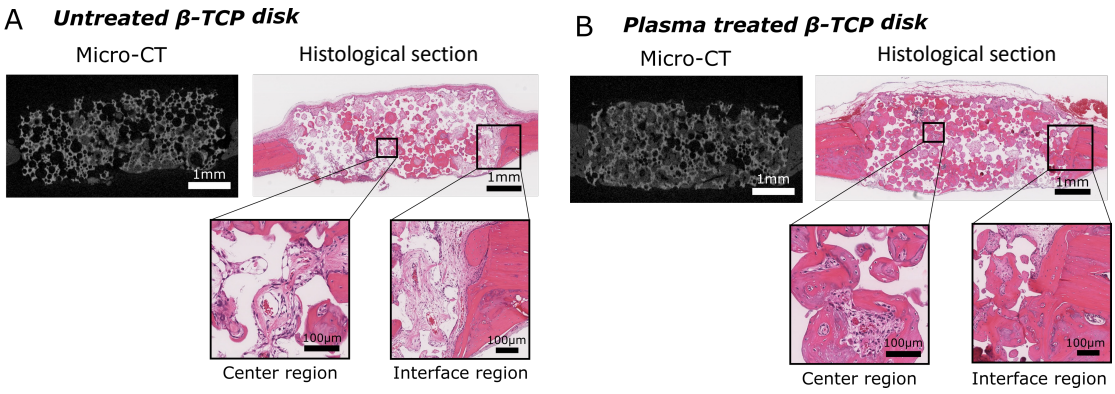

Figure 4.8: Histological sections at postoperative 6 weeks. (A) A cross-section image of an untreated porous β-TCP disk transplanted into a rat calvarial bone, reconstructed from its micro-CT scanning data (left). The white represents β-TCP, the gray represents the rat calvarial bone or newly formed bone, and the black represents soft tissues or the void of space. The corresponding histological section of the same porous β- TCP disk stained with H and E is shown on the upper right. The bright pink represents bony tissues, the pale pink represents soft tissues, the white represents the space of decalcified β-TCP or the void of space, and the nuclei of cells are stained in purple. Magnified images near the center and right interface region are also listed (bottom). (B) A cross-section image of a plasma-treated porous β-TCP disk transplanted into a rat calvarial bone, reconstructed from its micro-CT scanning data (left) and the corresponding histological section of the same porous β-TCP disk stained with H and E (upper right) and their magnified images (bottom). All images are at postoperative 6 weeks.

(A) untreated and (B) plasma-treated porous β-TCP disks transplanted into a rat calvarial bone at postoperative 6 weeks. In the micro-CT slices, the white represents β-TCP, the gray represents the rat calvarial bone or newly formed bone, and the black represents soft tissues or the void of space. In the histological sections, the bright pink represents bony tissues, the pale pink represents soft tissues, the white represents the space of decalcified β-TCP or the void of space, and the nuclei of cells are stained in purple. Magnified images near the center and right interface regions of the histological sections are also listed. More bone formation is observed in the plasma-treated porous β-TCP disk than in the untreated disk. The magnified histological images of the interface regions also indicate that the

new bone formed in the plasma-treated β-TCP disk has achieved good interface union with the host bone whereas, at the interface between the untreated porous β-TCP disk and the host rat calvarial bone, the host bone is in contact only with soft tissues and has not achieved solid interface union with new bone.

4.6 Discussion

In this study, we successfully formed amine-containing carbon polymers on β-TCP artificial bone surfaces by plasma polymerization using a gas mixture of CH_4, N_2, and He. This amine modification on β- TCP artificial bone surfaces enhanced in vitro cell adhesion and osteogenic differentiation as well as in vivo bone regeneration. The effects of amine-modified artificial bone surfaces on tissue ingrowth and enhancement of osteogenic differentiation are considered to be the main mechanisms underlying this high bone regeneration capacity. In the treatment of large bone defects with artificial bone, the successful introduction of cells and blood vessels at a substantial distance from the host bone remains challenging [156, 157]. To treat "critical size" bone defects, pre-loading of bone or vascular-forming cells or vascular transplantation inside artificial bones has been attempted [158–161]. These methods usually require long and costly pre-treatment. In the present study, we instead chose a "chemical modification" approach and formulated amine-containing plasma polymerization on the outer and inner surfaces of porous artificial bone. The implantation of such plasma-treated artificial bone in a rat calvarial defect model demonstrated early tissue (cells and vessels) ingrowth. The enhanced cell infiltration by plasma treatment is considered to contribute to

this early tissue ingrowth.

Amines, as functional groups, are hydrophilic. This is because, in an aqueous medium, amines become protonated and form positively charged functional groups $–NH_x^+$ (x = 1–3, depending on how many C atoms the center N atom is bonded with), which attract highly polarized water molecules. The present study revealed that amine modification of porous β-TCP surfaces enhanced the infiltration of cell suspension dropped on its surface. Notably, the plasma-treated β-TCP absorbed tissue fluid and rapidly became wet, in contrast to non-treated β-TCP, which remained almost completely dry during the implantation (Supplementary Fig. S3). Although the volumes of new bone formed at postoperative 3 weeks were observed to be similar between the plasma-treated and untreated porous β-TCP disks (Fig. 4.7B), the histological sections at postoperative 3 weeks revealed abundant infiltrated cells and tissue formation in the plasma-treated disks.

We demonstrated that β-TCP coated with amine-containing plasma-polymerized films enhanced in vitro osteoblastic differentiation and increased the volume of new bone inside the interconnected pores of artificial bones in vivo. Several effects provided by the amine modification must have contributed to this enhanced bone formation.

Amine modification of a surface is known to strengthen cell adhesion by enhancing integrin binding, which is required for osteoblastic differentiation [162–164]. In detail, cell adhesion is mainly mediated by the binding of cellular integrins and adhesive proteins such as fibronectin in the extra-cellular matrix. The positive charges of amines can increase the density of fibronectin and change its conforma-

tion [165]. These changes in fibronectin strengthen the cell adhesion by increasing the binding to integrins [166, 167] and trigger rapid phosphorylation of focal adhesion-associated tyrosine kinase (FAK) [168], subsequently triggering extracellular signal-regulated kinase (ERK)/mitogen-activated protein kinase (MAPK) signaling to upregulate Runt-related transcription factor 2 (Runx2), which is a master regulator of osteoblastic differentiation [169–175].

The type of change in cell morphology that we observed on the plasma-treated β-TCP, i.e., the increase of cell areas and the decrease of circularity and solidity, is known to facilitate the osteogenic differentiation of rat BMSCs [176]. This is similar to the earlier observation that human mesenchymal stem cells exhibiting a spreading, rather than maintaining round shapes, appear inclined toward an osteogenic lineage [177]. This is considered to be caused by the upregulation of Ras homolog family member A (RHOA), a transcription factor that regulates the actin cytoskeleton and increases osteogenesis [176–178]. The basicity of amines can also improve osteogenesis by increasing the interfacial pH [179]. A high pH environment around implant materials has been reported to enhance osteoblastic differentiation [179, 180].

Our study also showed that the plasma treatment enhanced the osteogenic differentiation without affecting cellular proliferation (Fig. 4.3B). In general, cellular proliferation and osteogenic differentiation do not necessarily occur simultaneously. Indeed, earlier studies also demonstrated the enhancement of osteogenic differentiation without enhanced cellular proliferation for different types of cells under different conditions [9, 47, 181]. The enhanced cell adhesion, change in cell

morphology, and possibly the increase of interfacial pH due to the presence of amine groups on β-TCP artificial bone surfaces are thus consistent with, and underlie, the high bone regeneration capacity achieved by the plasma polymerization on the artificial bones.

The major limitation of this study is, however, that we investigated the bone regeneration capacity only with a rat calvarial defect model. The calvaria has a rich blood supply and therefore offers a supportive environment for bone regeneration. A further investigation on bone regeneration under more stringent conditions, e.g., that for malunion of fractures, is desirable. Furthermore, as the size of artificial β-TCP bones designed for the rat calvarial defect model was small, we were only able to evaluate the bone volume with a high-resolution micro-CT, but unable to obtain other important bone parameters such as trabecular numbers and thicknesses or to perform biomechanical tests to evaluate mechanical strengths of the regenerated bone.

Despite such limitations, the findings of this study indicated that the rapid cell infiltration into the interconnected pores of artificial bones and the enhanced osteoblastic differentiation capability due to the presence of plasma-polymerized films on the artificial bone surfaces contributed to the early tissue ingrowth and high bone regeneration inside and around the plasma-treated artificial bones. Considering the fact that no commercial artificial bone is currently available that possesses a satisfactory osteogenic capacity, we expect these characteristics of amine-modified artificial bones to pave the way to the development of a safe and more effective treatment of large bone defects.

Chapter 5

PEEK implant functionalization with magnetron-sputtered $SrTiO_3$ for regenerative medicine

5.1 Introduction

Degenerative spine disease and low back pain have been extensively studied because of their significant impact on millions of people worldwide [182, 183]. These conditions often lead to chronic pain and loss of functions owing to intervertebral degeneration, fractures, dislocations, and deformities [184]. One treatment option for these conditions involves the use of implants to replace or support the damaged discs. Among various implant materials, polyetheretherketone (PEEK) is a preferred choice due to its natural radiolucency, magnetic resonance imaging (MRI) compatibility, and excellent mechanical properties that are comparable to those of

human cortical bone [185–187].

PEEK has replaced some conventional metal or ceramic implants for certain applications [185, 188] and is now widely used for bone implants, such as spinal cages, owing to its biocompatibility and favorable mechanical properties [189]. However, PEEK exhibits a low affinity for bone tissue and lacks osteoconductivity and osseointegration [187, 190], which can limit its effectiveness in certain applications. To address this issue, researchers have explored various strategies to enhance the osseointegration of PEEK implants [191], including its surface modification by the coating of bioactive agents [186], which has improved the efficiency of bone and soft tissue binding [192] and antibacterial properties [193].

Strontium (Sr) shares similar chemical properties with calcium (Ca) [194, 195]. Earlier studies examined the effects of non-radioactive Sr on bone through animal experiments [196–200]. The presence of Sr ions (Sr^{2+}) in biological environments is known for their dual effects of stimulating bone growth through osteoblasts and inhibiting bone resorption through osteoclasts [66]. This unique characteristic of Sr has led to its potential medical application in treating osteoporosis [198]. For example, Sr was used to improve osteoblast responses in bone implants such as bionic zirconia implants [201] and titanium (Ti) implants [202–206] and to enhance bone-to-implant contact [57].

Some of such studies used strontium titanate ($SrTiO_3$, STO) as a material that releases $Sr_2{}^+$ ions. The combination of $SrTiO_3$ and Ti was used to deposit a film on Ti implants (grade 4 Ti) by DC magnetron sputtering, which improved the bone-to-implant (BIC) interface up to 53% [202]. The magnetron sputtering

method was also used to deposit $SrTiO_3$ films on alkali-heat treated titanium, which promoted osteointegration ability in both normal and osteoporotic conditions [207]. In another study, sol-gel was applied to deposit $SrTiO_3$ mesoporous film on glass, which enhanced surface bioactivity, cell adhesion, and proliferation [208].

Some of such studies used strontium titanate ($SrTiO_3$, STO) as a material that releases $Sr_2{}^+$ ions. The combined deposition of STO and Ti was used to modify the surfaces of Ti implants by DC magnetron sputtering, which improved the bone-to-implant interface by up to 53% [202]. The magnetron sputtering method was also used to deposit STO films on alkali-heat-treated Ti, which promoted osteointegration ability in both normal and osteoporotic conditions [207]. In another study, sol-gel was applied to deposit STO mesoporous films on glass, which enhanced the surface bioactivity, cell adhesion, and proliferation [208].

Several studies have focused on enhancing the surface properties of PEEK through the incorporation of Sr-containing materials. For example, one study formed strontium-containing HA on PEEK with a molding technique to promote bone mineralization [209]. Another study used pulse electron deposition to deposit Sr doped calcium phosphate powders on the surfaces of PEEK implants to improve the wettability and mechanical properties [210]. The incorporation of both adiponectin and Sr in PEEK implants was found to enhance cellular responses for bone regeneration and osteogenic activity [211] and the incorporation of Sr-doped bioactive glass nanoparticles and polydopamine in PEEK implants was found to improve their antibacterial properties, reducing the risk of infection

after surgery [212].

In this study, we formed thin STO films on PEEK surfaces by sputtering deposition [213–219]. As discussed above, STO has been established as a material to release $Sr_2{}^+$ ions into its surrounding tissues when it is used for implants. On the other hand, sputtering deposition of STO has been widely used for various engineering applications [220, 221] and its techniques have been well established. It can be performed at or near room temperature such that PEEK implants are hardly affected when they are coated with STO films by sputtering deposition. The amount of Sr incorporated in the implants can be easily controlled by adjusting the thickness of the deposited STO film.

The goal of this study is to demonstrate that STO films can be deposited on PEEK implants by sputtering deposition and examine how Sr can be released from the deposited STO films to the surrounding environments. While the biological effects of STO-coated PEEK implants will be discussed in separate publications, we focus in this study on the physical properties of deposited STO films, including their ability to release Sr to surrounding water. The amount of Sr release is likely to increase as the deposited film thickness increases, but how about the rate? If the rate of Sr release also increases with the film thickness, how can we prolong the effectiveness of the STO-coated PEEK implants by ensuring a steady Sr release for an extended period? These are the questions we address in this study.

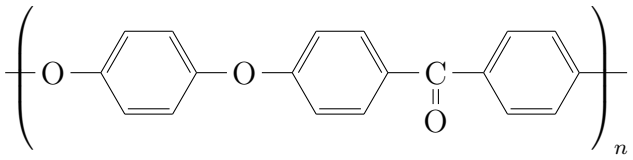

Figure 5.1: Chemical structure of PEEK

5.2 Material and methods

5.2.1 Plasma sputter deposition experiment

Disk-like PEEK samples (ϕ 12 mm × h 2 mm) and single-crystal silicon samples with (100) surfaces were placed in a magnetron sputtering system (SCV-700LRF) with an RF generator (13.56 MHz), as illustrated in Figure 5.2, for thin film deposition. Sputter deposition was carried out with an STO (Toshima Manufacturing Co., Ltd) target or a Ti target, with dimensions of a diameter of ϕ 52.1 mm and a thickness of 0.5 mm. The samples were mounted on a sample holder (anode) 60 mm away from the target. The chamber was evacuated with a turbo-molecular pump, with a base pressure of the deposition process below 5×10^{-4} Pa. The sputter deposition process was performed at a working pressure of 0.2 Pa, a power of 100 W, and an Ar gas flow rate of 2.7 sccm. All the deposition processes were performed at room temperature without heating the sample holder.

The conditions for sputter deposition are summarized in Table 5.1. The duration of STO deposition on PEEK was varied between 5, 10, and 30 min, which are denoted as STO I, STO II, and STO III, respectively. In the cases of two-layer deposition, an additional Ti layer was deposited on top of the STO layer, with thickness variations of 5, 10, 30, and 50 nm. In the case of three-layer deposition,

Table 5.1: Summary of the sputter deposition conditions used in this study. The leftmost column gives the abbreviated names for deposition conditions. The thicknesses of Ti films referred to here are those if deposited on the Si (100) surface and not meant to indicate their actual thicknesses on PEEK or STO surfaces. The Ti deposition time was the corresponding value given in Fig. 5.2

	Deposited layers			**Number of**
Deposition conditions	1st/bottom layer	2nd layer	3rd layer	**layers**
STO I	STO 5 min	-	-	1 layer
STO II	STO 10 min	-	-	1 layer
STO III	STO 30 min	-	-	1 layer
STO II/Ti 5 nm	STO 10 min	Ti 5 nm	-	2 layers
STO II/Ti 10 nm	STO 10 min	Ti 10 nm	-	2 layers
STO II/Ti 30 nm	STO 10 min	Ti 30 nm	-	2 layers
STO II/Ti 50 nm	STO 10 min	Ti 50 nm	-	2 layers
Ti 30 nm/STO II/Ti 5 nm	Ti 30 nm	STO 10 min	Ti 10 nm	3 layers

a 30 nm Ti layer was first deposited on PEEK as the bottom layer, followed by STO 10 min deposition and, finally, thin Ti deposition as the topmost layer. For multi-layer deposition (i.e., two-layer and three-layer), the top Ti layer was deposited to control the release of Sr from the STO layer when the sample is immersed in water solution, as will be discussed later.

It should be noted that the Ti film thickness referred to in Table 5.1 indicates the Ti film deposition time with which the referred Ti film thickness would be attained if the deposition took place on the Si substrate; it does not mean the actual Ti film thickness deposited on a PEEK surface. (The film thickness cannot be measured accurately on a PEEK surface due to its surface roughness.) For Ti films, whose deposition time can be very short in our study, the corresponding film thickness on the Si substrate, rather than the deposition time, is used to express the deposition conditions for simplicity.

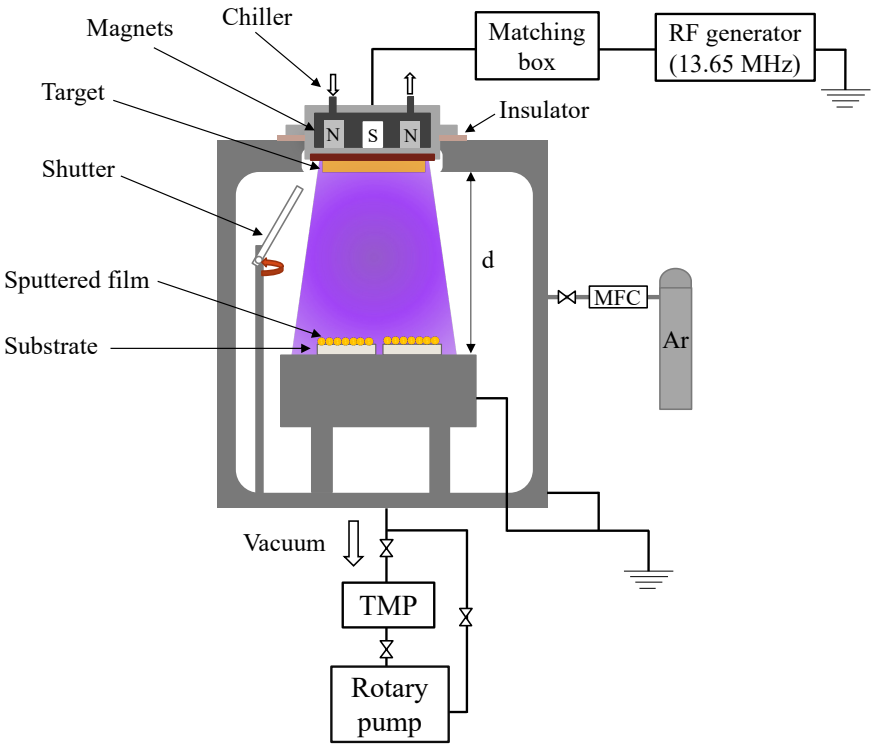

Figure 5.2: Schematic diagram of the RF magnetron sputtering system used in this study. The system was connected to a rotary pump and turbo molecular pump (TMP) for gas evacuation. The PEEK or Si samples were placed on the grounded bottom electrode. The STO or Ti target was set on the upper electrode connected to the RF power generator with a frequency of 13.65 MHz. Ar gas was ionized to generate plasma, which bombarded the target materials and sputtered off the target material. Sputtered target atoms were then deposited on the sample surface. The substrate temperature was not controlled and remained close to room temperature. The target-sample distance (d) was set at 60 mm.

5.2.2 Surface characterization

The thickness of the deposited film on a Si substrate was measured with a stylus profilometer (Dektak-XT Bruker) with a stylus tip radius of 12.5 μm and a stylus force of 3 mg. For this measurement, we covered part of the Si sample with a mask to avoid film deposition, and the step depth between the deposited and

undeposited areas was determined as the film thickness by the profilometer. The surface roughness of the pristine PEEK sample, before sputter deposition, was also measured by the stylus profilometer.

The surface morphologies of STO and Ti deposited on PEEK were examined at room temperature using field-emission scanning electron microscopy (FE-SEM; JEOL JSM-F100). To minimize the charging effect during high-resolution magnification, a 5 nm layer of osmium was coated on the STO films on the PEEK samples prior to measurement. The acceleration voltage of the FE-SEM was set to 10 kV with a working distance of 10 mm or less and at a low current. Image analyses to determine the histogram of surface pore distributions from the SEM images were performed with the ImageJ software.[222]

The surface chemical states were analyzed by X-ray photoelectron spectroscopy (XPS; JEOL JPS-9010MC) with an Al-Kα source (photon energy 1486.6 eV) and a power set to 300 W. The samples were placed on a sample holder with carbon tape and introduced to a high vacuum with an initial pressure of approximately 10^{-6} Pa. The charge neutralizer was used during analyses. Depth profiling was performed using Ar etching on the STO film deposited on PEEK with an applied voltage of 1 kV and a current of 23 mA. The peak quantifications are C 1s, O 1s, Ti 2p, Sr 3d, and Si 2p. The pass energies of the survey spectra and element core-level spectrum were 50 eV and 20 eV, respectively. Spectra were determined with Shirley's background subtraction procedure stored in CasaXPS software.

To evaluate how quickly Sr atoms are released from a deposited STO film into phosphate-buffered saline (PBS) solution, we soak an STO-coated PEEK sample

in 1 mL of PBS at room temperature for periods of 1, 3, 5, 7, and 14 days. The amount of Sr atoms accumulated in the solution for a given period was then detected by inductively coupled plasma atomic emission spectroscopy (ICP-AES; Shimadzu ICPS-8100).

5.3 Results and discussions

5.3.1 Structure analysis of film deposition on PEEK

Figure 5.3 shows the thicknesses of Ti and STO films deposited on (100) Si surfaces as functions of the deposition time. Error bars indicate the standard deviation of 20 measured thicknesses at different locations on the same sample. It is seen that the deposition rates were 4.9 ± 0.1 nm/min for STO and 9.7 ± 0.3 nm/min for Ti.

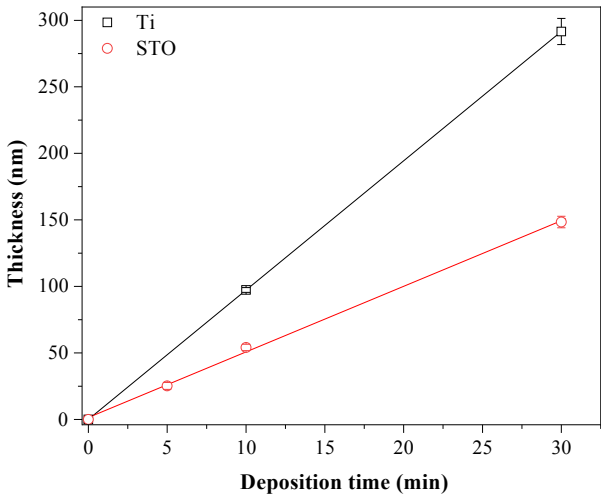

Figure 5.3: The thicknesses of Ti and STO films deposited on Si (100) surfaces as functions of the deposition time. In most cases, the error bars are smaller than the sizes of symbols.

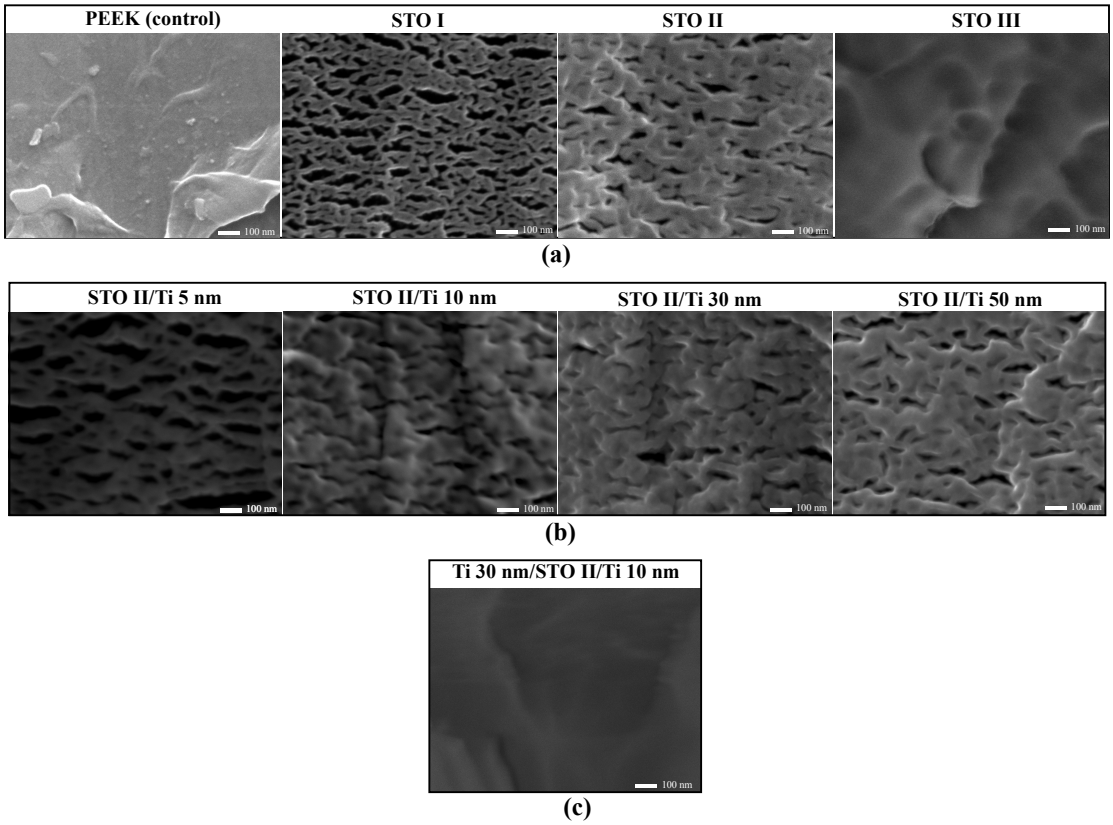

Figure 5.4: Surface morphologies at high magnification (100,000 ×) of (a) PEEK (no deposition) and STO films deposited directly on PEEK with deposition periods of 5, 10, and 30 min, (b) STO-Ti two-layer films deposited on PEEK with different Ti film thicknesses, and (c) Ti-STO-Ti three-layer film deposited on PEEK, according to the deposition conditions of Table 5.1

Surface morphologies of a pristine PEEK surface and deposited films are shown in Fig. 5.4 with a magnification of 100,000× as images taken by FE-SEM. It is seen that the pristine PEEK surface before sputter deposition is rough with a roughness of 0.9 μm measured by stylus profiling. It is also seen in Fig. 5.4(a) that the STO film growth is not uniform over the PEEK substrate when the film is relatively thin. The formation of elongated holes is observed in an STO single-layer deposition on PEEK for 5 and 10 min. After 30 min. deposition, such a hole

was no longer observed.

Ti films were deposited on STO II films (i.e., STO with 10 min. deposition) with different deposition periods and their surface morphologies are shown in (b). It seems the Ti film hardly filled in the holes of the underlying STO film; some holes are still observed even after 50 nm Ti deposition.

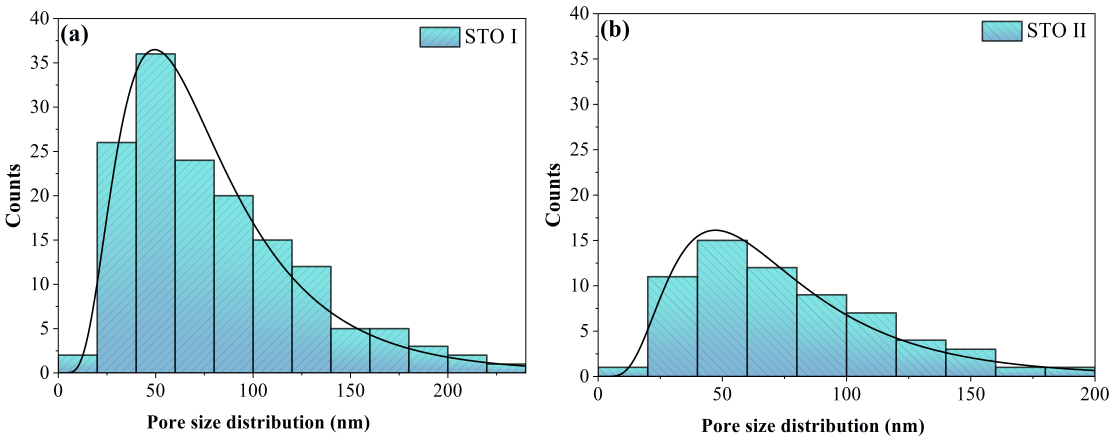

Figure 5.5: Pore size distribution histograms of STO films deposited directly on PEEK for (a) 5 min and (b) 10 min.

To avoid the formation of irregular holes of STO film on PEEK, we deposited a Ti layer directly on PEEK before an STO film and a subsequent thin Ti film were deposited. As seen in Fig. 5.4 (c), the three-layer film exhibited no sign of hole formation on the surface. It suggests that the direct deposition of a sufficiently thick Ti layer on PEEK allows the relatively uniform formation of an STO film in the subsequent sputter deposition process.

The pore-size distributions of STO I and STO II films of Fig. 5.4 (a) are given in Fig. 5.5 based on image processing of the SEM photographs. Because typical holes are elongated and may be approximated as ellipses, Fig. 5.4 plots the distribution

of the length of the major (i.e., longer) axes of such holes obtained from images shown in Fig. 5.4 (a). It is seen that, as the thickness of the STO film increases, the number of elongated holes decreases without much change in the size of the major axes. This indicates that the elongated holes become narrower as the deposition proceeds.

5.3.2 Chemical compositions of deposited films

The XPS measurement of the PEEK surface used in our study confirmed that the density ratio of carbon (C) to oxygen (O) on the PEEK surface was 6.39, which is close to that of stoichiometric PEEK of 6.33. The surface atomic concentration ratios of the deposited films obtained from XPS are summarised in Fig. 5.6, which lists the relative concentrations of Sr, Ti, and O only. The concentration of C was ignored because it can result from surface contamination by ambient air after the deposition. It is seen that the deposited STO film (STO II) has relative concentrations close to Sr:Ti:O = 1:1:3, i.e., the stoichiometric ratio of STO. As the thickness of the top Ti layer increases from 5 nm to 30 nm, the Sr signal is seen to decrease. For the three-layer (Ti 30 nm/STO II/Ti 10 nm), the Sr and O signals are lower than those for the corresponding two-layer (STO II/Ti 10 nm) film. This is likely because there are many holes in the STO film deposited directly on PEEK and a thin Ti layer cannot cover the STO film conformally and partially exposes the underlying STO film. The top Ti layer is also partially oxidized when the sample is exposed to ambient air for the *ex situ* XPS measurement or possibly during sputter deposition due to impurities in the processing chamber.

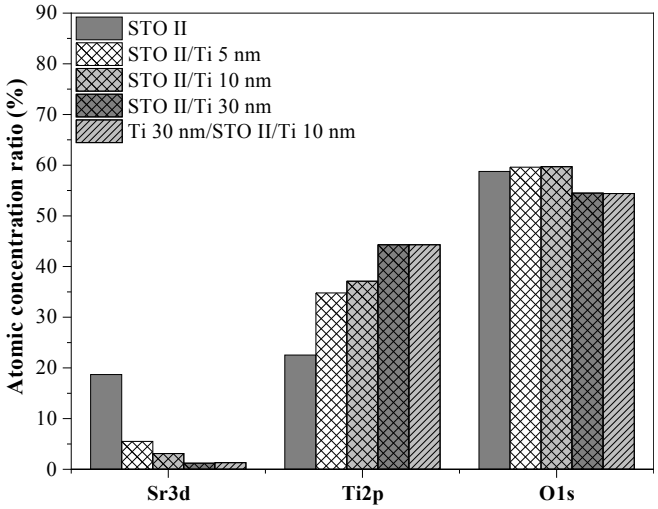

Figure 5.6: Relative concentrations of Sr, Ti, and O atoms, obtained from XPS, for single and multilayer deposition of STO II (10 min) and Ti on PEEK.

The XPS depth profiling results of C, O, Ti, and Sr relative concentrations for a single-layer STO film (STO III) deposited on Si as well as two-layer (STO II/Ti 10 nm) and three-layer (Ti 30 nm/STO II/Ti 10 nm) films deposited on PEEK are presented in Fig. 5.7. The background colors highlight the locations where some significant changes in atomic concentrations occur as the Ar ion (Ar^+) etching time increases and, therefore, they more or less mark the locations of different materials.

In each case, the C concentration on the top surface (where the Ar^+ ion etching time is 0) simply reflects carbon contamination of the surface. It should be noted that 1 keV Ar^+ ions used for depth profiling can cause significant mixing of surface atoms and preferential removal of specific atomic species as the etching proceeds. Therefore one cannot estimate the exact relative atomic concentrations of the deposited films from Fig. 5.7. For example, in (a), where a single STO film deposited on Si is examined, the relative concentrations of Sr, Ti, and O seem

close to Sr: Ti: O = 1:2:3 except for the top surface. Because the relative atomic concentrations of any surfaces of STO deposited in this study are always observed to be close to Sr: Ti: O = 1:1:3, the true relative atomic concentrations of STO should be around Sr: Ti: O = 1:1:3 throughout the deposited STO film, rather than what is seen in Fig. 5.7.

Although the STO deposition time is the same (10 min for STO II) for both (b) and (c), the Ar^+ etching time required to remove the STO film is significantly shorter in (b) than in (c). It indicates that the STO film of (b) is either thinner or easier to etch due to the presence of holes seen in Fig. 5.4 (b), or both, than the STO film of (c). Earlier studies [223–227] have reported that a PEEK surface has lower surface energy or weaker adhesion strength and is more hydrophobic than a Ti surface, which may cause STO less likely to be formed on a PEEK surface than on a Ti surface. As seen in the case of three-layer film, the presence of the bottom Ti film directly deposited on PEEK allowed the deposition of more STO for the same deposition time in the subsequent STO deposition process.

5.3.3 Control of Sr release to PBS

As discussed earlier, the thin Ti layer placed on the STO film is expected to slow down the release of Sr when the STO-coated artificial bone is implanted *in vivo*. To examine how quickly Sr is released from deposited STO films into its environment, we placed STO-coated PEEK samples in PBS solution. Assuming that Sr atoms exist as Sr_2^+ ions in aqueous solution, we measured the released Sr^{2+} ions by ICP-AES. Figure 5.8 summarizes the measurement method.

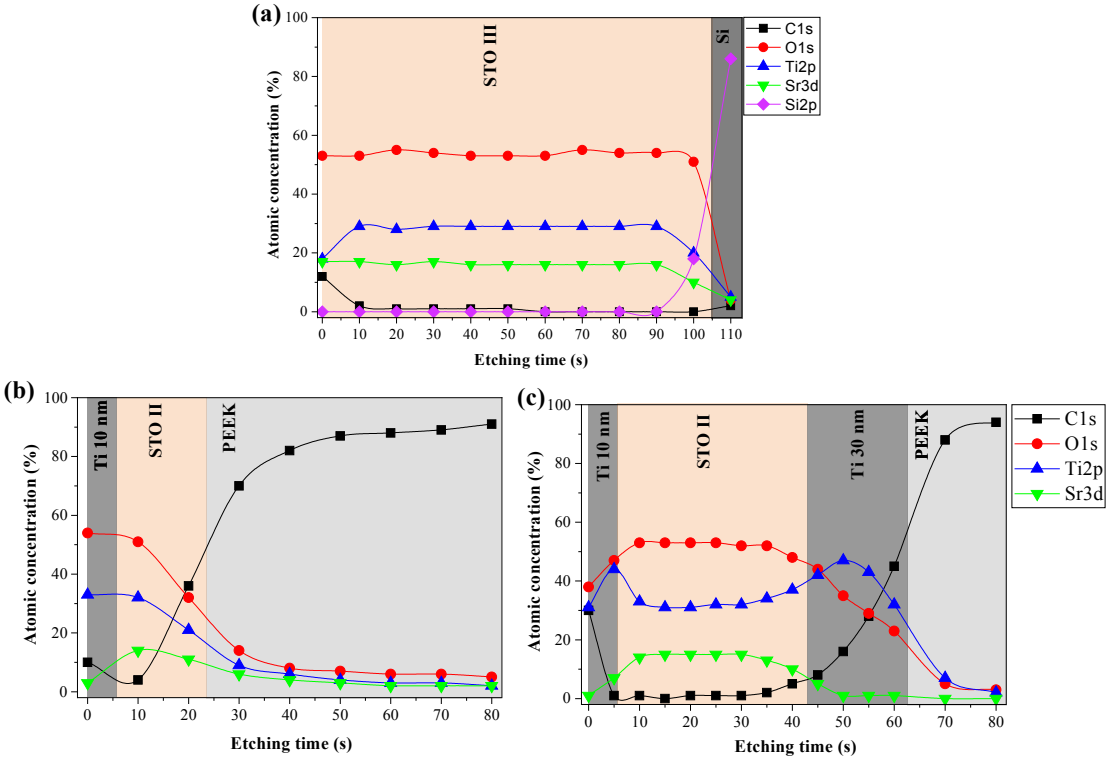

Figure 5.7: Relative concentrations of C, O, Sr, and Ti obtained from XPS depth profiling with a 1 keV Ar^+ ion beam for (a) one-layer (STO III) deposition on Si, (b) two-layer (STO II/Ti 10 nm) deposition on PEEK, and (c) three-layer (Ti 30nm/STO II/Ti 10 nm) deposition on PEEK, under the conditions listed in Table 5.1

Figure 5.9 shows the accumulated amounts of Sr_2^+ ions released from various STO films deposited on PEEK as functions of the immersion time in PBS. The results for the single-layer STO films are shown in (a), where the thicker STO film releases more Sr_2^+ but the release rate is also higher, reaching its near maximum concentration within 2-4 days, regardless of the thickness. In (b), the results of multilayer samples with the STO films deposited for 10 min are compared with that of a single-layer sample of STO II. It is seen that, in the case of two-layer (STO II/Ti) samples, the rates of Sr^{2+} release depend weakly on the thickness of the top Ti film. This is probably because, as discussed earlier, the top Ti film

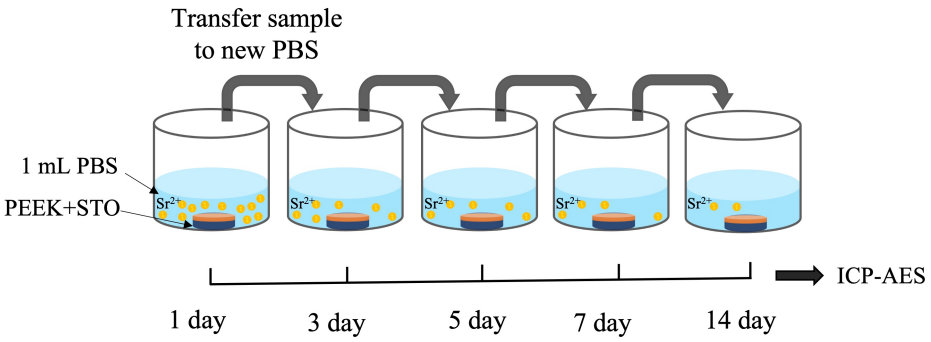

Figure 5.8: Schematic diagram of the Sr measurement in PBS. The STO-coated PEEK sample (denoted as PEEK+STO in this figure) was immersed in a 1mL PBS for one day and then moved to a new 1 mL PBS. The concentration of Sr in the former solution was then measured with ICP-AES. This process was repeated with various immersion periods and the Sr content in each PBS solution was measured.

could not cover the rough STO surface entirely and some parts of the STO surface might be exposed directly to the PBS solution.

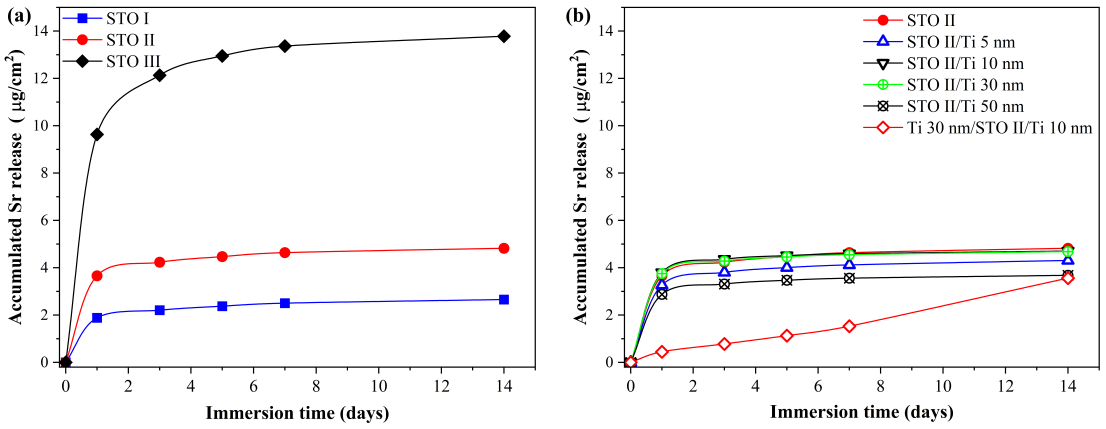

Figure 5.9: Accumulated Sr released in PBS for 1, 3, 5, 7, and 14 days from (a) the single-layer STO films deposited on PEEK for 5, 10, and 30 min and (b) the single-, two-, and three-layer films with STO deposition for 10 min on PEEK.

In the case of the three-layer structure, however, the top Ti film functioned as a barrier for Sr diffusion to the solution and a steady release of Sr^{2+} ions over 10 days was achieved. Although the data is not shown here, the ICP-AES also

confirmed that no Ti was dissolved into PBS during the same experiments.

To confirm that the Sr content of the STO film was reduced after it was immersed in PBS solution for an extended period, we observed the ratio of atomic concentrations of Sr to Ti on the surfaces of single-layer STO films deposited on PEEK, as shown in Fig. 5.10. It is seen that the amount of Sr decreased compared with that of Ti after the sample was immersed in PBS solution for 14 days.

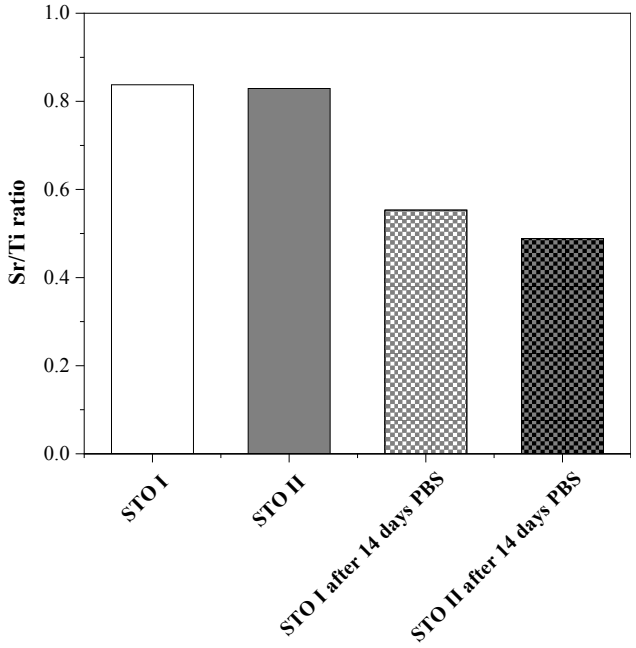

Figure 5.10: Concentration ratios of Sr to Ti of STO I and II surfaces, obtained from XPS, before and after being immersed in PBS solution for 14 days.

5.4 Conclusion

We have demonstrated STO deposition on PEEK surfaces by magnetron sputtering and examined the physical properties of the deposited films. The biological effects of STO-coated PEEK artificial bone will be discussed in separate publi-

cations. The target material used for the sputtering process was stoichiometric $SrTiO_3$ and the sputter-deposited films in our study also exhibited a stoichiometry close to that of the target. The sputtering deposition of STO forms a smooth and uniform film on the Si (100) surface. However, if a relatively thin STO film is deposited directly on PEEK by the same method, the deposited film exhibits rough surfaces with many holes. It suggests there is some incubation time for STO to grow on PEEK and possibly island structures are formed in the early deposition stage.

Sr is known to be readily dissolved from STO if the STO is exposed to water solution, so there is a concern that STO-coated artificial bone may run out of Sr quickly after it is implanted *in vivo*. The presence of Sr is known to have positive effects on bone regeneration, so, in some implant applications, the steady release of Sr from Sr-coated artificial bone for an extended period may be preferred.

To retard the Sr release from STO to the surrounding water, a thin Ti film was deposited on the STO surface. However, if the STO film is directly deposited on PEEK, it is found that the top Ti film hardly affects its Sr release rate. This is probably because the STO films directly deposited on PEEK have rough surfaces with many holes and, therefore, the thin top Ti film could not cover the STO surfaces completely.

On the other hand, we have demonstrated that the three-layer structure exhibits a steady release of Sr. By depositing a Ti film with a reasonable thickness directly on PEEK first, we were able to deposit a relatively thick STO film on the Ti film with the same deposition time as that of the STO film deposited directly

on a similar PEEK surface. This thicker STO film with a smoother surface allowed a better coverage of the STO surface by a thin Ti film deposited on it. When the three-layer coated PEEK sample was immersed in PBS solution, the diffusion of Sr through the thin top Ti film allowed the controlled steady release of Sr from the underlying STO film to the surrounding solution.

Chapter 6

General conclusion

In this research, low-pressure plasma e.g. PECVD or bipolar pulsed plasma and plasma sputtering has been done to modify the surface of artificial bone for orthopedic application. The classical MD simulation also was used to provide insight into the amine PP growth and formation of amine groups under PECVD.

In Chapter 2, the surface modification of porous hydroxyapatite (HA) as an artificial bone was performed with amine plasma polymerization by bipolar pulsed discharge. The stability of nitrogen-containing and primary amine embedded in the deposited polymer film on porous HA by bipolar pulsed discharge with low-pressure pulsed was investigated. The porous HA surface was effectively covered by the primary amine, as confirmed by 4-trifluoromethyl benzaldehyde (TFBA) derivatization. The experimental results showed that the high ratio of primary amine to the number of carbon $[NH_2]/[C]$ and nitrogen $[NH_2]/[N]$ in a plasma-deposited hydrocarbon film was typically about 0.03 and 0.20 respectively. The

stability of nitrogen-containing was examined on the porous HA surface, and it was confirmed that nitrogen also existed inside the HA pores through cross-section analysis of porous HA. The bipolar pulsed discharge was able to carry reactive species deeply inside the pores and functionalize the inner pores. The stability of plasma polymer (PP)-coated HA was investigated. It demonstrates the effectiveness and stability of amine plasma polymerization for surface modification of porous HA, which could have important implications for the development of improved artificial bones.

Chapter 3 explored the use of molecular dynamics (MD) simulations to analyze the amine formation process in carbon-based polymer films that were deposited using plasma-enhanced chemical vapor deposition (PECVD) with methane (CH_4) and nitrogen (N_2) gases. The surface of the deposited film and the incident precursors were analyzed, and it was assumed that only amino radicals (NH_2) supplied nitrogen species, so that the maximum amount of primary amine ($-NH_2$) could be present in the deposited film. Carbon was supplied to the reaction as either CH_2 or CH_3 radicals, or CH_2^+ or CH_3^+ ions with an ion kinetic energy up to 100 eV, which is typical in PECVD experiments of this type. The study shows that an increase in the concentration of NH_2 radicals in the gas phase during PECVD has a minimal impact on the primary-amine content in the resulting films. It appears that the primary amine content is not highly influenced by the plasma conditions as long as there is a sufficient amount of nitrogen and hydrogen during plasma polymerization.

Chapter 4 describes the process of modifying the surface of calcium phosphate

artificial bone using a bipolar pulsed plasma in the context of plasma amine polymerization. The results demonstrate that plasma-treated β-TCP displays a noticeably increased hydrophilicity, thereby promoting the extensive infiltration of cells into the interconnected porous β-TCP, facilitating tissue regeneration. The adhesion and osteogenic differentiation of cells on the plasma-treated artificial bone surfaces were also improved. In a rat calvarial defect model, the plasma treatment demonstrated high bone regeneration potential. The outcomes imply that the modification of artificial bone through plasma technology with amine is likely to demonstrate high osteogenic ability and thus represents a promising approach for overcoming current clinical restrictions related to the utilization of artificial bone.

In Chapter 5, a high-performance polymer called PEEK was used to create artificial spinal cage materials. In this study, the $SrTiO_3$ thin film was deposited on PEEK surfaces using RF magnetron sputtering. The film properties and release of $Sr_2{}^+$ ions into a phosphate-buffered saline (PBS) solution were examined. The results showed that, in the early stages of the deposition process, STO on a PEEK surface had irregular structures with many holes. As the film thickness increased, the amount of Sr stored in the STO film also increased, but the release rate of $Sr_2{}^+$ ions from the STO film also increased, limiting the duration of effectiveness of STO-coated PEEK films. However, a multilayer STO and Ti film allowed for a steady and slower release of $Sr_2{}^+$ ions into the surrounding PBS.

The research has comprehensively examined surface modification for orthopedic applications, including the application of low-pressure plasma techniques,

molecular dynamics simulations, and advanced materials. In particular, this study has investigated the use of amine plasma polymerization through bipolar pulsed discharge and plasma-enhanced chemical vapor deposition to effectively functionalize artificial bone materials, such as porous calcium phosphate (HA and β-TCP), with primary amine groups. The results demonstrate the effectiveness of amine plasma polymerization in providing stability and enhanced functionality for artificial bones. Furthermore, molecular dynamics simulations have provided insights into the amine formation process in plasma-deposited films and the factors that influence primary amine content. The artificial bone was successfully modified with $SrTiO_3$ on the surface of PEEK using plasma sputtering. the deposition of Sr-containing also could controlled on the PEEK implant with multilayer deposition. For the current state, our research still focus on amine plasma polymerization for calcium phospate and $SrTiO_3$ deposition for PEEK. Further investigations are possible to expand the modification of biomaterial surfaces using several approaches, either by changing the deposition methods or using different bone implants, and finding the potential of these innovative approaches, which pave the way for the development of next-generation orthopedic materials and implants.

Appendix A

MD simulation for plasma polymerization - Supporting Information

A.1 Interatomic Potential Functions

The mechanisms of amine plasma polymerization during plasma processes in PECVD can be studied through molecular dynamics (MD) simulation. The interatomic potential models used in this study (i.e., C/N/H system) are the same as those used in previous research [88–90, 136–138, 154], which are based on Stillinger-Weber potentials that consider multi-body interactions for various atomic species.[139–142] that represent multi-body interactions for covalent bonds among various atomic species. For the purpose of simplicity, we employ the same interatomic potential functions for both ions and charge-neutral atoms of the same

species. The energetic ions impacting a surface are considered to be energetic neutral atoms of a similar term. The total potential energy Φ of the system as

$$\Phi = \sum_i \sum_{i<j} \left[V_{ij}(r_{ij}, \sigma_{ij}) + \sum_{j<k} W_{ijk}(r_i, r_j, r_k) + V_{vdw}(r_{ij}) \right] \tag{A.1}$$

where V_{ij}, W_{ijk}, V_{vdw} are the two-body, three-body, and van der Waals potential.

The two-body V_{ij} is the total interaction of repulsive V_R and attractive V_A potential function between the i^{th} and j^{th} atoms with interatomic distance r_{ij} as given by

$$V_{ij}(r_{ij}, \sigma_{ij}) = V_{ij}^R(r_{ij}, \sigma_{ij}) + V_{ij}^A(r_{ij}, \sigma_{ij}). \tag{A.2}$$

In this system, the function of the two-body function depends on the bond order σ_{ij}. The value of the bond between i^{th} and j^{th} is determined by the presence of other atoms surrounding them. Our model assumes that these functions are dependent on both the interatomic distance r_{ij} and the bond order σ_{ij}.

$$V_{ij}(r_{ij}, \sigma_{ij}) = \frac{A_{ij}^\sigma}{r^{p_{ij}^\sigma}} \exp\left(\frac{D_{ij}^\sigma}{r - r_{ij}^\sigma}\right) - \frac{B_{ij}^\sigma}{r^{q_{ij}^\sigma}} \exp\left(\frac{C_{ij}^\sigma}{r - r_{ij}^\sigma}\right) \tag{A.3}$$

The value of the numerical parameters A_{ij}^σ, B_{ij}^σ, C_{ij}^σ, D_{ij}^σ, p_{ij}^σ, q_{ij}^σ, and r_{ij}^σ are determined by the i^{th} and j^{th} atoms and the bond order of the ij bond. The

interatomic cutoff length of this potential function is given by r_{ij}^{σ} where V_{ij} = zero if $r \geq r_{ij}^{\sigma}$.

The three-body interaction, denoted as W_{ijk}, describes the angular dependencies of the i^{th}, j^{th}, and k^{th} atoms given by

$$\begin{aligned} W_{ijk} =& h_{jik}(r_{ij}, r_{ik}, \theta_{jik}, \sigma_{ij}, \sigma_{jk}) + h_{ijk}(r_{ji}, r_{jk}, \theta_{ijk}, \sigma_{ji}, \sigma_{jk}) \\ &+ h_{ikj}(r_{ki}, r_{kj}, \theta_{ikj}, \sigma_{ki}, \sigma_{kj}). \end{aligned} \tag{A.4}$$

Here i, j, and k represent the identification number of each atom and their positions are denoted by r_{ij}. The bond order σ_{ij} is defined as the bond between i^{th} and j^{th} atoms. σ_{ij} is 1, 2, and 3 denoted as single, double, and triple bonds respectively. The angle θ_{ijk} is the bond angle at the j^{th} atom between the ji bond and the jk bond.

The H, C, and N atoms in this system have different two-body potentials, i.e., V_{HH}, V_{HC}, V_{HN}, V_{CC}, V_{CN}, and V_{NN}. The two-body potential functions for the single, double, and triple bonds used in this study, for example, the bond of V_{CC} i.e., $V_{CC}(r,\, 1)$, $V_{CC}(r,\, 2)$, and $V_{CC}(r,\, 3)$. We used potential function for general bond order σ ($1 \leq \sigma \leq 3$) for carbon-carbon bond as follows;

$$V_{CC}(r, \sigma) = \begin{cases} (2-\sigma)V_{CC}(r,1) + (\sigma-1)V_{CC}(r,2) & \text{if } 1 \leq \sigma \leq 2 \\ (3-\sigma)V_{CC}(r,2) + (\sigma-2)V_{CC}(r,3) & \text{if } 2 \leq \sigma \leq 3 \end{cases} \tag{A.5}$$

The potential function for carbon-nitrogen (V_{CN})(r_{ij}, σ) and nitrogen-nitrogen

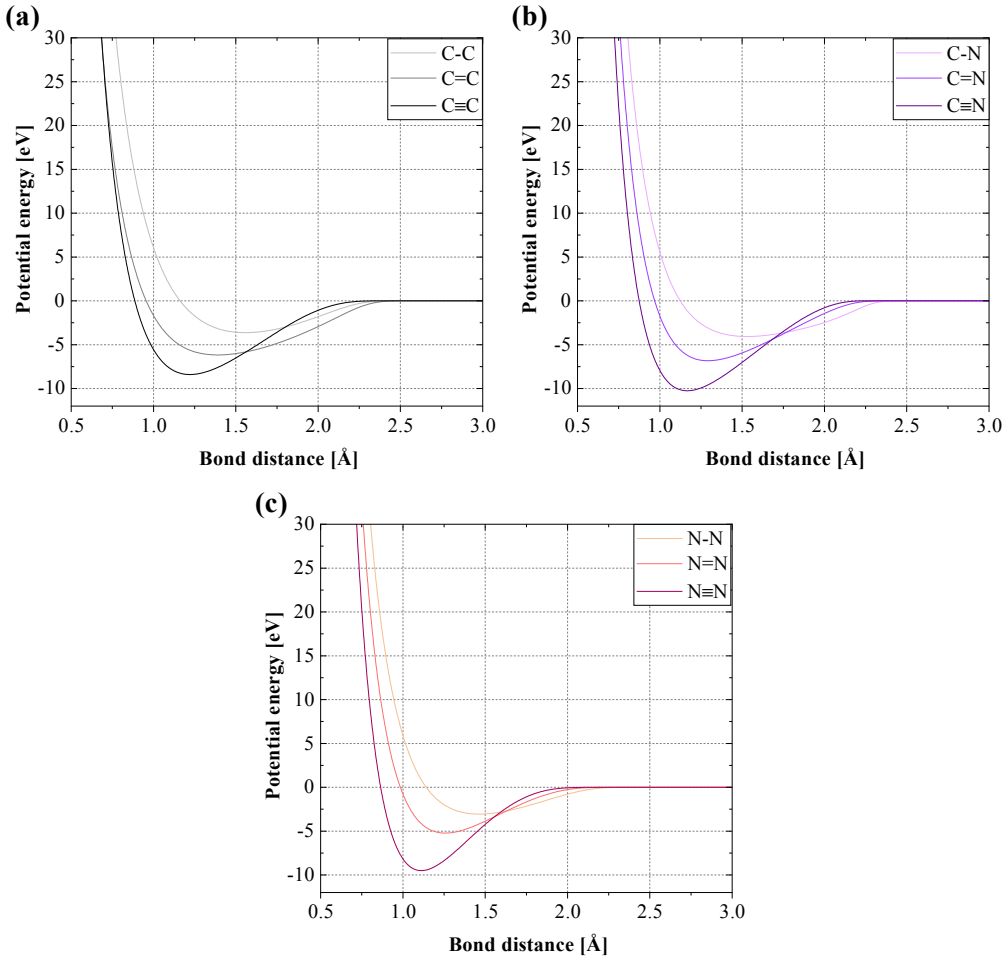

Figure A.1: Two-body interatomic potential functions between (a) two carbon atoms, (b) carbon and nitrogen atoms, and (c) two nitrogen atoms.

$(V_{NN})(r_{ij}, \sigma)$ are determined in similar manner. The bond order is the same as that given in [88, 228]. Some examples of the two-body interatomic potential functions used in this study are shown in Fig. A.1.

A.2 Bond energy and sticking probabilities used in molecular dynamic simulations

The chemical bond energy between two atoms is typically close to the (absolute value of the) minimum energy of the corresponding two-body interatomic potential, which is listed in Table A.1 under "our simulation" for each bond and compared with the bond energies from other literature.

Table A.1: Comparison of the bond energies of our simulation with the values from other literature. The value of bond energy of our simulation is the minimum energy of the corresponding two-body potential.

	Bond energy (eV)			
Bond	Our simulation	Ref.229	Ref.230	Ref.231
H−H	5.00	4.52	4.48	4.48
C−H	4.73	4.28	4.28	4.26
N−H	4.90	4.05	4.05	4.00
C−C	3.68	3.60	3.60	3.58
C=C	6.17	6.37	6.36	6.24
C≡C	8.40	8.41	8.70	8.66
C−N	4.09	3.02	3.16	3.16
C=N	6.83	6.37	6.37	6.37
C≡N	10.31	9.24	9.23	9.19
N−N	3.11	1.67	1.66	1.73 or 2.56
N=N	5.24	4.34	4.33	4.33
N≡N	9.51	9.80	9.75	9.76

It is seen that the N-N single-bond energy is especially overestimated in our simulation model. This is partially because the N-N single-bond energy tends to vary significantly among different molecules. However, in the present study, N-N single bonds are hardly observed, as seen in Figs. 8 and 9 of the main text. Therefore, it is likely that the inaccuracy of the N-N single-bond energy in our

Table A.2: The sticking probability of CH_2 and CH_3 ion on C surface.

Incident energy (eV)	Sticking probability (%)			
	CH_2		CH_3	
	C atoms	H atoms	C atoms	H atoms
0.2	94.0	92.8	89.0	82.3
10	90.4	86.5	80.4	73.9
50	57.6	78.8	56.2	68.6
100	63.2	83.0	64.0	73.5

model hardly affects the conclusion of this study. Further improvement of the interatomic potential functions is a subject of future study.

The sticking probability of CH_2 and CH_3 were examined in 5 different cases as a function of the incident energy on a clean C substrate as shown in Fig. 1 in the main text. In our study, the sticking probability is defined as the ratio of the total number of remaining CH_2 or CH_3 on the C substrate to the total number of injected ions. The CH_2 radicals or ions (in our model, both have the same interatomic potential functions, as discussed in the manuscript) are more likely to stick to the surface than CH_3 for the same incident energy. The results are summarized in Table A.2.

Appendix B

MD simulation of amine formation in PECVD - Supporting Information

B.1 MD simulation results for amine PPs

In this appendix, the deposition in MD simulation for conditions II, III, IV, and V in Chapter 3 is presented in Fig. B.1, B.2, B.3, B.4, respectively. The depth profiles of H, C, and N atomic concentrations in the deposited films, obtained from MD simulations are shown in Fig. B.5. The depth profiles and relative concentrations of all bonds and N−H bonds densities are shown in Fig. B.7 and Figure B.8. The ratios of desorbed species are given in Fig. B.9.

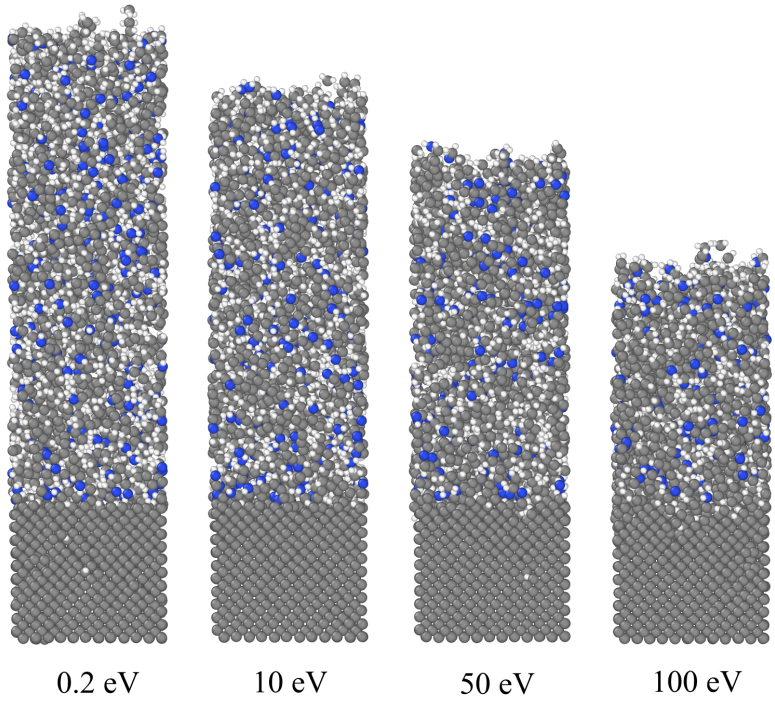

Figure B.1: MD simulation results with atomic models at different ion incident energies from 0.2 eV to 100 eV for Case II, i.e., the incident radicals are NH_2 and CH_2 and ions are CH_3^+. The gray, blue, and white spheres represent C, N, and H atoms, respectively.

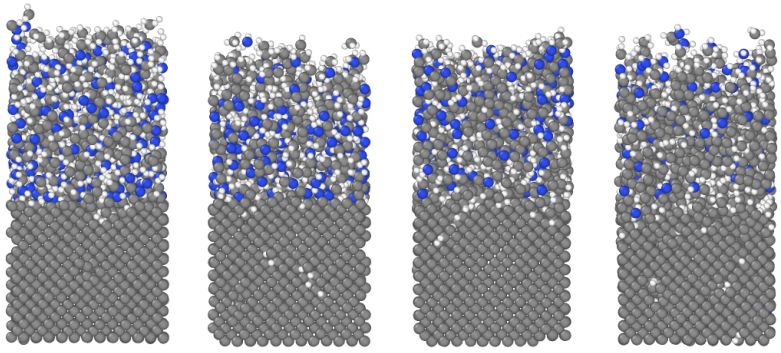

Figure B.2: MD simulation results with atomic models at different ion incident energies from 0.2 eV to 100 eV for Case III, i.e., the incident radicals are NH_2 and CH_3 and ions are CH_3^+. The gray, blue, and white spheres represent C, N, and H atoms, respectively.

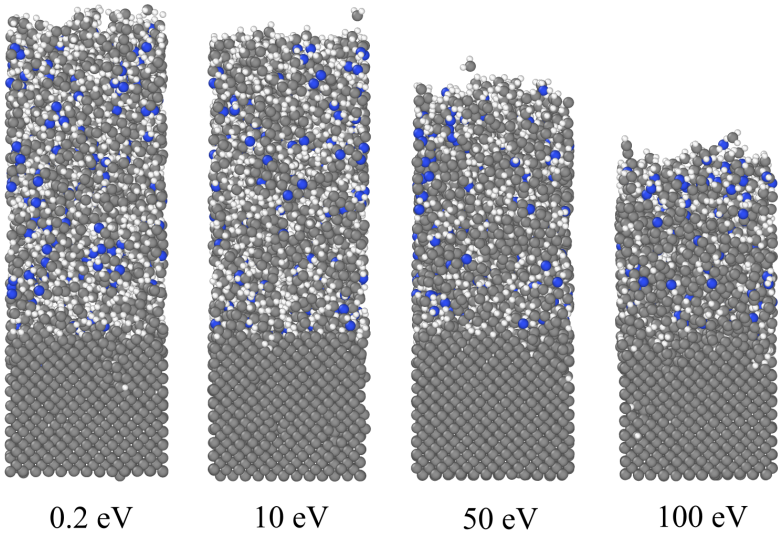

Figure B.3: MD simulation results with atomic models at different ion incident energies from 0.2 eV to 100 eV for Case IV, i.e., the incident radicals are NH_2, CH_2, and H and ions are CH_2^+. The gray, blue, and white spheres represent C, N, and H atoms, respectively.

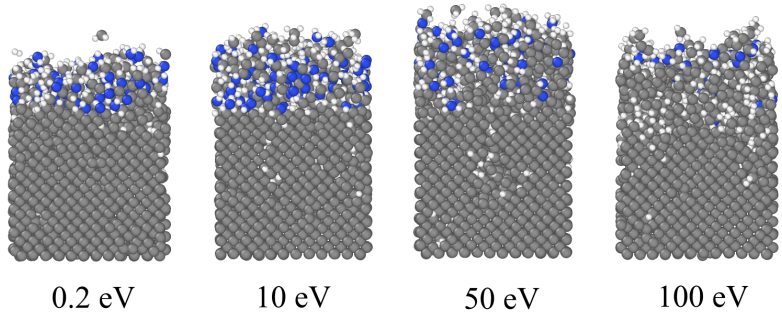

Figure B.4: MD simulation results with atomic models at different ion incident energies from 0.2 eV to 100 eV for Case V, i.e., the incident radicals are NH_2, CH_3, and H and ions are CH_3^+. The gray, blue, and white spheres represent C, N, and H atoms, respectively.

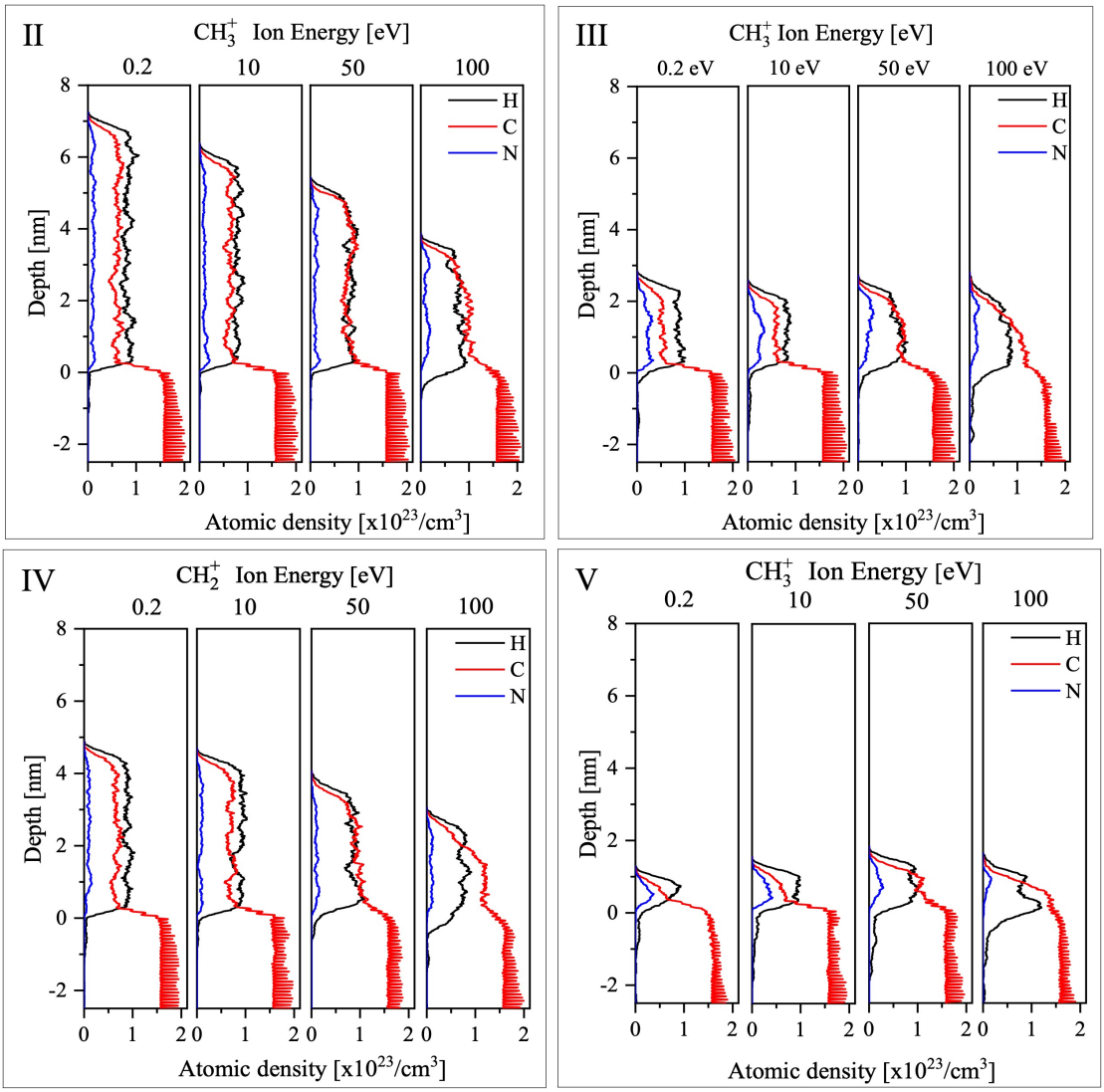

Figure B.5: Depth profiles of atomic concentrations at different ion incident energies from 0.2 eV to 100 eV for Case II, III, IV, and V. The ion dose is 2.18×10^{16} /cm^2. The atomic densities of H, C, and N atoms are represented by black, red, and blue curves, respectively

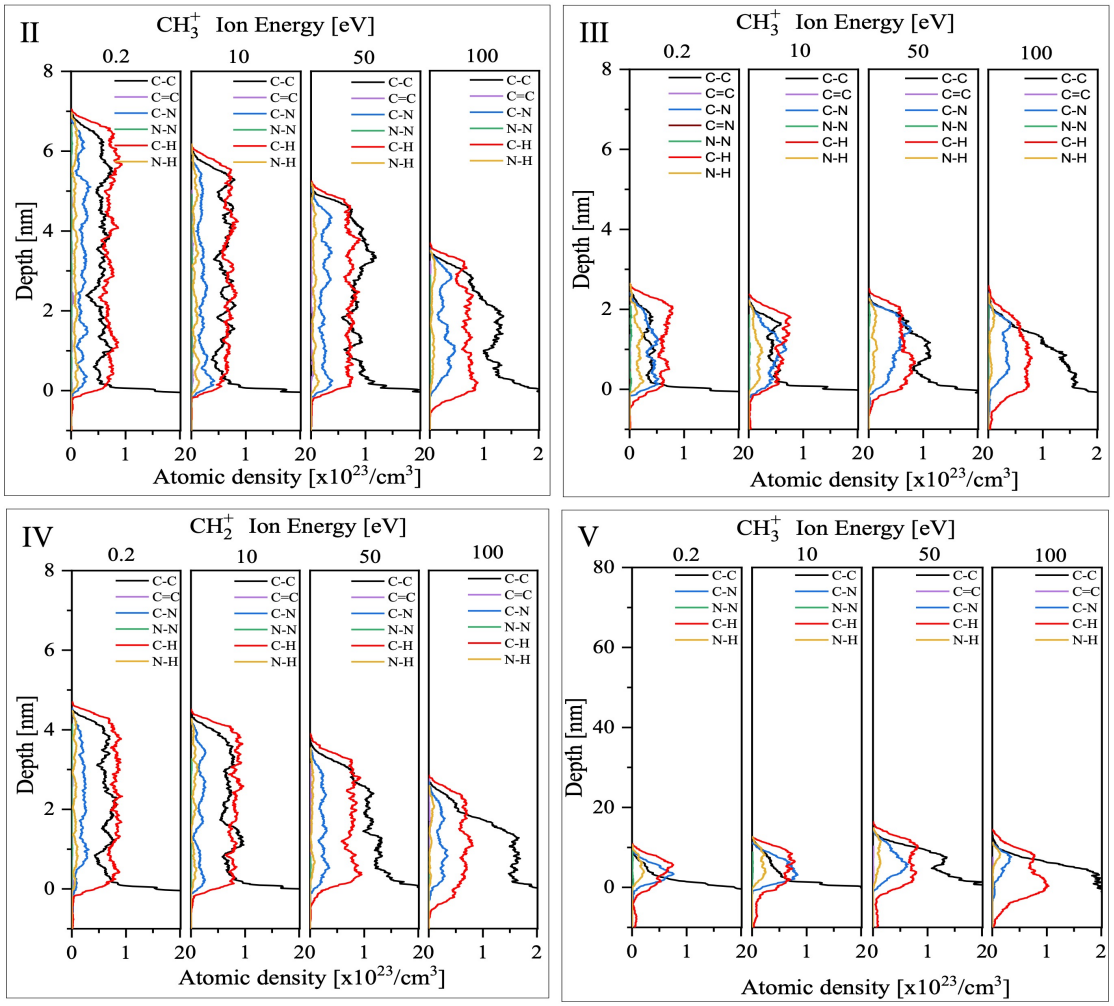

Figure B.6: Depth profiles of atomic concentrations at different ion incident energies from 0.2 eV to 100 eV for Case II, III, IV, and V.

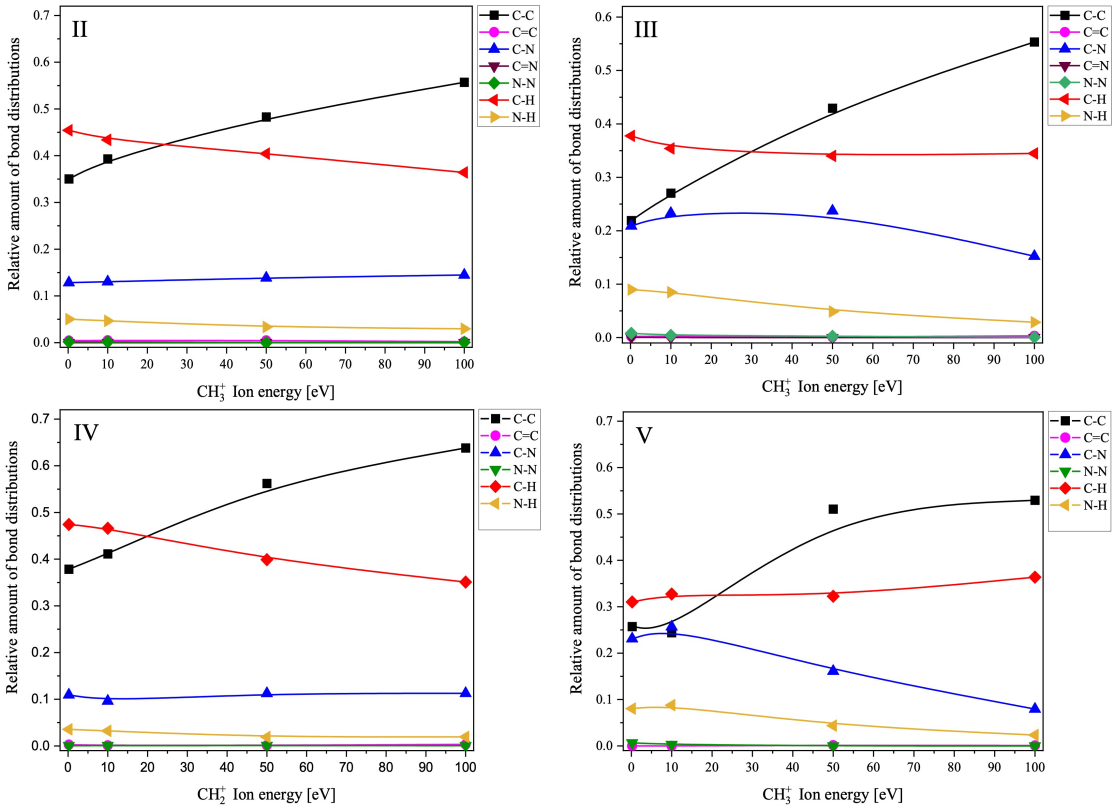

Figure B.7: Relative concentrations of the bonds listed in B.6 averaged over the deposited films at different ion incident energies from 0.2 eV to 100 eV for Case II, III, IV, and V.

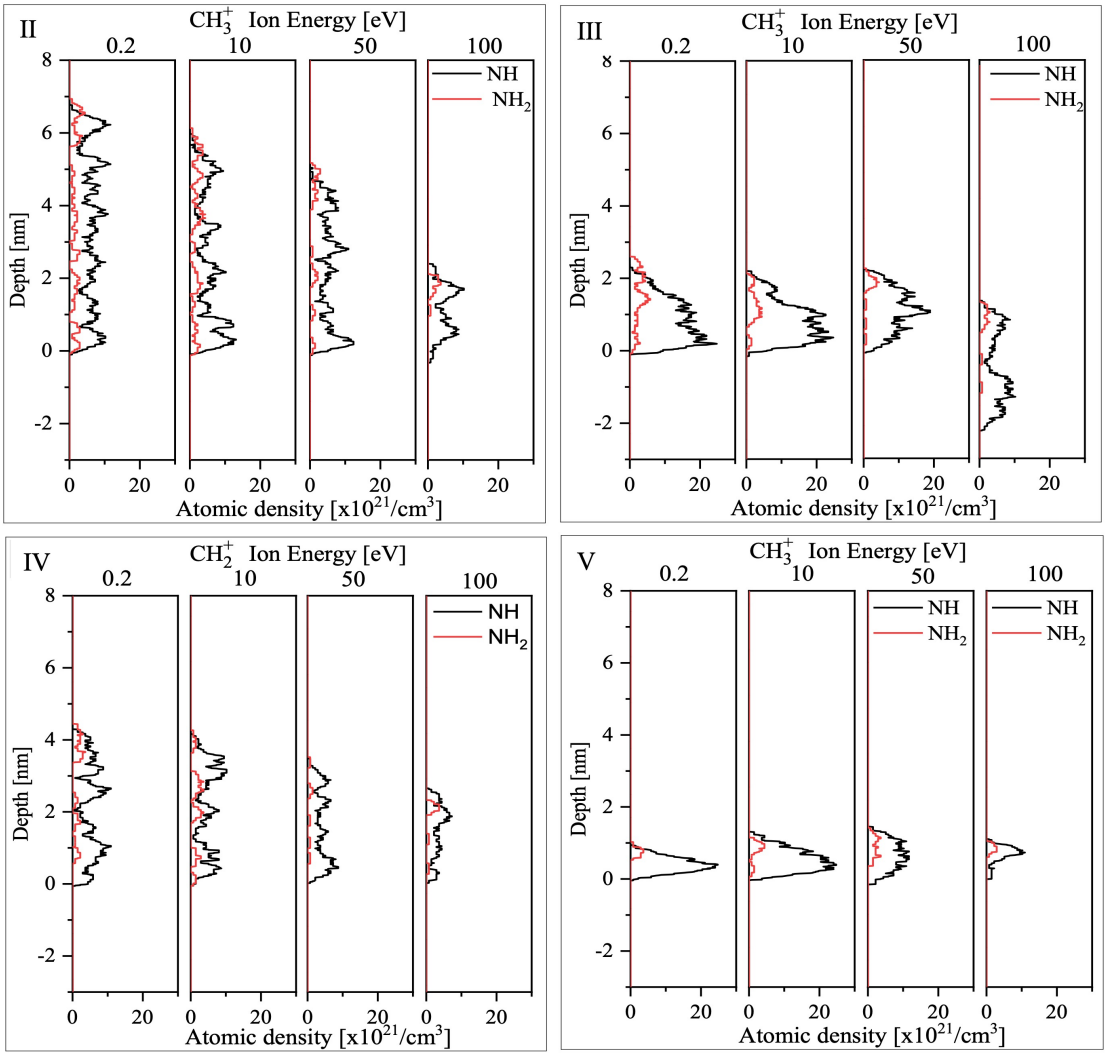

Figure B.8: Depth profiles of the atomic concentrations of secondary amines NH and primary amines NH_2 at different ion incident energies from 0.2 eV to 100 eV for Case II, III, IV, and V.

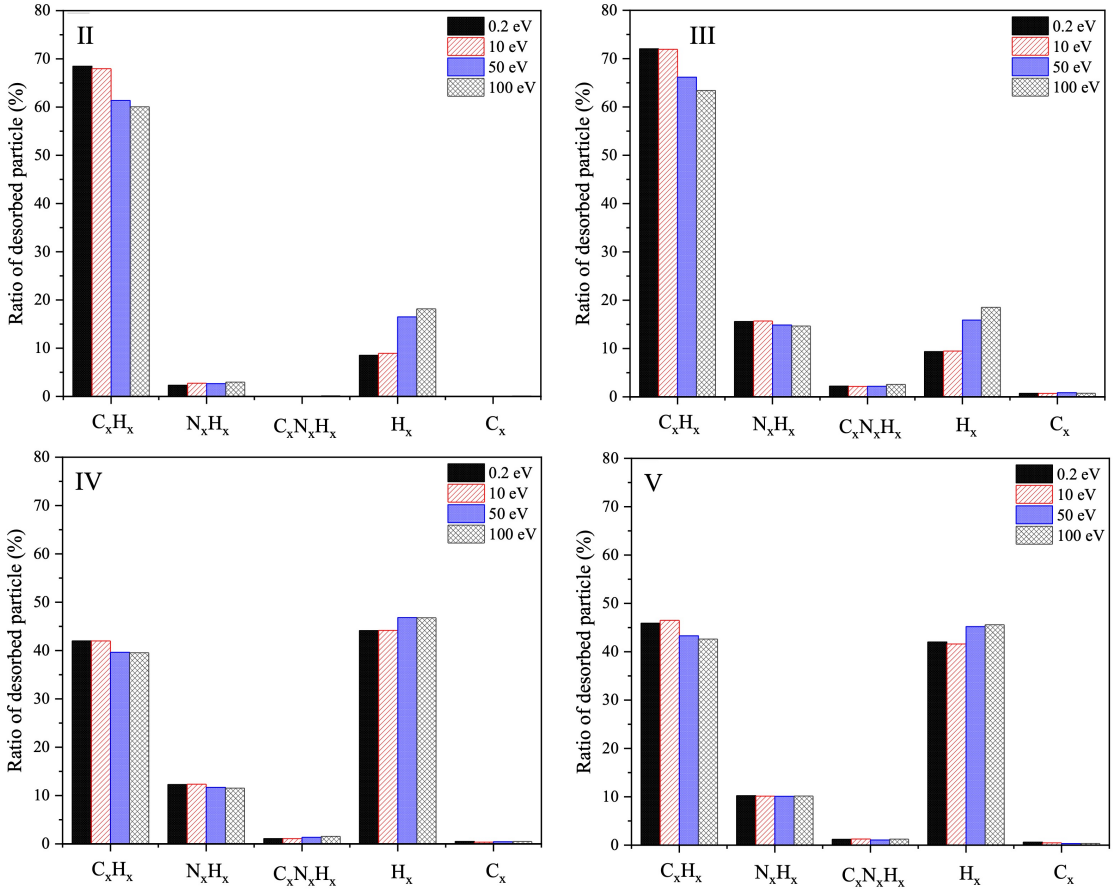

Figure B.9: Relative numbers of desorbed species during the deposition process at different ion incident energies for Case I, III, IV, and V. The ratios are relative to the total number of desorbed species during the process for each cases.

Appendix C

Amine PPs Deposited on Artificial Bone with Bipolar Pulsed Discharges - Supporting Information

C.1 Morphologies of the deposited films in MD simulation

Figure C.1 shows the morphologies of the deposited amine PP films obtained from MD simulations, corresponding to Fig. 2.10 in Chapter 2. Magnified images near the top of a deposited film are given in Fig. C.2.

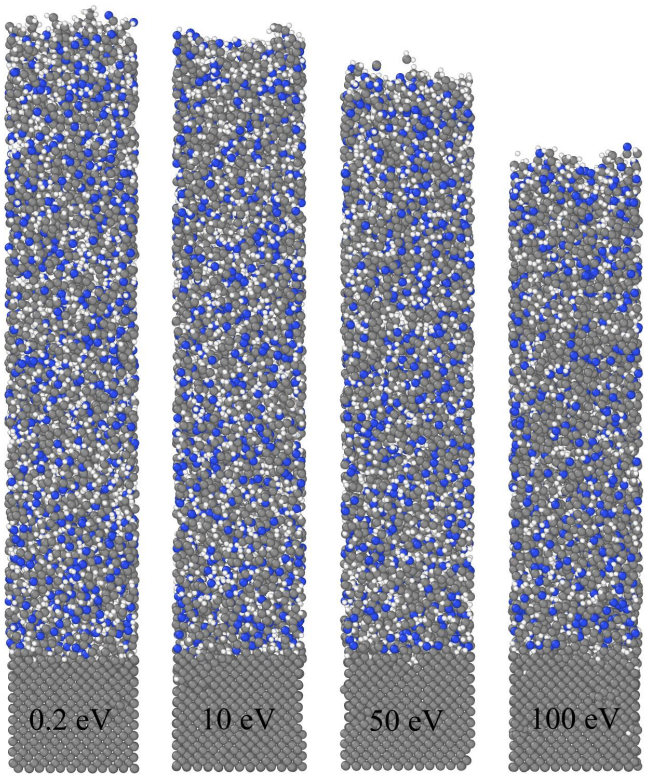

Figure C.1: Atomic representations of the deposited films given in Fig. 2.10, obtained from the MD simulations. The kinetic energy of the incident CH_2^+ ions is indicated at the bottom of each image. The grey, blue, and white spheres represent C, N, and H atoms, respectively.

C.2 The depth profiles of bond densities

Corresponding to Fig. 2.11, Fig. C.3 gives all major chemical bonds in the deposited films given in Figs. 2.10 and C.1.

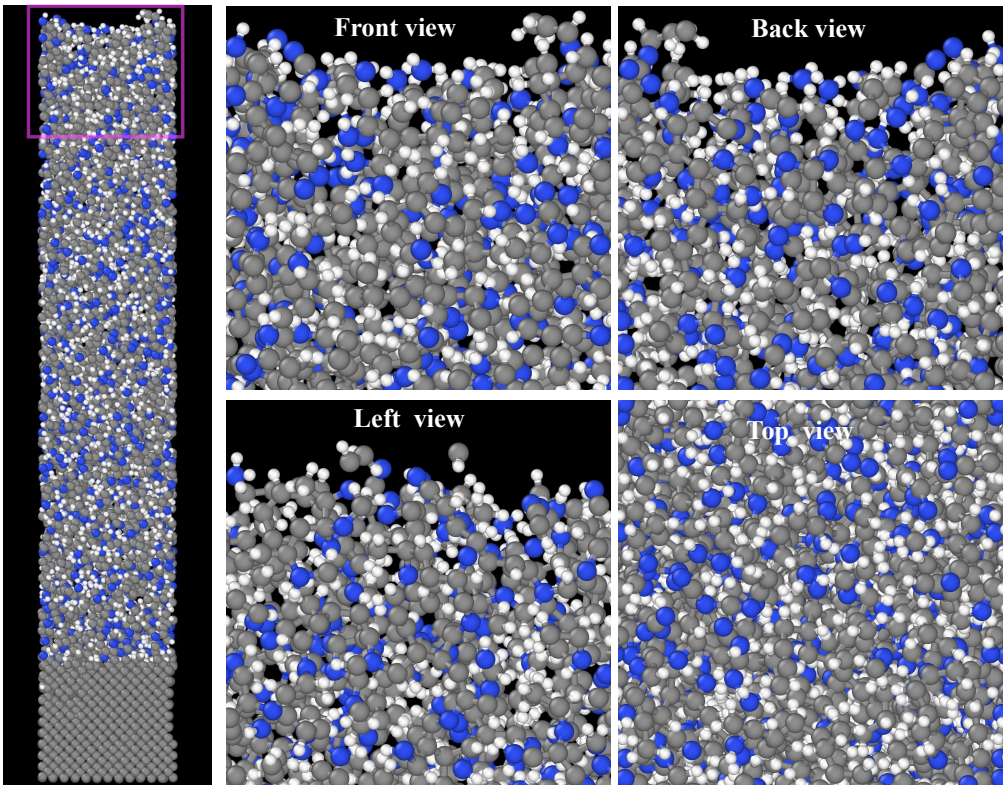

Figure C.2: Magnified images of a top surface region of the deposited film obtained from the MD simulation, corresponding to the image of Fig. C.1 for a CH_2^+ ion energy of 10 eV. The grey, blue, and white balls represent C, N, and H atoms, respectively, and the stick between two atoms represents their covalent bond.

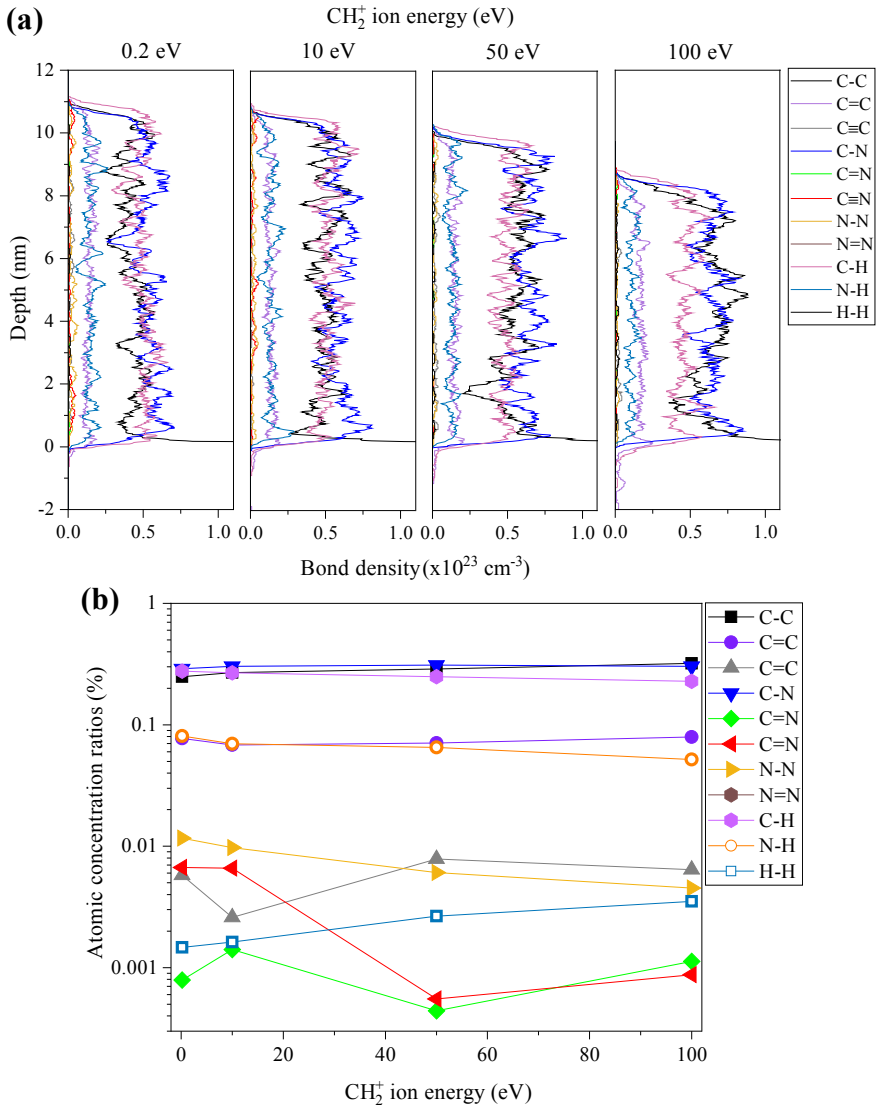

Figure C.3: Concentrations of major chemical (covalent) bonds in the deposited films obtained from the MD simulations with different kinetic energies (0.2, 10, 50, and 100 eV) of the incident CH_2^+ ions, corresponding to Fig. 2.11. (a) Depth profiles of the bond concentrations. The corresponding ion energy is given above each set of the profiles. (b) Relative concentrations of the bonds listed in (a) averaged over the deposited films as functions of the CH_2^+ ion energy. Unlike Fig. 2.11, the bond concentrations are not normalized by the C atomic concentration here; they are normalized by the total bond concentration.

Appendix D

PEEK implant functionalization with magnetron-sputtered STO - Supporting Information

D.1 Surface properties of the STO deposited films on PEEK

In this appendix, the XPS spectra of STO films on the PEEK substrate are shown in Figs. D.1 as discussed in Chapter 5. The spectra confirm the elemental composition of Sr, Ti, and O elements in the STO films at different deposition times. The depth profiling spectra of one-layer, two-layer, and three-layer are shown in Fig. D.2, D.3, D.4 corresponding to Fig. 5.7.

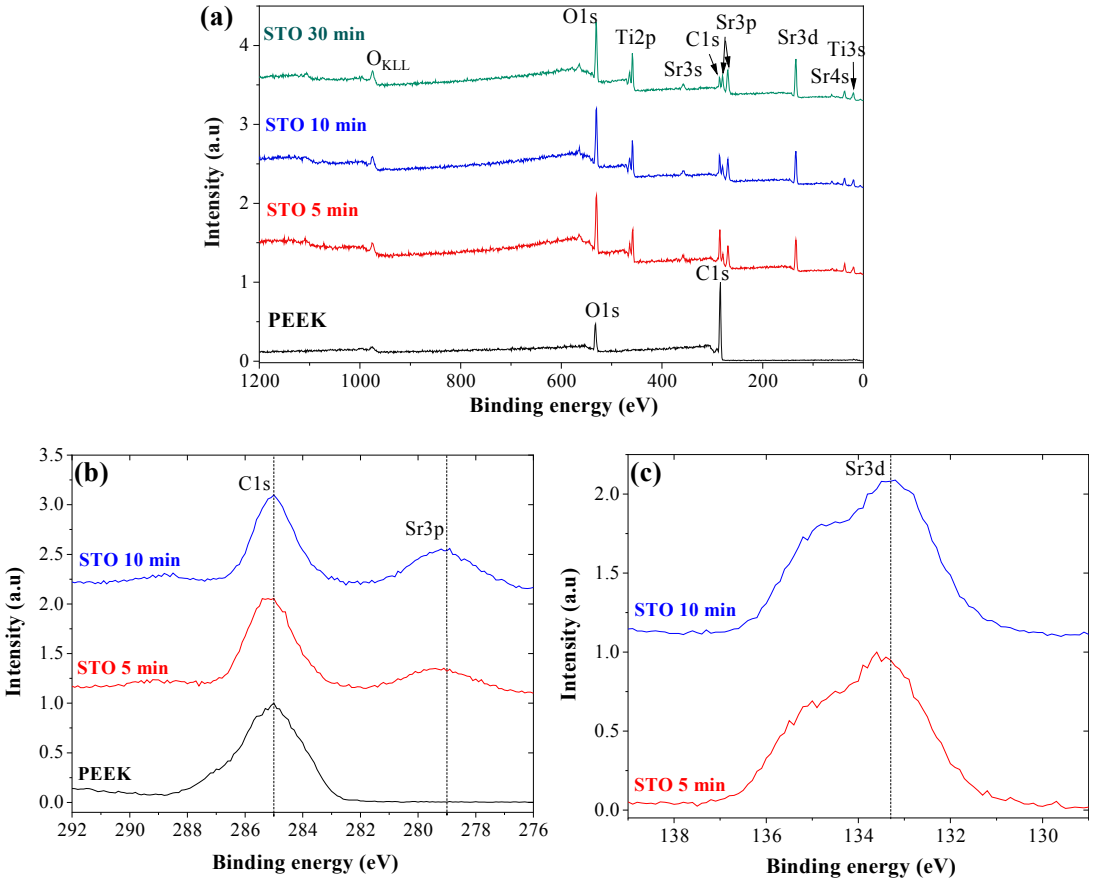

Figure D.1: The XPS spectra of Sr, Ti, and O atoms for STO I, II, and III were deposited on the PEEK substrate (a) wide spectra, (b) C 1s and Sr 3p spectra, and (c) Sr 3d spectra.

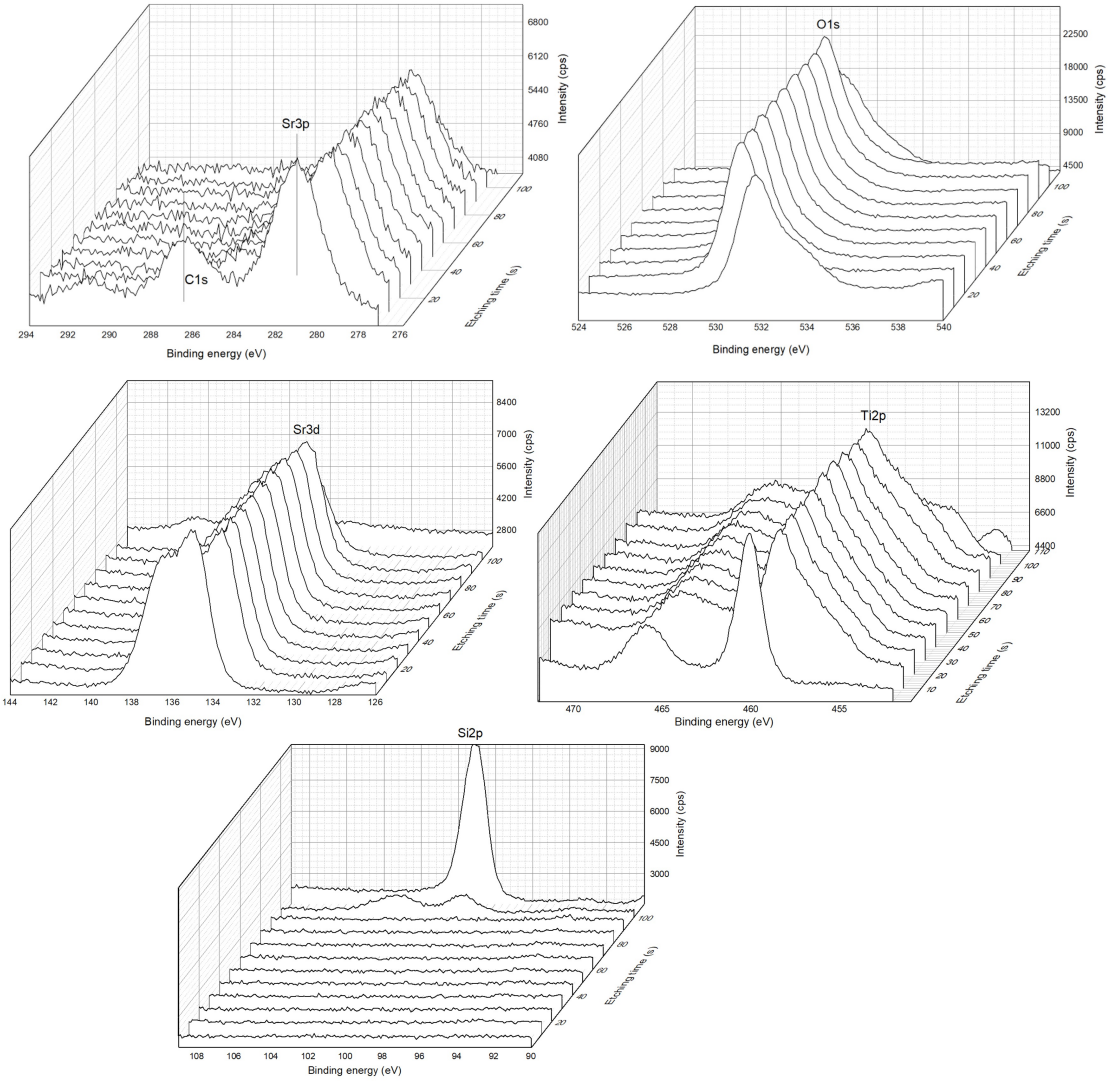

Figure D.2: Depth profiling of C, O, Sr, and Ti obtained from XPS depth profiling with a 1 keV Ar^+ ion beam for one-layer (STO III) deposition on Si substrate.

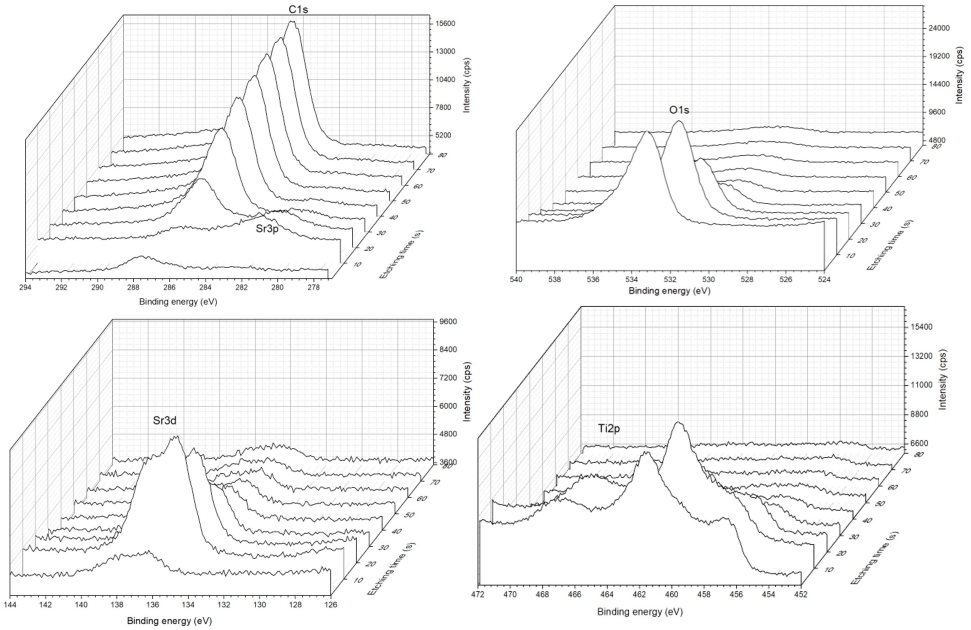

Figure D.3: Depth profiling of C, O, Sr, and Ti obtained from XPS depth profiling with a 1 keV Ar^+ ion beam for two-layer (STO II) deposition on PEEK substrate.

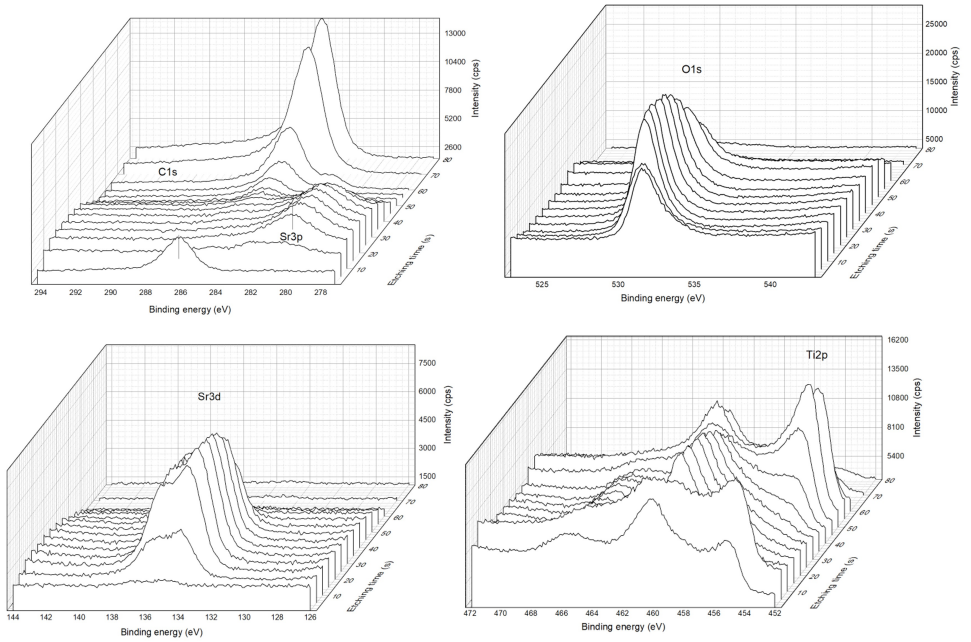

Figure D.4: Depth profiling of C, O, Sr, and Ti obtained from XPS depth profiling with a 1 keV Ar^+ ion beam for three-layer (STO II) deposition on PEEK substrate.

Bibliography

[1] Inês Peres, Pedro Rolo, and Marco P Soares dos Santos. Multifunctional smart bone implants: fiction or future?—a new perspective. *Frontiers in Bioengineering and Biotechnology*, 10:912081, 2022.

[2] Nader Salari, Niloofar Darvishi, Melika Ahmadipanah, Shamarina Shohaimi, and Masoud Mohammadi. Global prevalence of falls in the older adults: a comprehensive systematic review and meta-analysis. *Journal of orthopaedic surgery and research*, 17(1):1–13, 2022.

[3] Peter Dubruel and SV Vlierberghe. *Biomaterials for bone regeneration: novel techniques and applications*. Elsevier, 2014.

[4] Rahul Davis, Abhishek Singh, Mark James Jackson, Reginaldo Teixeira Coelho, Divya Prakash, Charalambos Panayiotou Charalambous, Waqar Ahmed, Leonardo Rosa Ribeiro da Silva, and Abner Ankit Lawrence. A comprehensive review on metallic implant biomaterials and their subtractive manufacturing. *The International Journal of Advanced Manufacturing Technology*, 120(3):1473–1530, 2022.

[5] XP Tan, YJ Tan, CSL Chow, SB Tor, and WY Yeong. Metallic powder-bed based 3d printing of cellular scaffolds for orthopaedic implants: A state-of-the-art review on manufacturing, topological design, mechanical properties and biocompatibility. *Materials Science and Engineering: C*, 76:1328–1343, 2017.

[6] Naser Mohammadzadeh Rezaei, Masakazu Hasegawa, Manabu Ishijima, Kourosh Nakhaei, Takahisa Okubo, Takashi Taniyama, Amirreza Ghassemi, Tania Tahsili, Wonhee Park, Makoto Hirota, et al. Biological and osseointegration capabilities of hierarchically (meso-/micro-/nano-scale) roughened zirconia. *International journal of nanomedicine*, pages 3381–3395, 2018.

[7] Hans K Uhthoff, Philippe Poitras, and David S Backman. Internal plate fixation of fractures: short history and recent developments. *Journal of Orthopaedic Science*, 11:118–126, 2006.

[8] Dae-Sung Lee, Yu Moriguchi, Kiyoshi Okada, Akira Myoui, Hideki Yoshikawa, and Satoshi Hamaguchi. Improvement of hydrophilicity of interconnected porous hydroxyapatite by dielectric barrier discharge plasma treatment. *IEEE Transactions on Plasma Science*, 39(11):2166–2167, 2011.

[9] Yu Moriguchi, Dae-Sung Lee, Ryota Chijimatsu, Khair Thamina, Kazuto Masuda, Dai Itsuki, Hideki Yoshikawa, Satoshi Hamaguchi, and Akira Myoui. Impact of non-thermal plasma surface modification on porous calcium hydroxyapatite ceramics for bone regeneration. *PloS one*, 13(3):e0194303, 2018.

[10] Joe Kodama, Anjar Anggraini Harumningtyas, Tomoko Ito, Miroslav Michlíček, Satoshi Sugimoto, Hidekazu Kita, Ryota Chijimatsu, Yuichiro Ukon, Junichi Kushioka, Rintaro Okada, et al. Amine modification of calcium phosphate by low-pressure plasma for bone regeneration. *Scientific reports*, 11(1):1–15, 2021.

[11] Chaoqian Zhao, Weiye Liu, Min Zhu, Chengtie Wu, and Yufang Zhu. Bioceramic-based scaffolds with antibacterial function for bone tissue engineering: A review. *Bioactive materials*, 18:383–398, 2022.

[12] Anastasiia Kashirina, Yongtao Yao, Yanju Liu, and Jinsong Leng. Biopolymers as bone substitutes: A review. *Biomaterials science*, 7(10):3961–3983, 2019.

[13] Hongpu Wei, Jinjie Cui, Kaili Lin, Jing Xie, and Xudong Wang. Recent advances in smart stimuli-responsive biomaterials for bone therapeutics and regeneration. *Bone research*, 10(1):17, 2022.

[14] Rana NS Sodhi. Application of surface analytical and modification techniques to biomaterial research. *Journal of electron spectroscopy and related phenomena*, 81(3):269–284, 1996.

[15] Paul K Chu, JY Chen, LP Wang, and Nan Huang. Plasma-surface modification of biomaterials. *Materials Science and Engineering: R: Reports*, 36(5-6):143–206, 2002.

[16] Theresia Stich, Francisca Alagboso, Tomáš Křenek, Tomáš Kovářík, Volker Alt, and Denitsa Docheva. Implant-bone-interface: Reviewing the impact of

titanium surface modifications on osteogenic processes in vitro and in vivo. *Bioengineering & translational medicine*, 7(1):e10239, 2022.

[17] Dae-Sung Lee, Yu Moriguchi, Akira Myoui, Hideki Yoshikawa, and Satoshi Hamaguchi. Efficient modification of the surface properties of interconnected porous hydroxyapatite by low-pressure low-frequency plasma treatment to promote its biological performance. *Journal of Physics D: Applied Physics*, 45(37):372001, aug 2012.

[18] Francis F Chen et al. *Introduction to plasma physics and controlled fusion*, volume 1. Springer, 1984.

[19] Michael A Lieberman and Allan J Lichtenberg. Principles of plasma discharges and materials processing. *MRS Bulletin*, 30(12):899–901, 1994.

[20] Francis F Chen and Jane P Chang. *Lecture notes on principles of plasma processing*. Springer Science & Business Media, 2012.

[21] Rachel Williams, editor. *Surface modification of biomaterials: Methods, analysis and application*. Woodhead Publishing Limited, Cambridge, UK, 2011.

[22] Gottlieb S. Oehrlein and Satoshi Hamaguchi. Foundations of low-temperature plasma enhanced materials synthesis and etching. *Plasma Sources Sci. Technol.*, 27(2):023001, 2018.

[23] T Shirafuji, H Motomura, and K Tachibana. Fourier transform infrared phase-modulated ellipsometry for in situ diagnostics of plasma–surface interactions. *Journal of Physics D: Applied Physics*, 37(6):R49, 2004.

[24] H Ki Yasuda. *Plasma polymerization*. Academic press, 2012.

[25] Jörg Friedrich. Mechanisms of plasma polymerization–reviewed from a chemical point of view. *Plasma Processes and Polymers*, 8(9):783–802, 2011.

[26] MJ Druyvesteyn and Fi M Penning. The mechanism of electrical discharges in gases of low pressure. *Reviews of Modern Physics*, 12(2):87, 1940.

[27] Hirotsugu K Yasuda. Some important aspects of plasma polymerization. *Plasma Processes and Polymers*, 2(4):293–304, 2005.

[28] Dirk Hegemann, Mohammad Mokbul Hossain, Enrico Körner, and Dawn J Balazs. Macroscopic description of plasma polymerization. *Plasma Processes and Polymers*, 4(3):229–238, 2007.

[29] Dirk Hegemann. Macroscopic investigation of reaction rates yielding plasma polymer deposition. *Journal of Physics D: Applied Physics*, 46(20):205204, 2013.

[30] Christopher L Rinsch, Xiaolan Chen, V Panchalingam, Robert C Eberhart, Jenn-Hann Wang, and Richard B Timmons. Pulsed radio frequency plasma polymerization of allyl alcohol: Controlled deposition of surface hydroxyl groups. *Langmuir*, 12(12):2995–3002, 1996.

[31] H Yasuda and M Gazicki. Biomedical applications of plasma polymerization and plasma treatment of polymer surfaces. *Biomaterials*, 3(2):68–77, 1982.

[32] AA Meyer-Plath, K Schröder, B Finke, and A Ohl. Current trends in biomaterial surface functionalization—nitrogen-containing plasma assisted processes with enhanced selectivity. *Vacuum*, 71(3):391–406, 2003.

[33] Kim Shyong Siow, Leanne Britcher, Sunil Kumar, and Hans J Griesser. Plasma methods for the generation of chemically reactive surfaces for biomolecule immobilization and cell colonization-a review. *Plasma processes and polymers*, 3(6-7):392–418, 2006.

[34] Dave Mangindaan, Wei-Hsuan Kuo, Ching-Chuan Chang, Shu-Ling Wang, Hsiu-Chi Liu, and Meng-Jiy Wang. Plasma polymerization of amine-containing thin films and the studies on the deposition kinetics. *Surface and coatings technology*, 206(6):1299–1306, 2011.

[35] Dirk Hegemann, Barbara Hanselmann, Sébastien Guimond, Giuseppino Fortunato, Marie-Noëlle Giraud, and Anne Géraldine Guex. Considering the degradation effects of amino-functional plasma polymer coatings for biomedical application. *Surface and Coatings Technology*, 255:90–95, 2014.

[36] L Štrbková, Anton Manakhov, Lenka Zajíčková, Adrian Stoica, P Veselỳ, and R Chmelík. The adhesion of normal human dermal fibroblasts to the cyclopropylamine plasma polymers studied by holographic microscopy. *Surface and Coatings Technology*, 295:70–77, 2016.

[37] F Intranuovo, E Sardella, R Gristina, M Nardulli, L White, D Howard, KM Shakesheff, MR Alexander, and P Favia. Pe-cvd processes improve cell affinity of polymer scaffolds for tissue engineering. *Surface and Coatings Technology*, 205:S548–S551, 2011.

[38] Anton Manakhov, Eva Kedroňová, Jiřina Medalová, Petra Černochová, Adam Obrusník, Miroslav Michlíček, Dmitry V Shtansky, and Lenka Za-

jíčková. Carboxyl-anhydride and amine plasma coating of pcl nanofibers to improve their bioactivity. *Materials & Design*, 132:257–265, 2017.

[39] Anton Manakhov, David Nečas, Jan Čechal, David Pavliňák, Marek Eliáš, and Lenka Zajíčková. Deposition of stable amine coating onto polycaprolactone nanofibers by low pressure cyclopropylamine plasma polymerization. *Thin Solid Films*, 581:7–13, 2015.

[40] F Intranuovo, R Gristina, L Fracassi, L Lacitignola, A Crovace, and P Favia. Plasma processing of scaffolds for tissue engineering and regenerative medicine. *Plasma Chemistry and Plasma Processing*, 36(1):269–280, 2016.

[41] Anton Manakhov, Elizaveta S Permyakova, Sergey Ershov, Alexander Sheveyko, Andrey Kovalskii, Josef Polčák, Irina Y Zhitnyak, Natalia A Gloushankova, Lenka Zajíčková, and Dmitry V Shtansky. Bioactive ticapcon-coated pcl nanofibers as a promising material for bone tissue engineering. *Applied Surface Science*, 479:796–802, 2019.

[42] Lu Cheng, Rouba Ghobeira, Pieter Cools, Zhen Liu, Keping Yan, Nathalie De Geyter, and Rino Morent. Comparative study of different nitrogen-containing plasma modifications applied on 3d porous pcl scaffolds and 2d pcl films. *Applied Surface Science*, 516:146067, 2020.

[43] Mahtab Asadian, Ke Vin Chan, Tim Egghe, Yuliia Onyshchenko, Silvia Grande, Heidi Declercq, Pieter Cools, Rino Morent, and Nathalie De Geyter. Acrylic acid plasma polymerization and post-plasma ethylene diamine graft-

ing for enhanced bone marrow mesenchymal stem cell behaviour on polycaprolactone nanofibers. *Applied Surface Science*, 563:150363, 2021.

[44] Fackson Mwale, Sonia Rampersad, Juan-Carlos Ruiz, Pierre-Luc Girard-Lauriault, Alain Petit, John Antoniou, Sophie Lerouge, and Michael Wertheimer. Amine-rich cell-culture surfaces for research in orthopedic medicine. *Plasma Medicine*, 1(2), 2011.

[45] Sung Woon Myung, Yeong Mu Ko, and Byung Hoon Kim. Effect of plasma surface functionalization on preosteoblast cells spreading and adhesion on a biomimetic hydroxyapatite layer formed on a titanium surface. *Applied surface science*, 287:62–68, 2013.

[46] Claudia Bergemann, Matthias Cornelsen, Antje Quade, Thorsten Laube, Matthias Schnabelrauch, Henrike Rebl, Volker Weißmann, Hermann Seitz, and Barbara Nebe. Continuous cellularization of calcium phosphate hybrid scaffolds induced by plasma polymer activation. *Materials Science and Engineering: C*, 59:514–523, 2016.

[47] Xujie Liu, Qingling Feng, Akash Bachhuka, and Krasimir Vasilev. Surface modification by allylamine plasma polymerization promotes osteogenic differentiation of human adipose-derived stem cells. *ACS applied materials & interfaces*, 6(12):9733–9741, 2014.

[48] Kiyotaka Wasa, Isaku Kanno, and Hidetoshi Kotera. *Handbook of sputter deposition technology: fundamentals and applications for functional thin films, nano-materials and MEMS*. William Andrew, 2012.

[49] Krishna Seshan. *Handbook of thin film deposition*. William Andrew, 2012.

[50] Yan Yonggang, JGC Wolke, Li Yubao, and JA Jansen. The influence of discharge power and heat treatment on calcium phosphate coatings prepared by rf magnetron sputtering deposition. *Journal of Materials Science: Materials in Medicine*, 18:1061–1069, 2007.

[51] K vd Takahashi, JJJP Van Den Beucken, JGC Wolke, T Hayakawa, N Nishiyama, and JA Jansen. Characterization and in vitro evaluation of biphasic calcium pyrophosphate–tricalciumphosphate radio frequency magnetron sputter coatings. *Journal of Biomedical Materials Research Part A: An Official Journal of The Society for Biomaterials, The Japanese Society for Biomaterials, and The Australian Society for Biomaterials and the Korean Society for Biomaterials*, 84(3):682–690, 2008.

[52] AR Boyd, GA Burke, H Duffy, Maria Holmberg, C O'Kane, BJ Meenan, and P Kingshott. Sputter deposited bioceramic coatings: surface characterisation and initial protein adsorption studies using surface-maldi-ms. *Journal of Materials Science: Materials in Medicine*, 22:71–84, 2011.

[53] Roman A Surmenev. A review of plasma-assisted methods for calcium phosphate-based coatings fabrication. *Surface and Coatings Technology*, 206(8-9):2035–2056, 2012.

[54] M Jelínek, M Weiserová, T Kocourek, M Zezulová, and J Strnad. Biomedical properties of laser prepared silver-doped hydroxyapatite. *Laser Physics*, 21:1265–1269, 2011.

[55] MA Surmeneva, RA Surmenev, MV Chaikina, AA Kachaev, VF Pichugin, and M Epple. Phase and elemental composition of silicon-containing hydroxyapatite-based coatings fabricated by rf-magnetron sputtering for medical implants. *Inorganic Materials: Applied Research*, 4:227–235, 2013.

[56] C Capuccini, P Torricelli, F Sima, E Boanini, C Ristoscu, B Bracci, G Socol, M Fini, IN Mihailescu, and A Bigi. Strontium-substituted hydroxyapatite coatings synthesized by pulsed-laser deposition: in vitro osteoblast and osteoclast response. *Acta biomaterialia*, 4(6):1885–1893, 2008.

[57] Junyu Shi, Yuan Li, Yingxin Gu, Shichong Qiao, Xiaomeng Zhang, and Hongchang Lai. Effect of titanium implants with strontium incorporation on bone apposition in animal models: A systematic review and meta-analysis. *Scientific Reports*, 7(1):15563, 2017.

[58] Takashi Kaito, Akira Myoui, Kunio Takaoka, Naoto Saito, Masataka Nishikawa, Noriyuki Tamai, Hajime Ohgushi, and Hideki Yoshikawa. Potentiation of the activity of bone morphogenetic protein-2 in bone regeneration by a pla–peg/hydroxyapatite composite. *Biomaterials*, 26(1):73–79, 2005.

[59] Iis Sopyan, M Mel, S Ramesh, and KA Khalid. Porous hydroxyapatite for artificial bone applications. *Science and Technology of Advanced Materials*, 8(1-2):116, 2007.

[60] William R Walsh, Frank Vizesi, Dean Michael, Jason Auld, Andy Langdown, Rema Oliver, Yan Yu, Hiroyuki Irie, and Warwick Bruce. β-tcp bone graft

substitutes in a bilateral rabbit tibial defect model. *Biomaterials*, 29(3):266–271, 2008.

[61] Rachel Williams. *Surface modification of biomaterials: Methods analysis and applications*. Elsevier, 2010.

[62] Hideki Yoshikawa and Akira Myoui. Bone tissue engineering with porous hydroxyapatite ceramics. *Journal of Artificial Organs*, 8(3):131–136, 2005.

[63] Kensuke Kuroda and Masazumi Okido. Hydroxyapatite coating of titanium implants using hydroprocessing and evaluation of their osteoconductivity. *Bioinorganic chemistry and applications*, 2012, 2012.

[64] Dae-Sung Lee, Yu Moriguchi, Akira Myoui, Hideki Yoshikawa, and Satoshi Hamaguchi. Efficient modification of the surface properties of interconnected porous hydroxyapatite by low-pressure low-frequency plasma treatment to promote its biological performance. *Journal of Physics D: Applied Physics*, 45(37):372001, 2012.

[65] Anjar Anggraini Harumningtyas, Tomoko Ito, Masato Ikuta, Takashi Kaito, and Satoshi Hamaguchi. Polyetheretherketone (PEEK) implant functionalization with magnetron-sputtered $SrTiO_3$ for regenerative medicine. *Plasma Medicine*, 13(3):53–67, 2023.

[66] Daniella Marx, Alireza Rahimnejad Yazdi, Marcello Papini, and Mark Towler. A review of the latest insights into the mechanism of action of strontium in bone. *Bone reports*, 12:100273, 2020.

[67] Qiang Chen, Renate Förch, and Wolfgang Knoll. Characterization of pulsed plasma polymerization allylamine as an adhesion layer for dna adsorption/hybridization. *Chemistry of materials*, 16(4):614–620, 2004.

[68] Renate Förch, Zhihong Zhang, and Wolfgang Knoll. Soft plasma treated surfaces: tailoring of structure and properties for biomaterial applications. *Plasma processes and polymers*, 2(5):351–372, 2005.

[69] K. S. Siow, L. Britcher, S. Kumar, and H. J. Griesser. Plasma methods for the generation of chemically reactive surfaces for biomolecule immobilization and cell colonization - a review. *Plasma Processes and Polymers*, 3(6-7):392–418, 2006.

[70] Florina Truica-Marasescu and Michael R Wertheimer. Nitrogen-rich plasma-polymer films for biomedical applications. *Plasma processes and polymers*, 5(1):44–57, 2008.

[71] Juan-Carlos Ruiz, Amélie St-Georges-Robillard, Charles Thérésy, Sophie Lerouge, and Michael R Wertheimer. Fabrication and characterisation of amine-rich organic thin films: Focus on stability. *Plasma Processes Polym.*, 7(9-10):737–753, 2010.

[72] Satoshi Sugimoto, Masato Kiuchi, Seiji Takechi, Katsutoshi Tanaka, and Seiichi Goto. Inverter plasma discharge system. *Surface and Coatings Technology*, 136(1-3):65–68, 2001.

[73] Seiji Takechi, Satoshi Sugimoto, Masato Kiuchi, Katsutoshi Tanaka, and

Seiichi Goto. Operational parameter effects on inverter plasma performance. *Surface and Coatings Technology*, 136(1-3):69–72, 2001.

[74] Zoltán Donkó, Lenka Zajičková, Satoshi Sugimoto, Anjar Anggraini Harumningtyas, and Satoshi Hamaguchi. Modeling characterisation of a bipolar pulsed discharge. *Plasma Sources Science and Technology*, 29(10):104001, 2020.

[75] Pietro Favia, Marco Vito Stendardo, and Riccardo d'Agostino. Selective grafting of amine groups on polyethylene by means of nh3- h2 rf glow discharges. *Plasmas and polymers*, 1(2):91–112, 1996.

[76] Johanna Dorst, Marianne Vandenbossche, Martin Amberg, Laetitia Bernard, Patrick Rupper, K-D Weltmann, Katja Fricke, and Dirk Hegemann. Improving the stability of amino-containing plasma polymer films in aqueous environments. *Langmuir*, 33(40):10736–10744, 2017.

[77] A Choukourov, H Biederman, I Kholodkov, D Slavinska, M Trchova, and A Hollander. Properties of amine-containing coatings prepared by plasma polymerization. *Journal of applied polymer science*, 92(2):979–990, 2004.

[78] Marianne Vandenbossche, Maria-Isabel Butron Garcia, Urs Schütz, Patrick Rupper, Martin Amberg, and Dirk Hegemann. Initial growth of functional plasma polymer nanofilms. *Plasma Chem. Plasma P.*, 36:667–677, 2016.

[79] Damien Thiry, Adrien Chauvin, Abdel-Aziz El Mel, Christophe Cardinaud, Jonathan Hamon, Eric Gautron, Nicolas Stephant, Agnès Granier, and Pierre-Yves Tessier. Tailoring the chemistry and the nano-architecture of

organic thin films using cold plasma processes. *Plasma Processes and Polymers*, 14(11):1700042, 2017.

[80] Anjar Anggraini Harumningtyas, Tomoko Ito, Michiro Isobe, Lenka Zajíčková, and Satoshi Hamaguchi. Molecular dynamics simulation of amine formation in plasma-enhanced chemical vapor deposition with hydrocarbon and amino radicals. *J. Vac. Sci. Technol. A*, 41(6), 2023.

[81] H Kojima, H Toyoda, and H Sugai. Observation of ch2 radical and comparison with ch3 radical in a rf methane discharge. *Applied physics letters*, 55(13):1292–1294, 1989.

[82] H Sugai, H Kojima, A Ishida, and H Toyoda. Spatial distribution of ch3 and ch2 radicals in a methane rf discharge. *Applied Physics Letters*, 56(26):2616–2618, 1990.

[83] A Von Keudell and W Möller. A combined plasma-surface model for the deposition of c: H films from a methane plasma. *Journal of applied physics*, 75(12):7718–7727, 1994.

[84] DJ Dagel, CM Mallouris, and JR Doyle. Radical and film growth kinetics in methane radio-frequency glow discharges. *Journal of applied physics*, 79(11):8735–8747, 1996.

[85] Esther Carrasco, Miguel Jiménez-Redondo, Isabel Tanarro, and Víctor J. Herrero. Neutral and ion chemistry in low pressure dc plasmas of H_2/N_2 mixtures: routes for the efficient production of NH_3 and NH_4^+. *Phys. Chem. Chem. Phys.*, 13:19561–19572, 2011.

[86] T Schneider and E Stoll. Molecular-dynamics study of a three-dimensional one-component model for distortive phase transitions. *Physical Review B*, 17(3):1302, 1978.

[87] Herman JC Berendsen, JPM van Postma, Wilfred F Van Gunsteren, ARHJ DiNola, and Jan R Haak. Molecular dynamics with coupling to an external bath. *The Journal of chemical physics*, 81(8):3684–3690, 1984.

[88] Hideaki Yamada and Satoshi Hamaguchi. Numerical analyses of surface interactions between radical beams and organic polymer surfaces. *Plasma Phys. Control. Fusion*, 47(5A):A11–A18, apr 2005.

[89] Hideaki Yamada and Satoshi Hamaguchi. Molecular-dynamics simulations of organic polymer etching by hydrocarbon beams. *J. Appl. Phys.*, 96(11):6147–6152, 2004.

[90] Masashi Yamashiro, Hideaki Yamada, and Satoshi Hamaguchi. Molecular dynamics simulations of organic polymer dry etching at high substrate temperatures. *Jpn. J. Appl. Phys.*, 46(4A):1692–1699, apr 2007.

[91] Yasuo Murakami, Seishi Horiguchi, and Satoshi Hamaguchi. Molecular dynamics simulation of the formation of sp3 hybridized bonds in hydrogenated diamondlike carbon deposition processes. *Physical Review E*, 81(4):041602, 2010.

[92] Neal Fairley, Vincent Fernandez, Mireille Richard-Plouet, Catherine Guillot-Deudon, John Walton, Emily Smith, Delphine Flahaut, Mark Greiner, Mark Biesinger, Sven Tougaard, et al. Systematic and collaborative approach to

problem solving using X-ray photoelectron spectroscopy. *Appl. Surf. Sci. Advances*, 5:100112, 2021.

[93] Thomas R Gengenbach, Ronald C Chatelier, and Hans J Griesser. Correlation of the nitrogen 1s and oxygen 1s xps binding energies with compositional changes during oxidation of ethylene diamine plasma polymers. *Surface and interface analysis*, 24(9):611–619, 1996.

[94] Krasimir Vasilev, Leanne Britcher, Ana Casanal, and Hans J Griesser. Solvent-induced porosity in ultrathin amine plasma polymer coatings. *The Journal of Physical Chemistry B*, 112(35):10915–10921, 2008.

[95] Pierre-Luc Girard-Lauriault, Paul M Dietrich, Thomas Gross, Thomas Wirth, and Wolfgang ES Unger. Chemical characterization of the long-term ageing of nitrogen-rich plasma polymer films under various ambient conditions. *Plasma processes and polymers*, 10(4):388–395, 2013.

[96] Reginald William Blake Pearse, Alfred Gordon Gaydon, Reginald William Blake Pearse, and Alfred Gordon Gaydon. *The identification of molecular spectra*, volume 297. Chapman and Hall London, 1976.

[97] KJ Clay, SP Speakman, GAJ Amaratunga, and SRP Silva. Characterization of a-c: H: N deposition from ch4/n2 rf plasmas using optical emission spectroscopy. *Journal of applied physics*, 79(9):7227–7233, 1996.

[98] P Jamroz and W Zyrnicki. Optical emission spectroscopy study for nitrogen–acetylene–argon and nitrogen–acetylene–helium 100 khz and dc discharges. *Vacuum*, 84(7):940–946, 2010.

[99] Brian N Chapman. *Glow Discharge Processes: Sputtering and Plasma Etching*. Wiley-Interscience, 1980.

[100] Satoshi Hamaguchi. Modeling and simulation methods for plasma processing. *IBM J. Res. Develp.*, 43(1.2):199–215, 1999.

[101] Michael A. Lieberman and Allan J. Lichtenberg. *Principles of Plasma Discharges and Materials Processing (2nd ed.)*. Wiley-Interscience, New Jersey, 2005.

[102] Kazuo Nojiri. *Dry Etching Technology for Semiconductors*. Springer, 2015.

[103] Toshiaki Makabe and Zoran Lj Petrovic. *Plasma Electronics*. Routledge, Boca Raton, 2016.

[104] I Adamovich, S D Baalrud, A Bogaerts, P J Bruggeman, M Cappelli, V Colombo, U Czarnetzki, U Ebert, J G Eden, P Favia, D B Graves, S Hamaguchi, G Hieftje, M Hori, I D Kaganovich, U Kortshagen, M J Kushner, N J Mason, S Mazouffre, S Mededovic Thagard, H-R Metelmann, A Mizuno, E Moreau, A B Murphy, B A Niemira, G S Oehrlein, Z Lj Petrovic, L C Pitchford, Y-K Pu, S Rauf, O Sakai, S Samukawa, S Starikovskaia, J Tennyson, K Terashima, M M Turner, M C M van de Sanden, and A Vardelle. The 2017 plasma roadmap: Low temperature plasma science and technology. *J. Phys. D: Appl. Phys.*, 50(32):323001, 2017.

[105] Klaus-Dieter Weltmann, Juergen F. Kolb, Marcin Holub, Dirk Uhrlandt, Milan imek, Kostya (Ken) Ostrikov, Satoshi Hamaguchi, Uros Cvelbar, Mirko,

Bruce Locke, Alexander Fridman, Pietro Favia, and Kurt Becker. The future for plasma science and technology. *Plasma Processes and Polymers*, 16(1):1800118, 2019.

[106] Karsten Arts, Satoshi Hamaguchi, Tomoko Ito, Kazuhiro Karahashi, Harm Knoops, Adriaan Mackus, and Wilhelmus M.M. Kessels. Foundations of atomic-level plasma processing in nanoelectronics. *Plasma Sources Science and Technology*, 2022.

[107] I Adamovich, S Agarwal, E Ahedo, L L Alves, S Baalrud, N Babaeva, A Bogaerts, A Bourdon, P J Bruggeman, C Canal, E H Choi, S Coulombe, Z Donkó, D B Graves, S Hamaguchi, D Hegemann, M Hori, H-H Kim, G M W Kroesen, M J Kushner, A Laricchiuta, X Li, T E Magin, S Mededovic Thagard, V Miller, A B Murphy, G S Oehrlein, N Puac, R M Sankaran, S Samukawa, M Shiratani, M Šimek, N Tarasenko, K Terashima, E Thomas Jr, J Trieschmann, S Tsikata, M M Turner, I J van der Walt, M C M van de Sanden, and T von Woedtke. The 2022 plasma roadmap: low temperature plasma science and technology. *J. Phys. D: Appl. Phys.*, 55(37):373001, July 2022.

[108] Riccardo d'Agostino. *Plasma Deposition, Treatment, and Etching of Polymers*. Academic Press, Inc., 1990.

[109] Damien Thiry, Stephanos Konstantinidis, Jérôme Cornil, and Rony Snyders. Plasma diagnostics for the low-pressure plasma polymerization process: A critical review. *Thin Solid Films*, 606:19–44, 2016.

[110] Zhilu Yang, Jin Wang, Rifang Luo, Xin Li, Si Chen, Hong Sun, and Nan Huang. Improved hemocompatibility guided by pulsed plasma tailoring the surface amino functionalities of tio2 coating for covalent immobilization of heparin. *Plasma Processes and Polymers*, 8(9):850–858, 2011.

[111] Anton Manakhov, Lenka Zajíčková, Marek Eliáš, Jan Čechal, Josef Polčák, Jaroslav Hnilica, Štěpánka Bittnerová, and David Nečas. Optimization of cyclopropylamine plasma polymerization toward enhanced layer stability in contact with water. *Plasma Processes and Polymers*, 11(6):532–544, 2014.

[112] Jan Trieschmann and Dirk Hegemann. Plasma polymerization at different positions in an asymmetric ethylene discharge. *Journal of Physics D: Applied Physics*, 44(47):475201, 2011.

[113] Seiji Takechi, Satoshi Sugimoto, Masato Kiuchi, Katsutoshi Tanaka, and Seiichi Goto. Operational parameter effects on inverter plasma performance. *Surface and Coatings Technology*, 136(1-3):69–72, 2001.

[114] Anjar Anggraini Harumningtyas, Tomoko Ito, Satoshi Sugimoto, Joe Kodama, Takashi Kaito, Chieko Asamori, Miroslav Michlíček, David Nečas, Lenka Zajíčková, and Satoshi Hamaguchi. Amine Rich Plasma Polymerization using Inverter Plasmas for Orthopaedic Application. In *Proc. of Int. Symp. on Plasma Chemistry (ISPC)*, pages 8–10, Italy, 2019. ISPC24.

[115] Hans J Griesser, Ronald C Chatelier, Thomas R Gengenbach, Graham Johnson, and John G Steele. Growth of human cells on plasma polymers: putative

role of amine and amide groups. *Journal of Biomaterials Science, Polymer Edition*, 5(6):531–554, 1994.

[116] D. Hegemann. 4.09 - plasma polymer deposition and coatings on polymers. In Saleem Hashmi, Gilmar Ferreira Batalha, Chester J. Van Tyne, and Bekir Yilbas, editors, *Comprehensive Materials Processing*, pages 201–228. Elsevier, Oxford, 2014.

[117] Anton Manakhov, Marie Landová, Jiřina Medalová, Miroslav Michlíček, Josef Polčák, David Nečas, and Lenka Zajíčková. Cyclopropylamine plasma polymers for increased cell adhesion and growth. *Plasma Processes and Polymers*, 14(7):1600123, 2017.

[118] Callum AC Stewart, Behnam Akhavan, Juichien Hung, Shisan Bao, Jun-Hyeog Jang, Steven G Wise, and Marcela MM Bilek. Multifunctional protein-immobilized plasma polymer films for orthopedic applications. *ACS Biomater. Sci. Eng.*, 4(12):4084–4094, 2018.

[119] P Černochová, L Blahová, J Medalová, D Nečas, M Michlíček, P Kaushik, J Přibyl, J Bartošíková, A Manakhov, L Bačáková, et al. Cell type specific adhesion to surfaces functionalised by amine plasma polymers. *Scientific reports*, 10(1):1–14, 2020.

[120] Dae-Sung Lee, Yu Moriguchi, Kiyoshi Okada, Akira Myoui, Hideki Yoshikawa, and Satoshi Hamaguchi. Improvement of hydrophilicity of interconnected porous hydroxyapatite by dielectric barrier discharge plasma treatment. *IEEE Transactions on Plasma Science*, 39(11):2166–2167, 2011.

[121] Dae-Sung Lee, Yu Moriguchi, Akira Myoui, Hideki Yoshikawa, and Satoshi Hamaguchi. Efficient modification of the surface properties of interconnected porous hydroxyapatite by low-pressure low-frequency plasma treatment to promote its biological performance. *Journal of Physics D: Applied Physics*, 45(37):372001, aug 2012.

[122] Yu Moriguchi, Dae-Sung Lee, Ryota Chijimatsu, Khair Thamina, Kazuto Masuda, Dai Itsuki, Hideki Yoshikawa, Satoshi Hamaguchi, and Akira Myoui. Impact of non-thermal plasma surface modification on porous calcium hydroxyapatite ceramics for bone regeneration. *PLOS ONE*, 13(3):1–18, 03 2018.

[123] Anton Manakhov, Miroslav Michlicek, Alexandre Felten, Jean-Jacques Pireaux, David Necas, and Lenka Zajickova. XPS depth profiling of derivatized amine and anhydride plasma polymers: Evidence of limitations of the derivatization approach. *Applied Surface Science*, 394:578–585, 2017.

[124] Anton Manakhov, Ekaterina Makhneva, Petr Skládal, David Nečas, Jan Čechal, Lukáš Kalina, Marek Eliáš, and Lenka Zajíčková. The robust bio-immobilization based on pulsed plasma polymerization of cyclopropylamine and glutaraldehyde coupling chemistry. *Applied Surface Science*, 360:28–36, 2016.

[125] Q Cheng, K Komvopoulos, and S Li. Plasma-assisted heparin conjugation on electrospun poly (l-lactide) fibrous scaffolds. *Journal of Biomedical Materials Research Part A*, 102(5):1408–1414, 2014.

[126] Xiao Chen, Zhiqiang Chen, Ludovic F Dumée, Luke A O'Dell, Johan Du Plessis, Riccardo d'Agostino, Xiujuan J Dai, and Kevin Magniez. Grafting of n-moieties onto octa-methyl polyhedral oligomeric silsesquioxane microstructures by sequential continuous wave and pulsed plasma. *Plasma Processes and Polymers*, 14(10):1600244, 2017.

[127] Ke Vin Chan, Mahtab Asadian, Iuliia Onyshchenko, Heidi Declercq, Rino Morent, and Nathalie De Geyter. Biocompatibility of cyclopropylamine-based plasma polymers deposited at sub-atmospheric pressure on poly (ε-caprolactone) nanofiber meshes. *Nanomaterials*, 9(9):1215, 2019.

[128] J. M. Haile. *Molecular Dynamics Simulation: Elementary Methods*. John Wiley and Sons, New York, 1997.

[129] M. P. Allen and D. J. Tildesley. *Computer simulation of liquids*. Oxford University Press, 2nd edition, 2017.

[130] David B Graves and Pascal Brault. Molecular dynamics for low temperature plasma–surface interaction studies. *J. Phys. D: Appl. Phys.*, 42(19):194011, 2009.

[131] Donald W. Brenner. Empirical potential for hydrocarbons for use in simulating the chemical vapor deposition of diamond films. *Phys. Rev. B*, 42:9458–9471, Nov 1990.

[132] Masafumi Taguchi and Satoshi Hamaguchi. Molecular dynamics study on Ar ion bombardment effects in amorphous SiO2 deposition processes. *Journal of Applied Physics*, 100(12), 12 2006. 123305.

[133] Masafumi Taguchi and Satoshi Hamaguchi. Numerical analysis of incident angle effects in reactive sputtering deposition of amorphous sio2. *Japanese Journal of Applied Physics*, 45(10S):8163, oct 2006.

[134] Masafumi Taguchi and Satoshi Hamaguchi. Md simulations of amorphous sio2 thin film formation in reactive sputtering deposition processes. *Thin Solid Films*, 515(12):4879–4882, 2007. The Third International Symposium on Dry Process (DPS 2005).

[135] Miroslav Michlíček, Satoshi Hamaguchi, and Lenka Zajíčková. Molecular dynamics simulation of amine groups formation during plasma processing of polystyrene surfaces. *Plasma Sources Science and Technology*, 29(10):105020, 2020.

[136] Masashi Yamashiro, Hideaki Yamada, and Satoshi Hamaguchi. Molecular dynamics simulation study on substrate temperature dependence of sputtering yields for an organic polymer under ion bombardment. *J. Appl. Phys.*, 101(4):046108, 2007.

[137] Masashi Yamashiro, Hideaki Yamada, and Satoshi Hamaguchi. Molecular dynamics simulations for nitridation of organic polymer surfaces due to hydrogen-nitrogen ion beam injections. *Thin Solid Films*, 516(11):3449–3453, 2008. Proceedings of the International Symposium on Dry Process (DPS 2006) Nagoya, Japan, November 29-30, 2006.

[138] Keita Miyake, Tomoko Ito, Michiro Isobe, Kazuhiro Karahashi, Masanaga Fukasawa, Kazunori Nagahata, Tetsuya Tatsumi, and Satoshi Hamaguchi.

Characterization of polymer layer formation during SiO_2/SiN etching by fluoro/hydrofluorocarbon plasmas. *Jpn. J. Appl. Phys.*, 53(3S2):03DD02, jan 2014.

[139] Frank H Stillinger and Thomas A Weber. Computer simulation of local order in condensed phases of silicon. *Physical review B*, 31(8):5262, 1985.

[140] Thomas A Weber and Frank H Stillinger. Dynamical branching during fluorination of the dimerized si (100) surface: A molecular dynamics study. *The Journal of chemical physics*, 92(10):6239–6245, 1990.

[141] H Ohta and S Hamaguchi. Classical interatomic potentials for si–o–f and si–o–cl systems. *The Journal of Chemical Physics*, 115(14):6679–6690, 2001.

[142] H Ohta and S Hamaguchi. Molecular dynamics simulation of silicon and silicon dioxide etching by energetic halogen beams. *Journal of Vacuum Science & Technology A: Vacuum, Surfaces, and Films*, 19(5):2373–2381, 2001.

[143] Zorica Buser, Darrel S Brodke, Jim A Youssef, Hans-Joerg Meisel, Sue Lynn Myhre, Robin Hashimoto, Jong-Beom Park, S Tim Yoon, and Jeffrey C Wang. Synthetic bone graft versus autograft or allograft for spinal fusion: a systematic review. *Journal of Neurosurgery: Spine*, 25(4):509–516, 2016.

[144] Oldřich Neděla, Petr Slepička, and Václav Švorčík. Surface modification of polymer substrates for biomedical applications. *Materials*, 10(10):1115, 2017.

[145] Satoshi Sugimoto, Yasushi Matsuda, and Hideo Mori. Carbon nanotube formation directly on the surface of stainless steel materials by plasma-assisted chemical vapor deposition. *J. Plasma Fusion Res. Ser*, 8:522, 2009.

[146] Harland G Tompkins and William A McGahan. Spectroscopic ellipsometry and reflectometry: a user's guide. *(No Title)*, 1999.

[147] Julie Hubert, Claude Poleunis, Arnaud Delcorte, Priya Laha, Jules Bossert, Sten Lambeets, Alper Ozkan, Patrick Bertrand, Herman Terryn, and François Reniers. Plasma polymerization of c4cl6 and c2h2cl4 at atmospheric pressure. *Polymer*, 54(16):4085–4092, 2013.

[148] C Maniatopoulos, J Sodek, and AH Melcher. Bone formation in vitro by stromal cells obtained from bone marrow of young adult rats. *Cell and tissue research*, 254:317–330, 1988.

[149] Catherine D Reyes and Andrés J García. A centrifugation cell adhesion assay for high-throughput screening of biomaterial surfaces. *Journal of Biomedical Materials Research Part A: An Official Journal of The Society for Biomaterials, The Japanese Society for Biomaterials, and The Australian Society for Biomaterials and the Korean Society for Biomaterials*, 67(1):328–333, 2003.

[150] Caroline A Schneider, Wayne S Rasband, and Kevin W Eliceiri. Nih image to imagej: 25 years of image analysis. *Nature methods*, 9(7):671–675, 2012.

[151] Anne E Carpenter, Thouis R Jones, Michael R Lamprecht, Colin Clarke, In Han Kang, Ola Friman, David A Guertin, Joo Han Chang, Robert A

Lindquist, Jason Moffat, et al. Cellprofiler: image analysis software for identifying and quantifying cell phenotypes. *Genome biology*, 7:1–11, 2006.

[152] Melanie L Hart, Jasmin C Lauer, Mischa Selig, Martha Hanak, Brandan Walters, and Bernd Rolauffs. Shaping the cell and the future: recent advancements in biophysical aspects relevant to regenerative medicine. *Journal of Functional Morphology and Kinesiology*, 3(1):2, 2017.

[153] National Research Council et al. *Guide for the care and use of laboratory animals*. National Academies Press, 2010.

[154] Miroslav Michlíček, Satoshi Hamaguchi, and Lenka Zajíčková. Molecular dynamics simulation of amine groups formation during plasma processing of polystyrene surfaces. *Plasma Sources Science and Technology*, 29(10):105020, 2020.

[155] Anton Manakhov, Miroslav Michlíček, Alexandre Felten, Jean-Jacques Pireaux, David Nečas, and Lenka Zajíčková. Xps depth profiling of derivatized amine and anhydride plasma polymers: Evidence of limitations of the derivatization approach. *Applied Surface Science*, 394:578–585, 2017.

[156] Sarah Almubarak, Hubert Nethercott, Marie Freeberg, Caroline Beaudon, Amit Jha, Wesley Jackson, Ralph Marcucio, Theodore Miclau, Kevin Healy, and Chelsea Bahney. Tissue engineering strategies for promoting vascularized bone regeneration. *Bone*, 83:197–209, 2016.

[157] Henry J Mankin, Mark C Gebhardt, L Candace Jennings, Dempsey S Springfield, and William W Tomford. Long-term results of allograft replacement in

the management of bone tumors. *Clinical Orthopaedics and Related Research (1976-2007)*, 324:86–97, 1996.

[158] Shosuke Akita, Noriyuki Tamai, Akira Myoui, Masataka Nishikawa, Takashi Kaito, Kunio Takaoka, and Hideki Yoshikawa. Capillary vessel network integration by inserting a vascular pedicle enhances bone formation in tissue-engineered bone using interconnected porous hydroxyapatite ceramics. *Tissue Engineering*, 10(5-6):789–795, 2004.

[159] Yuan Deng, Chuan Jiang, Cuidi Li, Tao Li, Mingzheng Peng, Jinwu Wang, and Kerong Dai. 3d printed scaffolds of calcium silicate-doped β-tcp synergize with co-cultured endothelial and stromal cells to promote vascularization and bone formation. *Scientific reports*, 7(1):5588, 2017.

[160] Masataka Nishikawa, Akira Myoui, Hajime Ohgushi, Masako Ikeuchi, Noriyuki Tamai, and Hideki Yoshikawa. Bone tissue engineering using novel interconnected porous hydroxyapatite ceramics combined with marrow mesenchymal cells: quantitative and three-dimensional image analysis. *Cell Transplantation*, 13(4):367–376, 2004.

[161] Dan Zhang, Peng Gao, Qin Li, Jinda Li, Xiaojuan Li, Xiaoning Liu, Yunqing Kang, and Liling Ren. Engineering biomimetic periosteum with β-tcp scaffolds to promote bone formation in calvarial defects of rats. *Stem cell research & therapy*, 8(1):1–11, 2017.

[162] Benjamin G Keselowsky, David M Collard, and Andrés J García. Integrin binding specificity regulates biomaterial surface chemistry effects on cell dif-

ferentiation. *Proceedings of the National Academy of Sciences*, 102(17):5953–5957, 2005.

[163] Mark H Lee, Paul Ducheyne, Laura Lynch, David Boettiger, and Russell J Composto. Effect of biomaterial surface properties on fibronectin–$\alpha 5\beta 1$ integrin interaction and cellular attachment. *Biomaterials*, 27(9):1907–1916, 2006.

[164] Amr M Moursi, Ruth K Globus, and Caroline H Damsky. Interactions between integrin receptors and fibronectin are required for calvarial osteoblast differentiation in vitro. *Journal of cell science*, 110(18):2187–2196, 1997.

[165] Benjamin G Keselowsky, David M Collard, and Andrés J García. Surface chemistry modulates fibronectin conformation and directs integrin binding and specificity to control cell adhesion. *Journal of Biomedical Materials Research Part A: An Official Journal of The Society for Biomaterials, The Japanese Society for Biomaterials, and The Australian Society for Biomaterials and the Korean Society for Biomaterials*, 66(2):247–259, 2003.

[166] Benjamin G Keselowsky, David M Collard, and Andrés J García. Surface chemistry modulates focal adhesion composition and signaling through changes in integrin binding. *Biomaterials*, 25(28):5947–5954, 2004.

[167] Kristin E Michael, Varadraj N Vernekar, Benjamin G Keselowsky, J Carson Meredith, Robert A Latour, and Andrés J García. Adsorption-induced conformational changes in fibronectin due to interactions with well-defined surface chemistries. *Langmuir*, 19(19):8033–8040, 2003.

[168] Lori Kornberg, H Shelton Earp, J Thomas Parsons, Michael Schaller, and RL Juliano. Cell adhesion or integrin clustering increases phosphorylation of a focal adhesion-associated tyrosine kinase. *Journal of Biological Chemistry*, 267(33):23439–23442, 1992.

[169] MJP Biggs and MJ Dalby. Focal adhesions in osteoneogenesis. *Proceedings of the Institution of Mechanical Engineers, Part H: Journal of Engineering in Medicine*, 224(12):1441–1453, 2010.

[170] Manus JP Biggs, R Geoff Richards, Nikolaj Gadegaard, Chris DW Wilkinson, Richard OC Oreffo, and Matthew J Dalby. The use of nanoscale topography to modulate the dynamics of adhesion formation in primary osteoblasts and erk/mapk signalling in stro-1+ enriched skeletal stem cells. *Biomaterials*, 30(28):5094–5103, 2009.

[171] Chunxi Ge, Guozhi Xiao, DI Jiang, and Renny T Franceschi. Critical role of the extracellular signal–regulated kinase–mapk pathway in osteoblast differentiation and skeletal development. *The Journal of cell biology*, 176(5):709–718, 2007.

[172] Douglas W Hamilton and Donald M Brunette. The effect of substratum topography on osteoblast adhesion mediated signal transduction and phosphorylation. *Biomaterials*, 28(10):1806–1819, 2007.

[173] Takahiro Kanno, Tetsu Takahashi, Toshiyuki Tsujisawa, Wataru Ariyoshi, and Tatsuji Nishihara. Mechanical stress-mediated runx2 activation is de-

pendent on ras/erk1/2 mapk signaling in osteoblasts. *Journal of cellular biochemistry*, 101(5):1266–1277, 2007.

[174] Robert F Klees, Roman M Salasznyk, Karl Kingsley, William A Williams, Adele Boskey, and George E Plopper. Laminin-5 induces osteogenic gene expression in human mesenchymal stem cells through an erk-dependent pathway. *Molecular biology of the cell*, 16(2):881–890, 2005.

[175] Jun Liu, Zhihe Zhao, Juan Li, Ling Zou, Charles Shuler, Yuanwen Zou, Xuejin Huang, Mingli Li, and Jun Wang. Hydrostatic pressures promote initial osteodifferentiation with erk1/2 not p38 mapk signaling involved. *Journal of cellular biochemistry*, 107(2):224–232, 2009.

[176] Antonella Rocca, Attilio Marino, Veronica Rocca, Stefania Moscato, Giuseppe de Vito, Vincenzo Piazza, Barbara Mazzolai, Virgilio Mattoli, Thu Jennifer Ngo-Anh, and Gianni Ciofani. Barium titanate nanoparticles and hypergravity stimulation improve differentiation of mesenchymal stem cells into osteoblasts. *International Journal of Nanomedicine*, 10:433, 2015.

[177] Rowena McBeath, Dana M Pirone, Celeste M Nelson, Kiran Bhadriraju, and Christopher S Chen. Cell shape, cytoskeletal tension, and rhoa regulate stem cell lineage commitment. *Developmental cell*, 6(4):483–495, 2004.

[178] Kiran Bhadriraju, Michael Yang, Sami Alom Ruiz, Dana Pirone, John Tan, and Christopher S Chen. Activation of rock by rhoa is regulated by cell adhesion, shape, and cytoskeletal tension. *Experimental cell research*, 313(16):3616–3623, 2007.

[179] Yuhui Shen, Waiching Liu, Chunyi Wen, Haobo Pan, Ting Wang, Brian W Darvell, William W Lu, and Wenhai Huang. Bone regeneration: importance of local ph—strontium-doped borosilicate scaffold. *Journal of Materials Chemistry*, 22(17):8662–8670, 2012.

[180] Yuhui Shen, Waiching Liu, Kaili Lin, Haobo Pan, Brian W Darvell, Songlin Peng, Chunyi Wen, Lianfu Deng, William W Lu, and Jiang Chang. Interfacial ph: a critical factor for osteoporotic bone regeneration. *Langmuir*, 27(6):2701–2708, 2011.

[181] Judith M Curran, Rui Chen, and John A Hunt. The guidance of human mesenchymal stem cell differentiation in vitro by controlled modifications to the cell substrate. *Biomaterials*, 27(27):4783–4793, 2006.

[182] Vijay M Ravindra, Steven S Senglaub, Abbas Rattani, Michael C Dewan, Roger Härtl, Erica Bisson, Kee B Park, and Mark G Shrime. Degenerative lumbar spine disease: estimating global incidence and worldwide volume. *Global spine journal*, 8(8):784–794, 2018.

[183] Alexander Jahn, Johan Hviid Andersen, David Høyrup Christiansen, Andreas Seidler, and Annett Dalbøge. Association between occupational exposures and chronic low back pain: Protocol for a systematic review and meta-analysis. *Plos one*, 18(5):e0285327, 2023.

[184] Arnold YL Wong, Jaro Karppinen, and Dino Samartzis. Low back pain in older adults: risk factors, management options and future directions. *Scoliosis and spinal disorders*, 12(1):1–23, 2017.

[185] Steven M Kurtz and John N Devine. Peek biomaterials in trauma, orthopedic, and spinal implants. *Biomaterials*, 28(32):4845–4869, 2007.

[186] Frédéric Cuisinier, Ivan Vladislavov Panayotov, Valérie Orti, and Jacques Yachouh. Polyetheretherketone (peek) for medical applications. *Journal of Materials Science: Materials in Medicine*, 27(7), 2016.

[187] Masafumi Kashii, Kazuma Kitaguchi, Takahiro Makino, and Takashi Kaito. Comparison in the same intervertebral space between titanium-coated and uncoated peek cages in lumbar interbody fusion surgery. *Journal of Orthopaedic Science*, 25(4):565–570, 2020.

[188] Weiling Yin, Miao Chen, Jiaxiang Bai, Yaozeng Xu, Miao Wang, Dechun Geng, and Guoqing Pan. Recent advances in orthopedic polyetheretherketone biomaterials: Material fabrication and biofunction establishment. *Smart Materials in Medicine*, 3:20–36, 2022.

[189] John W Brantigan, Arvo Neidre, and John S Toohey. The lumbar i/f cage for posterior lumbar interbody fusion with the variable screw placement system: 10-year results of a food and drug administration clinical trial. *The spine journal*, 4(6):681–688, 2004.

[190] Tongtong Ma, Jiajia Zhang, Shuoyao Sun, Wenqing Meng, Yan Zhang, and Junling Wu. Current treatment methods to improve the bioactivity and bonding strength of peek for dental application: A systematic review. *European Polymer Journal*, page 111757, 2022.

[191] Xinming Gu, Xiaolin Sun, Yue Sun, Jia Wang, Yiping Liu, Kaixuan Yu, Yao Wang, and Yanmin Zhou. Bioinspired modifications of peek implants for bone tissue engineering. *Frontiers in bioengineering and biotechnology*, 8:631616, 2021.

[192] Tianjie Chen, Yohei Jinno, Ikiru Atsuta, Akira Tsuchiya, Michele Stocchero, Eriberto Bressan, and Yasunori Ayukawa. Current surface modification strategies to improve the binding efficiency of emerging biomaterial polyetheretherketone (peek) with bone and soft tissue: A literature review. *Journal of Prosthodontic Research*, page JPR_D_22_00138, 2022.

[193] Yihan Wang, Shutao Zhang, Bin'en Nie, Xinhua Qu, and Bing Yue. Approaches to biofunctionalize polyetheretherketone for antibacterial: A review. *Frontiers in Bioengineering and Biotechnology*, 10:895288, 2022.

[194] Les E Lanyon and Walter R Heald. Magnesium, calcium, strontium, and barium. *Methods of Soil Analysis: Part 2 Chemical and Microbiological Properties*, 9:247–262, 1983.

[195] S Pors Nielsen. The biological role of strontium. *Bone*, 35(3):583–588, 2004.

[196] Pierre J Marie and Monique Hott. Short-term effects of fluoride and strontium on bone formation and resorption in the mouse. *Metabolism*, 35(6):547–551, 1986.

[197] MD Grynpas and PJ Marie. Effects of low doses of strontium on bone quality and quantity in rats. *Bone*, 11(5):313–319, 1990.

[198] Pierre J Marie. Strontium as therapy for osteoporosis. *Current opinion in pharmacology*, 5(6):633–636, 2005.

[199] Tomio Morohashi, Tsuneyoshi Sano, and Shoji Yamada. Effects of strontium on calcium metabolism in rats i. a distinction between the pharmacological and toxic doses. *The Japanese Journal of Pharmacology*, 64(3):155–162, 1994.

[200] Tomio Morohashi, Tsuneyoshi Sano, Kazuo Harai, and Shoji Yamada. Effects of strontium on calcium metabolism in rats ii. strontium prevents the increased rate of bone turnover in ovariectomized rats. *The Japanese Journal of Pharmacology*, 68(2):153–159, 1995.

[201] Li Li, Litao Yao, Haiyan Wang, Xufei Shen, Weiwei Lou, Chengyi Huang, and Gang Wu. Magnetron sputtering of strontium nanolayer on zirconia implant to enhance osteogenesis. *Materials Science and Engineering: C*, 127:112191, 2021.

[202] Ole Z Andersen, Vincent Offermanns, Michael Sillassen, Klaus P Almtoft, Inge H Andersen, Søren Sørensen, Christian S Jeppesen, David CE Kraft, Jørgen Bøttiger, Michael Rasse, et al. Accelerated bone ingrowth by local delivery of strontium from surface functionalized titanium implants. *Biomaterials*, 34(24):5883–5890, 2013.

[203] Yongfeng Li, Yaping Qi, Qi Gao, Qiang Niu, Mingming Shen, Qian Fu, Kaijin Hu, and Liang Kong. Effects of a micro/nano rough strontium-loaded

surface on osseointegration. *International journal of nanomedicine*, pages 4549–4563, 2015.

[204] Yaichiro Okuzu, Shunsuke Fujibayashi, Seiji Yamaguchi, Koji Yamamoto, Takayoshi Shimizu, Takashi Sono, Koji Goto, Bungo Otsuki, Tomiharu Matsushita, Tadashi Kokubo, et al. Strontium and magnesium ions released from bioactive titanium metal promote early bone bonding in a rabbit implant model. *Acta Biomaterialia*, 63:383–392, 2017.

[205] Yunchang Xin, Jiang Jiang, Kaifu Huo, Tao Hu, and Paul K Chu. Bioactive srtio3 nanotube arrays: strontium delivery platform on ti-based osteoporotic bone implants. *ACS nano*, 3(10):3228–3234, 2009.

[206] Jin-Woo Park, He-Kyung Kim, Youn-Jeong Kim, Je-Hee Jang, Hwangjun Song, and Takao Hanawa. Osteoblast response and osseointegration of a ti–6al–4v alloy implant incorporating strontium. *Acta biomaterialia*, 6(7):2843–2851, 2010.

[207] Haiyan Wang, Qiuping Xu, Hui Hu, Chunling Shi, Ziyan Lin, Huixi Jiang, Huaipu Dong, and Jing Guo. The fabrication and function of strontium-modified hierarchical micro/nano titanium implant. *International Journal of Nanomedicine*, pages 8983–8998, 2020.

[208] Ane Escobar, Nicolás Muzzio, Paula C Angelome, Andrea V Bordoni, Angel Martínez, Elisa Bindini, Emerson Coy, Patrizia Andreozzi, Marek Grzelczak, and Sergio E Moya. Strontium titanate (srtio3) mesoporous coatings for en-

hanced strontium delivery and osseointegration on bone implants. *Advanced Engineering Materials*, 21(7):1801210, 2019.

[209] KL Wong, CT Wong, WC Liu, HB Pan, MK Fong, WM Lam, WL Cheung, WM Tang, KY Chiu, KDK Luk, et al. Mechanical properties and in vitro response of strontium-containing hydroxyapatite/polyetheretherketone composites. *Biomaterials*, 30(23-24):3810–3817, 2009.

[210] Michele Bianchi, Lorenzo Degli Esposti, Alberto Ballardini, Fabiola Liscio, Matteo Berni, Alessandro Gambardella, Sander CG Leeuwenburgh, Simone Sprio, Anna Tampieri, and Michele Iafisco. Strontium doped calcium phosphate coatings on poly (etheretherketone)(peek) by pulsed electron deposition. *Surface and Coatings Technology*, 319:191–199, 2017.

[211] Shengnan Wang, Yuanyi Yang, Yunfei Li, Jiacheng Shi, Jianshu Zhou, Li Zhang, Yi Deng, and Weizhong Yang. Strontium/adiponectin co-decoration modulates the osteogenic activity of nano-morphologic polyetheretherketone implant. *Colloids and Surfaces B: Biointerfaces*, 176:38–46, 2019.

[212] Xinjin Su, Zhuocheng Lyu, Yuezhou Wu, Yue-Huan Gu, Shicheng Huo, and Chun Zhou. Strontium-doped bioactive glass/pda functionalized polyetheretherketone with immunomodulatory property for enhancing photothermal clearance of staphylococcus aureus. *Materials & Design*, 225:111552, 2023.

[213] John A. Thornton. Influence of apparatus geometry and deposition condi-

tions on the structure and topography of thick sputtered coatings. *J. Vac. Sci. Technol.*, 11(4):666–670, 07 1974.

[214] John A. Thornton. The microstructure of sputter-deposited coatings. *J. Vac. Sci. Technol. A*, 4(6):3059–3065, 11 1986.

[215] S. M. Rossnagel, D. Mikalsen, H. Kinoshita, and J. J. Cuomo. Collimated magnetron sputter deposition. *J. Vac. Sci. Technol. A*, 9(2):261–265, 03 1991.

[216] S. Hamaguchi and S. M. Rossnagel. Simulations of trench-filling profiles under ionized magnetron sputter metal deposition. *J. Vac. Sci. Technol. B*, 13(2):183–191, 03 1995.

[217] A. A. Mayo, S. Hamaguchi, J. H. Joo, and S. M. Rossnagel. Across-wafer nonuniformity of long throw sputter deposition. *J. Vac. Sci. Technol.B*, 15(5):1788–1793, 09 1997.

[218] Kiyotaka Wasa, Isaku Kanno, and Hidetoshi Kotera. *Handbook of Sputter Deposition Technology, 2nd ed.* William Andrew, Norwich, NY, 2012.

[219] J. E. Greene. Review Article: Tracing the recorded history of thin-film sputter deposition: From the 1800s to 2017. *J. Vac. Sci. Technol. A*, 35(5):05C204, 09 2017.

[220] Yukio Fukuda, Katsuhiro Aoki, Ken Numata Ken Numata, and Akitoshi Nishimura Akitoshi Nishimura. Current-voltage characteristics of electron-cyclotron-resonance sputter-deposited srtio3 thin films. *Jpn. J. Appl. Phys.*, 33(9S):5255, sep 1994.

[221] Chih-Yi Liu and Tseung-Yuen Tseng. Electrical properties of sputter deposited srtio3 gate dielectrics. *Journal of the European Ceramic Society*, 24(6):1449–1453, 2004. Electroceramics VIII.

[222] `https://imagej.net/ij/`. Accessed: 2023-09-15.

[223] Cheol-Min Han, Eun-Jung Lee, Hyoun-Ee Kim, Young-Hag Koh, Keung N Kim, Yoon Ha, and Sung-Uk Kuh. The electron beam deposition of titanium on polyetheretherketone (peek) and the resulting enhanced biological properties. *Biomaterials*, 31(13):3465–3470, 2010.

[224] Hsi-Kai Tsou, Ping-Yen Hsieh, Meng-Hui Chi, Chi-Jen Chung, and Ju-Liang He. Improved osteoblast compatibility of medical-grade polyetheretherketone using arc ionplated rutile/anatase titanium dioxide films for spinal implants. *Journal of Biomedical Materials Research Part A*, 100(10):2787–2792, 2012.

[225] Akira Miyagaki, Yusuke Kamaya, Takuya Matsumoto, Koji Honda, Masafumi Shibahara, Chizuru Hongo, and Takashi Nishino. Surface modification of poly (ether ether ketone) through friedel–crafts reaction for high adhesion strength. *Langmuir*, 35(30):9761–9768, 2019.

[226] Poonam Sundriyal, Megha Sahu, Om Prakash, and Shantanu Bhattacharya. Long-term surface modification of peek polymer using plasma and peg silane treatment. *Surfaces and Interfaces*, 25:101253, 2021.

[227] Jay R Dondani, Janaki Iyer, and Simon D Tran. Surface treatments of peek for osseointegration to bone. *Biomolecules*, 13(3):464, 2023.

[228] Masashi Yamashiro, Hideaki Yamada, and Satoshi Hamaguchi. Molecular dynamics simulations for nitridation of organic polymer surfaces due to hydrogen–nitrogen ion beam injections. *Thin solid films*, 516(11):3449–3453, 2008.

[229] Linus Pauling. *The Nature of the Chemical Bond and the Structure of Molecules and Crystals: An Introduction to Modern Structural Chemistry*, volume 18. Cornell University Press, 1960.

[230] Steven S Zumdahl and Donald J DeCoste. *Introductory chemistry: A foundation*. Cengage learning, 2010.

[231] R Bruce King. *Encyclopedia of inorganic chemistry*, volume 10. Wiley Online Library, 2005.

Research Achievement

Publications

1. Anjar Anggraini Harumningtyas, Tomoko Ito, Hidekazu Kita, Joe Kodama, Takashi Kaito, Satoshi Hamaguchi, "Amine Plasma Polymers Deposited on Porous Hydroxyapatite Artificial Bone with Bipolar Pulsed Discharges," J. Vac. Sci. Technol. A, vol. 42, issue 5, 2024.

2. Anjar Anggraini Harumningtyas, Nicolas Mauchamp, Michiro Isobe, Jomar U. Tercero, Satoshi Hamaguchi, "The Effect of Oxygen Radicals in Amine Plasma Polymers using MD simulations," 2024. (To be submitted)

3. Anjar Anggraini Harumningtyas, Tomoko Ito, Masato Ikuta, Takashi Kaito, Satoshi Hamaguchi, "Polyetheretherketone (PEEK) implant functionalization with magnetron-sputtered $SrTiO_3$ for regenerative medicine," Plasma Medicine, vol. 13, issue 3, pp. 53-67, 2023.

4. Anjar Anggraini Harumningtyas, Tomoko Ito, Michiro Isobe, Lenka Zajíčková, Satoshi Hamaguchi, "Molecular dynamics simulation of amine formation in plasma-enhanced chemical vapor deposition (PECVD) with hy-

drocarbon and amino radicals," J. Vac. Sci. Technol. A, vol. 41, issue 6, 2023.

5. J. Kodama*, A. A. Harumningtyas*, T. Ito, M. Michlíček, S. Sugimoto, H. Kita, R. Chijimatsu, Y. Ukon, J. Kushioka, R. Okada, T. Kamatani, K. Hashimoto, D. Tateiwa, H. Tsukazaki, S. Nakagawa, S. Takenaka, T. Makino, Y. Sakai, D. Nečas, L. Zajičková, S. Hamaguchi, T. Kaito, "Amine modification of calcium phosphate by low-pressure plasma for bone regeneration," Scientific Reports, vol. 11, no. 1, pp. 1–15, 2021. (* equal contribution)

6. Z. Donkó, L. Zajičková, S. Sugimoto, A. A. Harumningtyas, and S. Hamaguchi, "Modeling characterisation of a bipolar pulsed discharge," Plasma Sources Science and Technology, vol. 29, no. 10, p. 104001, 2020.

International and Domestic Conferences

1. "Development of Highly Functional Biomedical Materials by Low-Pressure Plasma-based Surface Modification," Anjar Anggraini Harumningtyas, Tomoko Ito, Michiro Isobe, Satoshi Sugimoto, Joe Kodama, Takashi Kaito, Lenka Zajíčková, Satoshi Hamaguchi, the 15th HOPE Meeting with Nobel Laureates, Japan Society for the Promotion of Science (JSPS), Kyoto, Japan, 26 February - 1 March 2024. [flash talk and poster presentation]

2. "Low-temperature atomic layer deposition (ALD) of strontium oxide on poly(ether-ether-ketone) (PEEK) for lumbar cage implants," A. A. Harumn-

ingtyas, L. Zajíčková, M. Eliáš, T. Ito, D. Nečas, L. Janů, E. Dvořáková, M. Ikuta, T. Kaito, P. Vinchon and S. Hamaguchi, the 25th International Symposium on Plasma Chemistry (ISPC25), (May 21th-26th, 2023, Kyoto, Japan). [oral presentation]

3. "Thermal and Plasma-enhanced Atomic Layer Deposition of Strontium Oxide on Artificial Cages," Anjar Anggraini Harumningtyas, Lenka Zajíčková, Marek Eliáš, Tomoko Ito, David Nečas, Lucie Janů, Eva Dvořáková, Pierre Vinchon, Masato Ikuta, Takashi Kaito, Satoshi Hamaguchi, 4th International Conference on Data-Driven Plasma Science (ICDDPS-4) and the 14th EU-Japan Joint Symposium on Plasma Processing (JSPP-14), (April 16th-21th, 2023, Okinawa, Japan). [poster presentation]

4. "Amine-modified on artificial bone by PECVD and molecular dynamic simulation of N-H bond interaction," Anjar Anggraini Harumningtyas, Tomoko Ito, Michiro Isobe, Satoshi Sugimoto, Joe Kodama, Takashi Kaito, Lenka Zajíčková, Satoshi Hamaguchi, The 25th International school on low plasma physics: basics and applications, (October 1st-8th, 2022, Physikzentrum Bad Honnef, Germany) [poster presentation]

5. "Atomic Layer Deposition of Strontium Oxide on Poly(ether-ether-ketone)," Harumningtyas Anjar Anggraini, Zajíčková Lenka, Eliáš Marek, Ito Tomoko, Nečas David, Blahová Lucie, Dvořáková Eva, Hamaguchi Satoshi, The XIV international conference NANOCON'22, (October 19th-21th, 2022, Brno, Czech Republic)

6. "Polyether-ether ketone (PEEK) functionalization by $SrTiO_3$ for lumbar in-

terbody fusion cage," Anjar Anggraini Harumningtyas, Masato Ikuta, Tomoko Ito, Takashi Kaito, Satoshi Hamaguchi, 9th International Conference on Plasma Medicine (ICPM9), (June 27th to July 1st, 2022, Utrecht, Netherland). [oral presentation]

7. "Development of a DC-Plasma Source for Surface Functionalization by Amino Groups," Anjar Anggraini Harumningtyas, Suprapto, Hari Suprihatin, Ihwanul Aziz, Wiwien Andriyanti, Tjipto Sujitno, Agus Purwadi, Satoshi Hamaguchi, (2021), AIP Conference Proceedings. Vol. 2381, No. 1, p. 020018, AIP publishing LLC. [oral presentation]

8. "Stability of Primary Amine Groups During Plasma Polymerization for the Surface Modification of Artificial Bones", Anjar Anggraini Harumningtyas, Tomoko Ito, Satoshi Sugimoto, Michiro Isobe, Joe Kodama, Takashi Kaito, Lenka Zajíčková, Satoshi Hamaguchi, 74th Annual Gaseous Electronic Conference, Bulletin of the American Physical Society, Vol. 66, Number 7, 4-8 October 2021, online. [oral presentation]

9. "Effect of Primary Amines Formed by Low-Pressure Pulsed Plasma on Bone Regeneration and Numerical Study of Amine Formation using MD Simulation", Anjar Anggraini Harumningtyas, Tomoko Ito, Satoshi Sugimoto, Michiro Isobe, Joe Kodama, Takashi Kaito, Lenka Zajíčková, Satoshi Hamaguchi, Bridging the Pandemic: Reigniting Cooperation on Plasma Research (Deutschland-Japan), 25 November 2021, online. [poster presentation]

10. Anjar Anggraini Harumningtyas, Tomoko Ito, Satoshi Sugimoto, Joe Kodama, Takashi Kaito, Chieko Asamori, Miroslav Michlicek, David Necas,

Lenka Zajickova, Satoshi Hamaguchi, "The Amino Group Effect of Plasma Irradiation for Surface Treatment on Hydroxyapatite (HA) Artificial Bone", The 66th JSAP Spring Meeting, Tokyo, March 2019. [oral presentation]

11. Anjar Anggraini Harumningtyas, Tomoko Ito, Satoshi Sugimoto, Joe Kodama, Takashi Kaito, Chieko Asamori, Miroslav Michlicek, David Necas, Lenka Zajickova, Satoshi Hamaguchi, "Amine Rich Plasma Polymerization using Inverter for Orthopaedic Application", 24th International Symposium on Plasma Chemistry, Italy, June 2019. [poster presentation]

12. Anjar Anggraini Harumningtyas, Michiro Isobe, Tomoko Ito, Satoshi Sugimoto, Satoshi Hamaguchi, "Analysis of Amino Group Bonds in Plasma Polymerization using Molecular Dynamics Simulation", XXXIV International Conference on Phenomena in Ionized Gases (XXXIV ICPIG) and 10th International Conference on Reactive Plasmas (ICRP-10), Hokkaido, Japan, July 2019. [poster presentation]

13. Tomoko Ito, Anjar Anggraini Harumningtyas, Satoshi Sugimoto, Satoshi Hamaguchi, 2018, Plasma Surface Functionalization of Biocompatible Materials, 2nd International Workshop on Plasma Agriculture (IWOPA2) Takayama, Gifu, Japan. [poster presentation]

14. Anjar Anggraini H., et.al, 2017, Construction and Function Test of Rogowski Coil for Plasma Spot and Plasma Discharge Currents Measurement in Plasma Cathode Electron Source (PCES), International Symposium "The 10th EU-Japan Joint Symposium on Plasma (JSPP2017) and The 82nd

IUVSTA Workshop on Plasma-based Atomic Layer Processes", Okinawa, Japan. [poster presentation]

International School or Research Meeting

1. International Join Research at CEITEC Nano research infrastructure, May 13th to July 31st, 2022, Brno, Czech Republic.

2. The Summer School on Plasma Medicine, the 9th International Conference on Plasma Medicine (ICPM9), June 25th and June 26th, 2022, Utrecht, The Netherlands.

3. Plasma Class "Low-Temperature Plasma Physics: Basics and Applications" of the 25th International Plasma School, October 1-6, 2022, Physikzentrum, Bad Honnef (Germany).

4. Master Class "Plasma Propulsion" of the 25th International Plasma School, Bad Honnef (Germany), October 6-8, 2022, Physikzentrum, Bad Honnef (Germany).

5. Visiting Student at Institute for Experimental Physics - Plasma and Atomic Physics, Ruhr- University Bochum, October 9-15, 2022, Germany, October, Bochum, Germany.

6. International Join Research at Central European Institute of Technology (CEITEC) and Masaryk University, Brno, Czech Republic, November-December 2018.

Awards

1. Recipient of JSPS HOPE fellow of the 15th HOPE Meeting with Nobel Laureates, Japan Society for the Promotion of Science (JSPS), Kyoto, Japan, 26 February - 1 March 2024.

2. Recipient of (MEXT) Scholarship for Doctoral Degree from Japanese Government Ministry of Education, Culture, Sports, Science and Technology, Japan, (October 2020- September 2023).

3. Recipient of GEC Travel Grant of The 74th Annual Gaseous Electronics Conference, Huntsville, US, October 4 - 8, 2021.

4. Recipient of Riset-Pro Scholarship for Master Degree from Ministry of Research, Technology and Higher Education of the Republic of Indonesia, (October 2017- September 2019).

5. Recipient of the Best Scientific Poster Award (3rd Winner), 3rd CEITEC Nano User Meeting, Brno, Czech Republic, November 2018.

6. Recipient of IPCS Scholarship for 24th International Symposium on Plasma Chemistry, Italy, June 2019.

7. Recipient of the Best Scientific Poster Award (1st Winner), Riset-Pro Program Symposium, Ministry of Research, Technology and Higher Education of the Republic of Indonesia, Jakarta, Indonesia, 3-4 December 2019.